Ultrafast electron diffraction and imaging using ionized electrons

Dissertation zur Erlangung des Grades
eines Doktors der Naturwissenschaften
am Fachbereich Physik
der Freien Universität Berlin

Faruk Krečinić

Berlin, September 2016

This work has been performed between September 2011 and June 2016 at the Max Born Institute for Nonlinear Optics and Short Pulse Spectroscopy, Berlin, under the supervision of Prof. Dr. Marc Vrakking.

Berlin, September 2016

1. Gutachter: Prof. Dr. Marc Vrakking
2. Gutachter: Prof. Dr. Jochen Küpper

Tag der Disputation: 06.06.2017

Abstract

This thesis investigates two different techniques that can potentially be used for the direct imaging of ultrafast structural dynamics of molecules at the femtosecond time scale and with Ångström spatial resolution. Conventional ultrafast diffraction and imaging techniques use *elastically* scattered energetic particles, i.e. X-rays or electrons, to probe the molecular structure. The two techniques studied in this thesis make use of *inelastic* processes to produce *ionized* (secondary) electrons, that are subsequently used to image the molecular structure.

The first technique studied in this thesis is Laser Induced Electron Diffraction (LIED). The ionization of a molecule in a strong, low-frequency laser field leads to the creation of a photoelectron wavepacket that is driven by the laser and can re-collide with its parent molecule. These re-scattered photoelectrons display diffraction features, i.e. LIED, that can be used for the reconstruction of the molecular structure [1, 2, 3].

A series of experiments was performed, investigating the effect of the *molecular frame* on the Photoelectron Angular Distribution (PAD) of impulsively aligned and strong-field ionized CF_3I molecules using a Velocity Map Imaging Spectrometer (VMIS). It is shown that using the impulsive laser alignment technique enables taking *differential measurements* that bring out directly and clearly LIED effects in the PAD, even for a relatively *complex molecule* such as CF_3I. The comparison of the experimental results at different laser intensities and at two different probe wavelengths, i.e. 800 and 1300 nm, shows that the LIED effect is robust and reproducible for a wide range of experimental conditions, and at comparatively low re-collision energies. Moreover, the first results from Time-Dependent Density Functional Theory (TDDFT) calculations indicate that the ionization of multiple molecular orbitals, which have a distinct shape and orientation with respect to the molecular frame, leads to significant effects and can be identified in the experimental results.

The second technique investigated in this thesis proposes the use of secondary electrons produced by electron impact ionization for the imaging of the molecular structure during a dynamical process. Specifically, Impact Ionized Coherent Electron Emission (IICEE), which leads to the interference between electrons that are ejected from two identical atomic centres within a molecule [4], was investigated experimentally.

A commercially available *table-top* Ultrafast Electron Diffraction (UED) source was used to produce a beam of (primary) electrons that subsequently ionizes the target atom or molecule and generates energetic secondary electrons. The table-top UED source was combined with a high-energy Velocity Map Imaging Spectrometer (VMIS) and applied to the study of secondary electron emission. By comparing the spectra of Helium and H_2 to theoretical calculations, it is shown that hints of IICEE effects due to the molecular structure of H_2 may be visible in the experimental data. However, possible systematic errors in the experiment and the shortcomings of the theoretical model in reproducing the low-energy part of the spectrum make an unambiguous assignment to IICEE effects difficult. Simulations with perfectly aligned and partially aligned H_2 were used to illustrate the effect of alignment on the secondary electron spectrum. It is shown that using molecular alignment enables clear and unambiguous extraction of molecular effects from secondary electron spectra of impact ionized molecules, in a similar fashion as demonstrated by the LIED experiments.

Kurzfassung

Diese Arbeit untersucht zwei verschiedene Techniken, welche potenziell zur direkten Abbildung von ultraschneller Strukturdynamik von Molekülen auf der Zeitskala von Femtosekunden und mit Ångström räumlicher Auflösung verwendet werden können. Konventionelle ultraschnelle Beugungs- und Abbildungstechniken verwenden *elastisch* gestreute energetische Teilchen um die molekulare Struktur zu untersuchen. Die in dieser Arbeit untersuchten Techniken nutzen *inelastische* Prozesse um ionisierte (sekundäre) Elektronen zu erzeugen, mittels derer anschließend die molekulare Struktur abgebildet wird.

Die erste Technik, die in dieser Arbeit untersucht wird, ist Laser Induced Electron Diffraction (LIED). Die Ionisation eines Moleküls in einem starken, niederfrequenten Laserfeld führt zur Erzeugung eines Photoelektronenwellenpakets, welches durch den Laser beschleuningt wird und mit dem ursprünglichen Molekül wieder kollidieren kann. Diese gestreuten Photoelektronen zeigen Beugungsmerkmale, d.h. LIED-Muster, welche für die Rekonstruktion der molekularen Struktur verwendet werden können. Es wurde eine Reihe von Experimenten durchgeführt, in denen der Einfluss der molekularen Struktur auf die Photoelektronen-Winkelverteilung von impulsiv ausgerichteten CF_3I Molekülen untersucht wurde. Die Technik der impulsiven Laserausrichtung ermöglicht Differenzmessungen, mittels derer direkt und eindeutig LIED-Effekte in der Photoelektronen-Winkelverteilung hervorgehoben werden, auch für ein relativ komplexes Molekül wie CF_3I. Der Vergleich der Versuchsergebnisse bei verschiedenen Laserintensitäten sowie bei zwei verschiedenen Abfrage-Wellenlängen von 800 nm und 1300 nm zeigt, dass der LIED-Effekt für einen weiten Bereich von experimentellen Bedingungen und bei vergleichsweise niedrigen Wiederkollisionsenergien robust und reproduzierbar ist. Darüber hinaus zeigen erste Ergebnisse von Berechnungen zeitabhängiger Dichtefunktionaltheorie, dass die Ionisation von mehreren Molekülorbitalen, die eine unterschiedliche Form und Ausrichtung in Bezug auf das Molekül aufweisen, ebenfalls signifikant ist und in den Versuchsergebnissen identifiziert werden kann.

Die zweite in dieser Arbeit untersuchte Technik basiert auf dem Vorschlag Sekundärelektronen, welche durch Elektronenstoß-Ionisation erzeugt werden, zum Abbilden der Molekülstruktur während eines dynamischen Prozesses zu verwenden. Insbesondere wurden Interferenzeffekte zwischen Elektronen, welche mittels kohärenter Stoßionisation aus zwei unterschiedlichen Atomzentren innerhalb eines Moleküls ausgestoßen werden [4], experimentell untersucht. Eine kommerziell erhältliche ultraschnelle Elektronenquelle wurde verwendet um einen Primärstrahl von Elektronen zu erzeugen, welcher das Atom oder Molekül ionisiert und energetische Sekundärelektronen erzeugt. Durch den Vergleich der Spektren von Helium und H_2 mit theoretischen Berechnungen wird gezeigt, dass Hinweise auf Interferenzeffekte in den experimentellen Daten sichtbar sind, die von der molekularen Struktur von H_2 herrühren. Allerdings erschweren mögliche systematische Fehler im Experiment sowie Mängel des theoretischen Modells im niederenergetischen Teil des Spektrums eine eindeutige Zuordnung dieser Effekte zur molekularen Struktur. Simulationen mit perfekt und teilweise ausgerichteten H_2-Molekülen wurden verwendet, um zu zeigen dass molekulare Effekte in den Sekundärelektronenspektren von ionisierten Molekülen klar und eindeutig mittels molekularer Ausrichtung extrahiert werden können.

Contents

Chapter 1

Introduction

1.1 Scientific objective

The subject of this thesis are two techniques that can potentially be used for the direct imaging of ultrafast structural dynamics of molecules at the femtosecond timescale and with Ångström spatial resolution. The motivation for the development of ultrafast imaging techniques originated from the field of femtochemistry. Femtochemistry tries to elucidate the basic processes underlying the dynamics of chemical bonds and can be said to seek answers to these three main questions [5]

1. How does the reaction energy redistribute within the molecule?
2. What are the detailed nuclear motions characterizing the chemical reaction and its transition states?
3. What are the speeds of the chemical changes connecting the quantum states in the reactants, through the transition states, to products?

Figure 1.1 shows one of the earliest experiments in femtochemistry that made use of optical spectroscopy to successfully demonstrate photo-induced ultrafast dynamics in NaI [6]. However, due to the relative complexity of extracting molecular structure from spectroscopic information it was clear very early on that techniques that could *directly image* the structure of a molecule undergoing ultrafast dynamics would be highly desirable [7, 8].

In order to achieve the goal of ultrafast imaging of molecular reactions with the required spatial *and* temporal resolution, femtosecond sources of electrons or X-rays are required. Very soon after the first successes in ultrafast spectroscopy ultrafast electron sources based on the photoemission from a solid photocathode by irradiation with an ultrafast laser pulse were proposed [9]. This led to the first experiments using Ultrafast Electron Diffraction (UED) to elucidate gas-phase radical structures [10]. The UED technique has reached a certain level of maturity since then and has been used to study a wide variety of systems, ranging from the solid state to the gas-phase, with a time resolution down to 100 fs [11, 12, 13]. With the development of the X-ray Free Electron Lasers, the extremely bright and short X-ray pulses necessary for Ultrafast X-ray Diffraction (UXD) have also become available. The UXD technique is especially promising for the imaging of the structural dynamics of biologically relevant systems

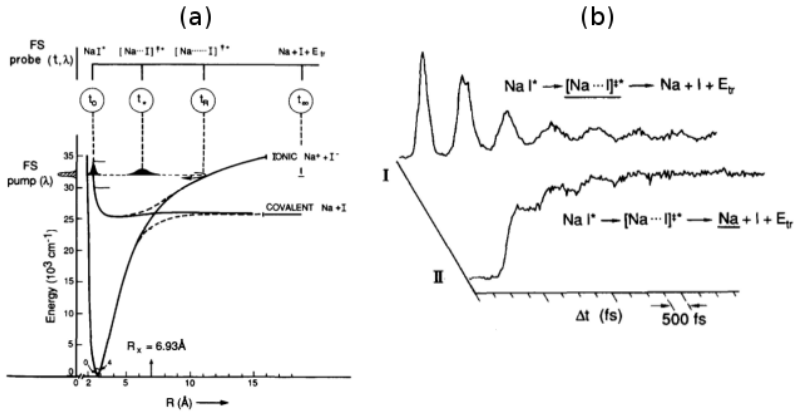

Figure 1.1: Ultrafast laser-induced fluorescence of NaI; image taken from [6]. (a) The NaI molecule is brought into a dissociative (covalent bonding) state by the pump pulse, which initiates the dynamics and leads to a structural motion in the molecule where the excited state is coupled to the ground state (ionic bond) through an avoided crossing. (b) Fluorescence signal from the NaI radical (I), showing the oscillatory motion across the avoided crossing, and Na (II) showing the stepwise increment of the Na atom yield as the molecule dissociates.

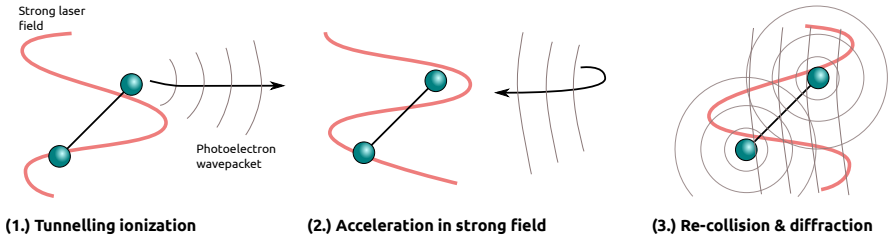

Figure 1.2: Three-step model of Laser Induced Electron Diffraction (LIED). After tunnelling ionization by the strong laser field (1), the photoelectron is accelerated by the oscillating electric field (2) and is finally driven back to the molecule where it scatters elastically (3). The multi-center nature of the molecule, i.e. molecular structure, leads to diffraction features in the final photoelectron spectrum.

[14], and in recent years the ability to image large and complex biomolecules undergoing photoreactions has been experimentally demonstrated [15, 16].

The 'conventional' approach to ultrafast imaging is to use *elastically* scattered X-rays or electrons to form a diffraction image. In recent years several promising techniques for ultrafast diffraction have been proposed that use *ionized* (secondary) electrons to image the molecule with its own electrons [1, 2, 3, 17, 18, 19]. This thesis investigates two such techniques that employ ionized electrons to probe the molecular structure and that can potentially be used for ultrafast molecular structure imaging.

The basic idea behind the first technique, Laser Induced Electron Diffraction

(LIED), is illustrated in Fig. 1.2. The ionization of a molecule in a strong laser field leads to the creation of a photoelectron wavepacket that is driven by the laser to re-collide with its parent molecule [1, 2, 3]. The elastically scattered photoelectrons display diffraction features that can be used for the reconstruction of molecular structure. The ultimate time resolution of this technique is in principle on the order of one half of the laser cycle duration (e.g. 3.3 fs for λ_{laser}=2 μm). The spatial resolution depends on the de Broglie wavelength of the re-colliding electron, which can reach sub-Å scales when long wavelength strong laser fields are used that can achieve re-collision energies of more than a hundred eV.

The second technique investigated in this thesis proposes the use of secondary electrons produced by *electron impact ionization* for the imaging of the molecular structure during a dynamical process. The ultrafast diffraction techniques proposed so far rely on the use of *photoionization* to generate the secondary electrons that are used to image the molecular structure. The recent development of *table-top* Ultrafast Electron Diffraction (UED) sources, which are readily available and can even be obtained commercially [20], has inspired the idea of using these sources to generate energetic secondary electrons that may be used for ultrafast molecular structure imaging. Secondary electrons produced by electron impact ionization may carry information on the molecular structure through different physical mechanisms, as illustrated in Fig. 1.3. Impact Ionized Coherent Electron Emission (IICEE) leads to the interference between electrons emitted from multiple, identical atomic centres within a molecule [4]. A second mechanism that can give rise to molecular interference effects is Impact Ionized Secondary Electron Diffraction (IISED). An impact ionized electron that is ejected from one of the atomic centres within the molecule can scatter elastically from *another* atomic center, which leads to interferences between the scattered

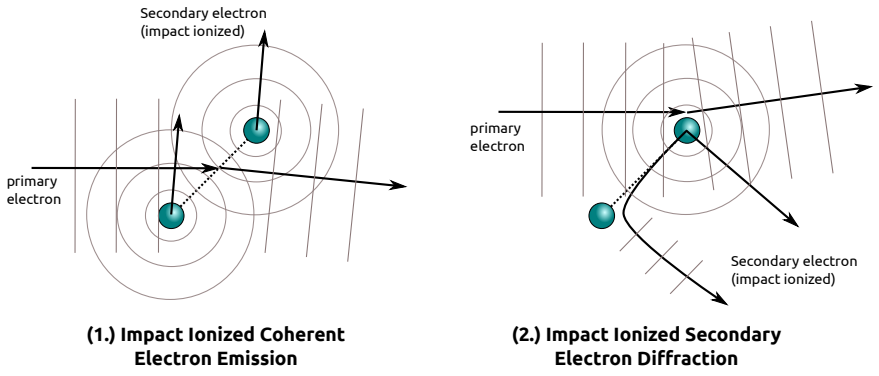

Figure 1.3: Schematic illustration of two processes that may give rise to molecular interference effects in the spectrum of impact ionized electrons. Impact Ionized Coherent Electron Emission (IICEE) leads to interferences between secondary electrons emitted from two distinct atomic centres within the molecule. Impact Ionized Secondary Electron Diffraction (IISED) arises when a secondary electron produced at one atomic centre is scattered by another atomic centre within the same molecule.

and *non*-scattered electrons [4]. IISED can be seen as a generalization of the photoelectron diffraction effect, see e.g. [21]. The IICEE and IISED effects, which carry information on the molecular structure, could in principle be used to image the molecular structure during a *dynamical* process.

Finally, another ingredient in the experiments and the theoretical calculations presented in this thesis is the use of molecular alignment as a means of extracting molecular structure effects from electron spectra. Recent Free Electron Laser (FEL) [22] and UED [23, 24] experiments have demonstrated the potential for using molecular alignment in combination with X-ray and electron diffraction. The experiments presented in Chapter 3 demonstrate that the use of molecular alignment enables taking *differential measurements* that bring out directly and clearly LIED effects in the photoelectron spectra of a strong-field ionized molecule. In Chapter 4 it is shown using theoretical calculations that using the alignment effect should also enable clear and unambiguous extraction of IICEE effects from the secondary electron spectra of electron impact ionized molecules.

1.2 Thesis overview

Chapter 2 summarizes the basic principles of electron scattering theory and highlights approaches and approximations which are specifically needed to understand theoretical considerations and calculations in this thesis. It introduces all the necessary concepts and the basic theoretical models that are used in the rest of the thesis such as differential cross-sections, Born series, partial wave expansions, etc. The final section in this chapter also introduces some basic concepts from strong-field theory, which are needed for the discussion on LIED effects, and shows how the electron scattering theory is utilised within semi-classical models of LIED.

Chapter 3 presents a series of experiments that investigate the effect of the *molecular frame* on the Photoelectron Angular Distribution (PAD) of impulsively aligned and strong-field ionized CF_3I molecules using a Velocity Map Imaging Spectrometer (VMIS). It is shown that using the impulsive laser alignment technique enables taking *differential measurements* that bring out directly and clearly LIED effects in the PAD, even for a relatively *complex molecule* such as CF_3I and using a non-coincident detection setup such as the VMIS. The comparison of the experimental results at different laser intensities and at two different probe wavelengths, i.e. 800 and 1300 nm, shows that the LIED effect is robust and reproducible for a wide range of experimental conditions and at comparatively low re-collision energies.

Chapter 4 presents some first results from the combination of a table-top UED source with a Velocity Map Imaging Spectrometer (VMIS) that is applied to the study of secondary electron emission. By comparing the spectra of Helium and of H_2 to theoretical calculations, it is shown that hints of IICEE effects due to the molecular structure of H_2 may be visible in the experimental data. Because molecular structure effects are seen to be very weak, it is shown using theoretical calculations how such effects can be brought out more clearly in the secondary electron spectrum by *aligning* the molecules.

Chapter 2

Electron scattering theory

2.1 Introduction

Laser induced electron diffraction and electron impact ionization can be understood within the framework of electron scattering theory. Since the early days of Quantum Mechanics, a vast body of theoretical work has been devoted to the accurate modelling of electron scattering processes. Even nowadays, scattering theory remains an active field of research, as it is necessary to treat *continuum states* with a large range of possible kinetic energies, while taking many-body interactions into account. Due to this complexity, many different theoretical approaches have been developed to treat the collisional problem that often make use of simplifications applicable to the particular problem at hand. This chapter summarizes some of the basic principles from electron scattering theory and highlights approaches and approximations which are specifically needed to understand theoretical considerations and calculations in this thesis.

First, the basic ground work is laid out in Sec. 2.2, which summarizes some basic requirements on the solution of the scattering problem and defines observable quantities such as the differential cross-section. Section 2.3 then treats the most basic scattering problem: the scattering of a free electron by an arbitrary scalar potential. Techniques for solving the potential scattering problem, such as the Born series and the partial wave expansion, form the basis for solving scattering problems involving more complex targets. Section 2.4 proceeds with the treatment of *atom-electron* scattering problems where the basic potential scattering approach is extended in order to treat the possibility of the excitation or ionization of an atom. The treatment of low-energy collisions, where the projectile energy is comparable to the target electron energy, is relatively different from that of high-energy collisions and is therefore treated separately. Finally, Sec. 2.5 introduces the basic model for electron-molecule scattering used in this thesis, i.e. the Independent Atom Model (IAM), and treats the effects of molecular alignment on the observables.

2.2 Basic definitions

The typical scattering experiment is schematically represented in Fig. 2.1. The incoming projectile, which in the current work is always assumed to be an

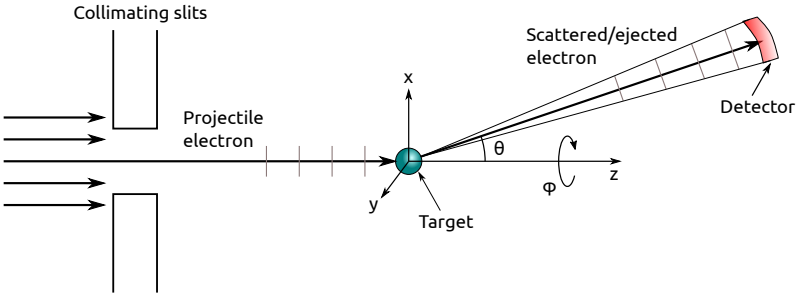

Figure 2.1: Basic scattering experiment.

electron, has a well-defined direction and energy. The target is an atom or molecule A assumed to be in its ground state with one or more bound electrons. These two conditions describe a well-defined initial state of the system.

The description of the *final* state is in general more complicated, as it can involve different *scattering channels* that represent different possible reactions of the target system. Assuming that there is no change in the internal state of the target system one arrives at the possibility of *elastic scattering*

$$e^- + A \rightarrow e^- + A \tag{2.1}$$

In the typical electron scattering experiment, the target, i.e. an atom or a molecule, is much heavier than the projectile so that the center-of-mass frame is approximately equal to the reference frame in which the target has zero velocity [25]. Under these conditions the energy of the projectile is unaltered by the elastic collision, but its direction may have been changed by some angle θ so that the observable in such experiments is the scattered electron direction. In the case of *inelastic scattering*, the internal state of the target is modified through the interaction with the projectile, leading to many possible reaction pathways. Some examples are

$$\begin{aligned} e^- + A &\rightarrow e^- + A^* && (2.2)\\ &\rightarrow 2e^- + A^+ && (2.3)\\ &\rightarrow 2e^- + A^{*+} && (2.4)\\ &\dots \end{aligned}$$

where A^* and A^{*+} represent excited neutral and ionic target states respectively. The two main reactions of interest in this thesis are (2.1) and (2.3) which represent *elastic scattering* and *electron impact ionization* respectively. The description of the initial and final states of the system in terms of scattering reactions implies a basic constraint on the final state due to energy conservation. The total initial energy must be equal to the final system energy, i.e.

$$\frac{k_i^2}{2} + E_i = \frac{k_s^2}{2} + E_j \tag{2.5}$$

where k_i is the incoming electron momentum, k_s the scattered electron momentum and E_j is the final state energy of the target, including the kinetic energy of ionized target electrons.

The full solution of the scattering problem requires the solution of the time-dependent Schrödinger equation

$$\mathrm{i}\hbar\frac{\partial}{\partial t}\Psi(\boldsymbol{r},t) = H(\boldsymbol{r})\Psi(\boldsymbol{r},t) \tag{2.6}$$

where $\Psi(\boldsymbol{r},t)$ is the full many-body wavefunction, which includes the projectile, and $H(\boldsymbol{r})$ is the total system Hamiltonian. In typical experiments the electron beam pulse duration is much longer than the time it takes the projectile to cross the interaction region so that the time-dependent equation can be solved by looking for *stationary solutions* of the form[1] [26, 27]

$$\Psi(\boldsymbol{r},t) = \psi(\boldsymbol{r})\exp(-\mathrm{i}Et/\hbar) \tag{2.7}$$

The problem thus reduces to solving the *time-independent* Schrödinger equation

$$E\psi(\boldsymbol{r}) = H\psi(\boldsymbol{r}) \tag{2.8}$$

where E is the system energy and H the full system Hamiltonian. For electron-atom scattering the Hamiltonian is explicitly given by [28]

$$H = \sum_{p=0}^{N}\left(-\frac{\hbar^2}{2m}\nabla^2_{\boldsymbol{r_p}} - \frac{Z}{r_p}\right) + \frac{1}{2}\sum_{p,q=0}^{N}\frac{1}{r_{pq}} \tag{2.9}$$

where Z is the nuclear charge, $\boldsymbol{r_1},\ldots,\boldsymbol{r_N}$ are the target electron coordinates and $\boldsymbol{r_0}$ is the projectile coordinate. The first term in (2.9) is the sum of the electron kinetic energy and the nucleus-electron potential energy operators, while the second term gives the sum of the electron-electron potential energy operators. In short, solving the electron-atom scattering problem requires obtaining the total time-independent wavefunction $\psi(\boldsymbol{r})$ of the many-particle Hamiltonian (2.9).

A major difference between solving the many particle time-independent Schrödinger equation for bound systems and for the scattering problem is, of course, the involvement of *continuum states*. In fact, in scattering experiments the observable is typically the energy or momentum of the outgoing electrons at some macroscopic distance far away from the scattering region. In order to obtain experimentally observable quantities it is therefore necessary to obtain the *asymptotic form* of the wavefunction $\psi(\boldsymbol{r})$. In most theoretical treatments the asymptotic form of the solution is actually imposed on the general solutions in the form of *boundary conditions*.

Two types of asymptotic forms for the scattering wavefunctions are considered in this thesis. Firstly, assuming that far from the scatterer there is no force on the scattered particle, the total wavefunction can be asymptotically given as a superposition of the incoming plane wave and a freely expanding outgoing spherical wave [29]

$$\psi_f^{(+)} \underset{r\to\infty}{\longrightarrow} \exp\left(\mathrm{i}\boldsymbol{k}\cdot\boldsymbol{r}\right) + f(k,\theta,\phi)\frac{\exp(\mathrm{i}kr)}{r} \tag{2.10}$$

[1] Even for the case of 'ultrafast' electron diffraction the typical electron pulse duration is on the order of femtoseconds whereas the typical collision/interaction time between the projectile and target electron is on the order of attoseconds.

The angular dependence of the scattering process is given by the *scattering amplitude* $f(k,\theta,\phi)$ which depends on the spherical polar angles θ and ϕ (Fig. 2.1) and the projectile momentum k. It can be shown that this asymptotic form holds for any potential with a *finite range*, i.e. for potentials decreasing faster than $1/r$ for $r \to \infty$ [30]. Secondly, for the case of scattering from a pure Coulomb potential of the form U_0/r, which has an infinite range, it can be shown (see also Sec. 2.3.3) that the correct asymptotic form of the wavefunction is given by [29]

$$\psi_f^{(+)} \underset{r\to\infty;\ \theta\neq 0}{\longrightarrow} \exp\{\mathrm{i}\boldsymbol{k}\cdot\boldsymbol{r} + \mathrm{i}\gamma\log[kr(1-\cos\theta)]\} + f(k,\theta)\frac{\exp\{\mathrm{i}kr - \mathrm{i}\gamma\log(2kr)\}}{r} \quad (2.11)$$

where $\gamma = U_0/2k$ is the Sommerfeld parameter. The logarithmic phase factor in this asymptotic form is a manifestation of the fact that for the Coulomb potential neither the scattered nor the incoming wavefunction can be considered to be a plane wave and that the potential has a distorting influence on the them even at very great distance. The treatment of electron impact ionization in Sec. 2.4.2 is an example of a case where Coulomb effects can become important.

Having obtained the asymptotic forms of the scattered wavefunction it is then possible to calculate the probability of detecting an outgoing electron with a certain momentum, i.e. energy and direction. This probability is expressed in terms of the *differential cross-section* which gives the probability flux of scattered particles per unit time into a certain solid angle. For elastic scattering the *double differential cross-section* is given by

$$\frac{\mathrm{d}^2\sigma}{dk\ \mathrm{d}\Omega} = |f(k,\Omega)|^2 \quad (2.12)$$

where $\Omega = (\theta,\phi)$ is the solid angle of the scattered electron and $f(k,\Omega)$ is obtained from the asymptotic form of the wavefunction (2.10) or (2.11). The concept of cross-section can be generalized to include further variables which are relevant to the reaction at hand, e.g. molecular orientation in electron-molecule scattering. For the electron impact ionization reaction, (2.12) must be modified slightly in order to ensure probability flux conservation. The *triple differential cross-section* for electron impact ionization is given by

$$\frac{\mathrm{d}^3\sigma}{\mathrm{d}k_e\,\mathrm{d}\Omega_e\,\mathrm{d}\Omega_s} = \frac{k_s k_e}{k_i}|f(k_e,\Omega_e,\Omega_s)|^2 \quad (2.13)$$

where k_e and k_s are the momentum magnitudes and Ω_e and Ω_s are the solid angles of the ejected and scattered electron respectively. The projectile momentum is considered here as a parameter and its magnitude is given by k_i. The magnitude of the scattered electron momentum k_s depends on the values of k_i and k_e through the energy conservation relation (2.5). The flux conservation factor is given by the multiplicative term $k_e k_s/k_i$ [29].

2.3 Potential scattering

The simplest scattering problem is that of a single charged particle by an arbitrary scalar potential $V(\boldsymbol{r})$. The charged particle is assumed to be structureless,

e.g. an electron, so that it has no internal states or constituent parts that can be affected by the collision. The scattering of such a particle by a potential is therefore *elastic*. Though this is necessarily an idealized and simplified situation, which rarely is present in real experiments, the theory of potential scattering provides a basic framework within which generalizations involving more complex systems can be understood.

This section will focus on two important approaches for calculating the potential scattering cross-sections: the partial wave expansion (Sec. 2.3.1) and the integral formulation which leads to e.g. the Born series (Sec. 2.3.2). These two approaches are used for complementary energy ranges. For low energy scattering partial wave expansions are usually more appropriate, whereas for high energy scattering the integral formulation and the Born series are more frequently used. Both the partial wave expansion and the integral formulation assume a finite range for the scattering potential so that they can not be used for scattering from the Coulomb potential without appropriate modification. This case is treated in Sec. 2.3.3.

2.3.1 Partial wave formulation

The partial wave method specifies a procedure for solving the time-independent Schrödinger equation that uses a spherical harmonic expansion of the scattered particle wavefunction in order to calculate the so-called *phase shifts* for each component of the angular momentum separately. The phase shifts are obtained by comparing the asymptotic form of the *radial part* of the wavefunction to that of a freely propagating plane wave. Determination of the phase shifts completely specifies the scattering amplitude $f(k, \theta, \phi)$, and thus the scattering cross-section (2.12). Non-spherical potentials can also be treated with the partial wave method, provided they are expanded in a spherical harmonic basis. The derivation of the partial wave potential scattering equations below follows largely that given by Bransden and Joachain [29].

The basic principles of the partial wave method can be nicely illustrated by considering scattering from a simple spherically symmetric potential $V(r)$. In this case the time-independent Schrödinger equation is explicitly given by

$$\left[-\frac{\hbar^2}{2m}\nabla^2 + V(r)\right]\psi(\boldsymbol{r}) = E\psi(\boldsymbol{r}) \tag{2.14}$$

where E is the energy of the projectile. It is well known that the Hamiltonian of (2.14) is separable in spherical polar coordinates. Moreover, since the scattering process possesses azimuthal symmetry around the incident projectile direction, the unknown wavefunction $\psi(\boldsymbol{r})$ must do so as well. Expanding the wavefunction $\psi(\boldsymbol{r})$ in spherical harmonics, and making use of the azimuthal symmetry, results in the following expression

$$\psi_f^{(+)}(k, r, \theta) = \sum_{\ell=0}^{\infty} R_\ell(k, r) P_\ell(\cos\theta) \tag{2.15}$$

The Legendre polynomials $P_\ell(\cos\theta)$ completely determine the *angular dependence* of the wavefunction for each angular momentum value ℓ. The radial dependence of the wavefunction is given by $R_\ell(k, r)$, and by substituting (2.15)

back into (2.14) it is found that the $R_\ell(k,r)$ satisfy the following equations

$$\left[\frac{\mathrm{d}^2}{dr^2}+\frac{2}{r}\frac{\mathrm{d}}{dr}-\frac{\ell(\ell+1)}{r^2}-U(r)+k^2\right]R_\ell(k,r)=0 \tag{2.16}$$

where $U(r)=2mV(r)/\hbar^2$ and $k^2=2mE/\hbar^2$.

As was pointed out at the beginning of this section, in order to obtain an expression for the scattering amplitude, and hence the differential cross-section, the asymptotic behaviour of the radial functions $R_\ell(k,r)$ must be examined. Assuming that the potential has a *finite range*, the radial functions should asymptotically match those of the free particle solution. The free particle equation is obtained from (2.16) by setting the potential function $U(r)=0$. The general solution to this equation is given by a linear combination of the spherical Bessel function

$$j_\ell=\left(\frac{\pi}{2kr}\right)^{1/2}J_{\ell+1/2}(kr) \tag{2.17}$$

and the spherical Neumann function

$$n_\ell=(-1)^{\ell+1}\left(\frac{\pi}{2kr}\right)^{1/2}J_{-\ell-1/2}(kr) \tag{2.18}$$

where $J_\nu(kr)$ is a Bessel function of order ν. For $kr\to\infty$ these functions behave asymptotically as

$$j_\ell \underset{kr\to\infty}{\longrightarrow} \frac{1}{kr}\sin(kr-\ell\pi/2) \tag{2.19}$$

$$n_\ell \underset{kr\to\infty}{\longrightarrow} -\frac{1}{kr}\cos(kr-\ell\pi/2) \tag{2.20}$$

Returning to (2.15) it can be concluded that the asymptotic form of the radial functions $R_\ell(k,r)$ *outside the scattering potential range* must also be given by a linear combination of the spherical Bessel and Neumann functions, so that

$$R_\ell(k,r) \underset{kr\to\infty}{\longrightarrow} B_\ell(k)j_l(kr)+C_\ell(k)n_l(kr) \tag{2.21}$$

where B_ℓ and C_ℓ are some constants of integration that do not depend on the free variable r. Using the asymptotic expressions for $j_\ell(kr)$ and $n_\ell(kr)$ given by (2.19) and (2.20), the asymptotic expression for $R_\ell(k,r)$ can be written as

$$R_\ell(k,r) \underset{r\to\infty}{\longrightarrow} \frac{A_\ell(k)}{kr}\sin\left[kr-\ell\pi/2+\delta_\ell(k)\right] \tag{2.22}$$

where $A_\ell=\sqrt{B_\ell^2+C_\ell^2}$ and $\tan\delta_\ell=-C_\ell/B_\ell$. Finally, substituting this result back into the partial wave expansion (2.15), the asymptotic form of the wavefunction is given by

$$\psi \underset{r\to\infty}{\longrightarrow} \sum_{\ell=0}^{\infty}\frac{1}{2ikr}\Big\{\exp[\mathrm{i}(kr-\ell\pi/2+\delta_\ell(k)]- \exp[-\mathrm{i}(kr-\ell\pi/2+\delta_\ell(k)]\Big\}\times P_\ell(\cos\theta) \tag{2.23}$$

In order to obtain an explicit expression for the scattering amplitude, which can then be used to calculate the scattering cross-section, the two asymptotic

expressions for the wavefunction given by (2.10) and (2.23) are compared to each other. Using the expansion of a plane wave in Legendre polynomials

$$\exp(\mathrm{i}kz) = \sum_{\ell=0}^{\infty}(2\ell+1)\mathrm{i}^{\ell}j_{\ell}(kr)P_{\ell}(\cos\theta) \tag{2.24}$$

together with the asymptotic expression for the spherical Bessel function (2.19), (2.10) can be rewritten as

$$\psi \underset{r\to\infty}{\longrightarrow} \sum_{\ell=0}^{\infty}(2\ell+1)\mathrm{i}^{\ell}\frac{\sin(kr-\ell\pi/2)}{kr}P_{\ell}(\cos\theta) + f(k,\theta,\phi)\frac{\exp(ikr)}{r} \tag{2.25}$$

Rewriting the *sin* term using complex exponentials, (2.25) can be brought to the following form

$$\psi \underset{r\to\infty}{\longrightarrow} \frac{\exp(ikr)}{r}\left[f(k,\theta,\phi) - \sum_{\ell=0}^{\infty}\frac{\mathrm{i}}{2k}(2\ell+1)P_{\ell}(\cos\theta)\right] + \frac{\exp(-ikr)}{r}\left[\sum_{\ell=0}^{\infty}(-1)^{\ell}\frac{\mathrm{i}}{2k}(2\ell+1)P_{\ell}(\cos\theta)\right] \tag{2.26}$$

Finally, by matching the coefficients of the $\exp(ikr)/r$ and $\exp(-ikr)/r$ terms in (2.26) and (2.23), the following expression for the scattering amplitude is obtained

$$f(k,\theta) = \sum_{\ell=0}^{\infty} f_{\ell}(k)P_{\ell}(\cos\theta) \tag{2.27}$$

where $f_{\ell}(k)$ is the partial wave scattering amplitude given by

$$f_{\ell}(k) = \frac{2\ell+1}{2\mathrm{i}k}\left\{\exp[2\mathrm{i}\delta_{\ell}(k)] - 1\right\} \tag{2.28}$$

and $\delta_{\ell}(k)$ are the partial wave *phase shifts*. The quantity $\exp[2\mathrm{i}\delta_{\ell}(k)]$ is also called the S-matrix element. To actually compute the phase shifts δ_{ℓ} one must in general numerically solve the radial differential equation (2.16) in some internal region $r < a$ where the potential is effective[2]. The internal solution is then matched to the asymptotic expression for the phase-shifted, scattered wavefunction (2.23) at the boundary $r = a$ so that the wavefunction and its derivative are continuous, thereby obtaining the phase shifts δ_{ℓ}. Having thus obtained the S-matrix elements all the information needed to calculate differential cross-sections and determine experimental observables is available.

Figure 2.2 illustrates some interesting aspects of the partial wave method. The two potential energy terms in the radial equation (2.16) are the scattering potential term and a centrifugal term so that the effective potential each partial wave sees is given by

$$U_{eff} = U(r) + \frac{\ell(\ell+1)}{r^2} \tag{2.29}$$

[2]This of course assumes that there *is* a finite internal region outside of which the potential is assumed zero and the asymptotic form (2.25) correctly represents the wavefunction. This assumption is valid for potentials decreasing faster than $1/r$. For a pure Coulomb potential the approach must be modified (see Sec. 2.3.3).

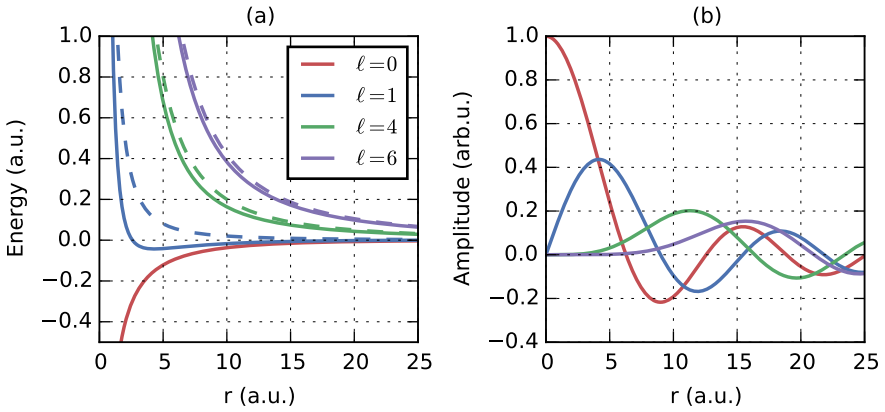

Figure 2.2: (a) Total potential energy terms $\ell(\ell+1)/r^2+U(r)$ from the radial equation (2.16) for a Yukawa scattering potential $U(r) = -\exp(-\alpha r)/r$ with $\alpha = 0.1$ and for different values of the angular momentum ℓ. The dashed line shows the centrifugal part of the potential only, i.e. $\ell(\ell+1)/r^2$. (b) Spherical Bessel functions $j_\ell(kr)$ given by (2.17) for $k = 0.5$ a.u. and the same values of ℓ as in (a).

From Fig. 2.2(a) it is clear that for higher angular momentum ℓ the total effective potential is dominated more and more by the centrifugal term. This implies that the solution for the radial equation should resemble that of a free wave and thus that the phase shifts δ_ℓ should eventually tend to zero. The question is: how fast do the phase shifts tend to zero? This point is illustrated in Fig. 2.2(b) which shows the spherical Bessel functions, which are the free particle solutions of the radial equation, for a momentum of $k = 0.5$ a.u.[3] For values of k or r close to zero the behaviour of these functions is given by

$$j_\ell(kr) \underset{kr\to\infty}{\longrightarrow} \frac{(kr)^\ell}{(2\ell+1)!!} \tag{2.30}$$

In other words for small values of r or k and higher values of ℓ the wavefunction goes rapidly to zero and does so for a larger range of r. Physically this is due to the fact that the centrifugal barrier becomes larger and wider for high ℓ and/or small k so that the projectile has to penetrate it to reach small r regions. At the same time, as shown in Fig. 2.2(a), the difference between the true effective potential, which includes the scattering potential, and the centrifugal term is only appreciable for small r. This means that for high ℓ and/or small k the partial waves effectively do not see this region. In the extreme case of a very slow particle it can be sufficient to calculate the s-wave, i.e. $\ell = 0$, partial wave phase shift only. The partial wave formulation is therefore well suited for problems which require a low number of angular momentum values to be calculated, which is especially true for slow projectiles. For a high energy projectile a large number of phase shifts needs to be calculated because high ℓ partial waves can

[3]Here, and elsewhere in this thesis, a.u. stands for *Hartree atomic units*. These are obtained by setting the numerical value of the fundamental constants of the electron charge e and mass m_e, the reduced Plank's constant $\hbar$, and Coulomb's constant $k_e = 1/(4\pi\epsilon_0)$ to unity.

still penetrate far into the low r region where the scattering potential influence is strong.

2.3.2 Integral equation formulation

As was shown in the previous section the partial wave method is well suited for low energy collisions as it requires a relatively small number of phase shifts to be computed. For high energy collisions an approach based on a *perturbative expansion* may be more suitable. Such an approach follows naturally from the *Lippman-Schwinger equation*, which is an integral equation formulation of the time-independent Schrödinger equation for the scattering problem. The iterative solution of the Lippman-Schwinger equation leads to the *Born series* which is a well-known and frequently used method for solving scattering problems. The derivation of the integral equation formulation for potential scattering in this section largely follows the treatment by Merzbacher [26].

As in the previous section the starting point in this treatment is the Schrödinger equation (2.14) which can be rewritten as

$$H_0\psi = U\psi \tag{2.31}$$

where H_0 is the free particle Hamiltonian

$$H_0 = \left[\nabla^2 + k^2\right] \tag{2.32}$$

with $k^2 = 2mE/\hbar^2$ and $U = 2mV/\hbar^2$. The reformulation of this equation to an integral equation is most conveniently done by considering the term $U\psi$ as an *inhomogeneity* or source term. This differential equation can be solved using the *Green's function* formalism, which states that the solution to (2.31) can be constructed from the solutions to the equation

$$H_0 G(\boldsymbol{r}, \boldsymbol{r'}) = -4\pi\delta(\boldsymbol{r} - \boldsymbol{r'}) \tag{2.33}$$

where $G(\boldsymbol{r}, \boldsymbol{r'})$ is a Green's function. Once the Green's function is known, a particular solution of the original equation (2.31) is given by

$$-\frac{1}{4\pi}\int G(\boldsymbol{r}, \boldsymbol{r'})U(\boldsymbol{r'})\psi(\boldsymbol{r'})\,\mathrm{d}\boldsymbol{r'} \tag{2.34}$$

That this is a solution may be verified by substituting (2.34) for the wavefunction ψ on the left hand side of (2.31) and using (2.33). It can be shown that the explicit form of the Green's function for (2.33) is given by [26, 29]

$$G(\boldsymbol{r}, \boldsymbol{r'}) = \frac{\exp(\mathrm{i}k|\boldsymbol{r} - \boldsymbol{r'}|)}{|\boldsymbol{r} - \boldsymbol{r'}|} \tag{2.35}$$

which corresponds to a homogeneously expanding spherical wave centred at $\boldsymbol{r} - \boldsymbol{r'}$. The general solution of the original Schrödinger equation (2.31) is a sum of the particular solution (2.34) and an arbitrary solution of the *homogeneous* differential equation

$$H_0\psi_0 = 0 \tag{2.36}$$

This is a generalization of the standard approach to solving ordinary differential equations with a source term, see e.g. [31]. The solution of (2.36) is a freely

propagating plane wave with momentum k that corresponds to the incoming projectile. Adding the homogeneous equation solution to Green's solution finally leads to the following integral equation for the wavefunction

$$\psi(\boldsymbol{r}) = N\exp(\mathrm{i}\boldsymbol{k}\cdot\boldsymbol{r}) - \frac{1}{4\pi}\int G(\boldsymbol{r},\boldsymbol{r'})U(\boldsymbol{r'})\psi(\boldsymbol{r'})\,\mathrm{d}\boldsymbol{r'} \tag{2.37}$$

Equation (2.37) is the *Lippman-Schwinger equation* that gives the solutions to the original scattering problem in terms of an *integral equation*, and is completely equivalent to the original Schrödinger equation.

In order to make the connection between the Lippman-Schwinger equation and the scattering amplitude, the asymptotic behaviour of (2.37) for $r \to \infty$ must be examined. Expanding the term in the exponent in (2.35) gives

$$k|\boldsymbol{r}-\boldsymbol{r'}| = kr - k\hat{\boldsymbol{r}}\cdot\boldsymbol{r'} + \frac{k(\hat{\boldsymbol{r}}\times\boldsymbol{r'})^2}{2r} + \ldots \tag{2.38}$$

where $\hat{\boldsymbol{r}}$ is the unit vector of $\boldsymbol{r}$. At this point it is necessary to assume that the potential $U(\boldsymbol{r'})$ becomes zero after some distance a. Since the potential now has a *finite range* the expansion above may be truncated after the first two terms, provided r is chosen such that $r \gg ka^2$. This condition is easily fulfilled for realistic experiments since r is the macroscopic distance to the detection apparatus. Performing a similar expansion for the denominator in (2.35) and only keeping the first term, the asymptotic form of the Lippman-Schwinger equation is given by

$$\psi \underset{r\to\infty}{\longrightarrow} N\exp(\mathrm{i}\boldsymbol{k}\cdot\boldsymbol{r}) - \frac{1}{4\pi}\frac{\exp(\mathrm{i}kr)}{r}\int \exp(-\mathrm{i}\boldsymbol{k_f}\cdot\boldsymbol{r'})U(\boldsymbol{r'})\psi(\boldsymbol{r'})\,\mathrm{d}\boldsymbol{r'} \tag{2.39}$$

where $\boldsymbol{k_f} = k\hat{\boldsymbol{r}}$ represents the final momentum that is measured and which is determined by the placement of the detector in a certain direction $\hat{\boldsymbol{r}}$. For the case of potential scattering the final momentum is of course equal in magnitude to the incoming momentum. Comparing (2.39) to (2.10) it is seen that the scattering amplitude is given by the following expression

$$f = -\frac{1}{4\pi}\int \exp(-\mathrm{i}\boldsymbol{k_f}\cdot\boldsymbol{r'})U(\boldsymbol{r'})\psi(\boldsymbol{r'})\,\mathrm{d}\boldsymbol{r'} \equiv -\frac{1}{4\pi}\langle\boldsymbol{k_f}|\,U\,|\psi\rangle \tag{2.40}$$

where $\langle\boldsymbol{k_f}\,|\,\boldsymbol{r}\rangle = \exp(-\mathrm{i}\boldsymbol{k_f}\cdot\boldsymbol{r'})$.

Solving (2.37) is in general a non-trivial task, so that the reformulation of the original Schrödinger equation in terms of the Lippman-Schwinger integral equation seems not to be of particular use. However, the *Born series* can be used to obtain an approximate solution to the Lippman-Schwinger equation in many practical situations. To see how the Born series arises from the Lippman-Schwinger equation the latter is first rewritten in Dirac notation as follows

$$|\psi\rangle = |\psi_0\rangle + \mathcal{GU}\,|\psi\rangle \tag{2.41}$$

where $\mathcal{GU}$ is a Green's integral operator defined by (2.34) and $\langle\boldsymbol{r}\,|\,\psi_0\rangle = N\exp(\mathrm{i}\boldsymbol{k}\cdot\boldsymbol{r})$, which corresponds to the incoming plane wave. Solving this equation *formally* is very simple and results in the following expression for the wavefunction

$$|\psi\rangle = \frac{1}{1-\mathcal{GU}}\,|\psi_0\rangle \tag{2.42}$$

In order to get a practical expression for the inverse operator on the right hand side of this equation its series expansion can be taken. Using the geometric series[4] this leads to the following result

$$|\psi\rangle = \left[1 + \sum_{n=1}^{\infty} (\mathcal{GU})^n\right] |\psi_0\rangle \tag{2.43}$$

which is also known as the Born series. The Born series also results quite naturally from the Lippman-Schwinger equation (2.41) if one attempts to find its solution iteratively [29]. Starting from the incident plane-wave as the zero-order approximation the following sequence is obtained

$$\begin{aligned} |\psi_1\rangle &= |\psi_0\rangle + \mathcal{GU}\,|\psi_0\rangle \\ &\vdots \\ |\psi_n\rangle &= |\psi_0\rangle + \mathcal{GU}\,|\psi_{n-1}\rangle \end{aligned} \tag{2.44}$$

Returning now to expression (2.40), which provides the necessary relation to obtain the scattering amplitude, and substituting the Born series expansion (2.43) the desired scattering amplitude can be written as the following summation

$$f = \sum_{n=1}^{\infty} f^{Bn} \tag{2.45}$$

where the Born scattering amplitude terms are given by

$$f^{Bn} = -\frac{1}{4\pi} \langle \boldsymbol{k_f} | \, U(\mathcal{GU})^{n-1} \, |\psi_0\rangle \tag{2.46}$$

The Born series expansion has a very intuitive physical picture where each term in the series (2.46) represents a scattering amplitude where the scattering particle has interacted n times with the scattering potential before ending up in the final state $|\boldsymbol{k_f}\rangle$ (see also Fig. 2.3). In order to see how this interpretation follows from (2.46) this expression is written out explicitly for the first two Born scattering amplitudes using the definition of the integral operator $\mathcal{GU}$ (2.34). This leads to the following expressions

$$f^{B1} = -\frac{1}{4\pi} \int \psi_f^*(\boldsymbol{r'}) U(\boldsymbol{r'}) \psi_0(\boldsymbol{r'}) \, \mathrm{d}\boldsymbol{r'} \tag{2.47}$$

$$f^{B2} = -\frac{1}{4\pi} \int \psi_f^*(\boldsymbol{r'}) U(\boldsymbol{r'}) G(\boldsymbol{r'}, \boldsymbol{r''}) U(\boldsymbol{r''}) \psi_0(\boldsymbol{r''}) \, \mathrm{d}\boldsymbol{r'} \, \mathrm{d}\boldsymbol{r''} \tag{2.48}$$

where $\psi_f^*(\boldsymbol{r'}) = \langle \boldsymbol{k_f} \,|\, \boldsymbol{r'} \rangle$. The integrand in the first term (2.47) can now be interpreted as the possibility that the incoming plane wave ψ_0 interacts with the potential U a single time at some point $\boldsymbol{r'}$ and then ends up in the final state ψ_f. The total probability of this process is given by the integration over all possible scattering points $\boldsymbol{r'}$ and is modulated by the strength of the potential U at those particular points. The integrand in the second term (2.48) can analogously be interpreted as the possibility that the incoming plane wave ψ_0 interacts with the potential at some point $\boldsymbol{r''}$, then propagates in an intermediate form, which

[4] The geometric series is the infinite series expansion of $\frac{1}{1-x} = \sum_n^{\infty} x^n$, see e.g. [31].

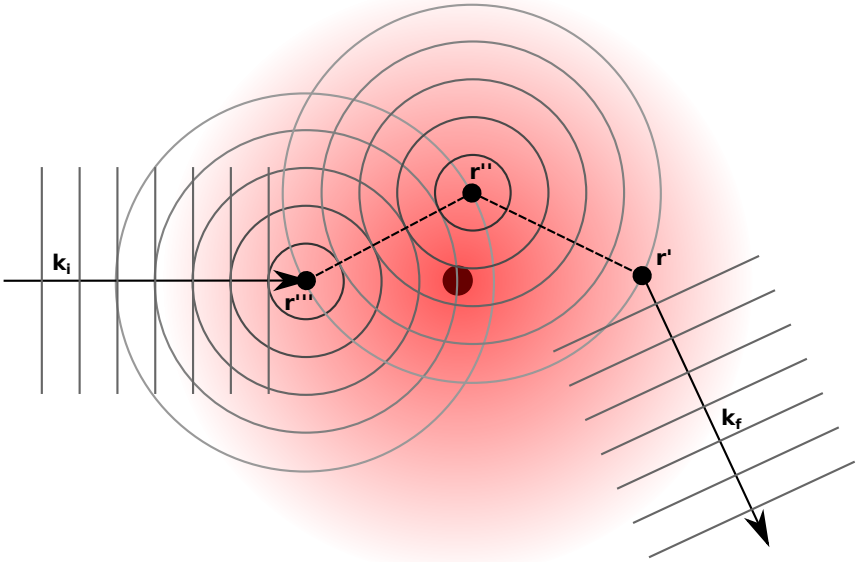

Figure 2.3: Graphical illustration of the third Born scattering amplitude interpretation in which the scattered particle sequentially interacts three times with a potential U (whose magnitude at a point $\boldsymbol{r}$ is represented by the red gradient) at points $\boldsymbol{r'''}$, $\boldsymbol{r''}$ and $\boldsymbol{r'}$ and propagates as a freely expanding spherical wave between these interactions (concentric circles). The initial and final states are plane waves with momentum $\boldsymbol{k_i}$ and $\boldsymbol{k_f}$ respectively.

is specified by the Green's function $G(\boldsymbol{r'}, \boldsymbol{r''})$, before interacting a *second time* at point $\boldsymbol{r'}$ and ending up in the final state ψ_f. The actual form of the Green's function is specified by (2.33). For example, for the unperturbed Hamiltonian given by (2.32) it is a *homogeneously expanding spherical wave* given by (2.35). The total scattering amplitude (2.45) thus takes into account all possible number of interactions $n = 1, 2, \ldots$ with the potential and integrates over all possible intermediate paths that the particle can take.

Using this physical picture, one can conclude that the Born series should converge faster if the projectile energy is high enough so that it cannot interact with the scattering potential too many times, i.e. if the interaction is weak enough. Depending on the strength of the interaction one should therefore be able to take a finite number of Born series terms to calculate the total scattering amplitude. The Born series is thus a *perturbative expansion* of the interaction potential between the incoming projectile and the target. In many practical cases, for which the projectile energy is large with respect to the interaction potential, the first Born term is sufficient to calculate the scattering cross-section. Assuming that the incoming and outgoing wavefunctions, ψ_0 and ψ_f, can be described by plane waves with momentum $\boldsymbol{k_i}$ and $\boldsymbol{k_f}$, the *First Born Approximation* (FBA) can be written as

$$f^{B1} = -\frac{1}{4\pi} \int \exp(\mathrm{i}\boldsymbol{q} \cdot \boldsymbol{r}) U(\boldsymbol{r}) \, \mathrm{d}\boldsymbol{r} \tag{2.49}$$

where $\boldsymbol{q} = \boldsymbol{k_i} - \boldsymbol{k_f}$ is the *momentum transfer* variable. The first Born amplitude

is therefore given by the *Fourier transform* of the interaction potential in the variable $\boldsymbol{q}$.

2.3.3 Coulomb scattering

In the previous two sections scattering amplitudes and cross-sections were obtained by comparing the asymptotic form of the wavefunction to a certain boundary condition given by (2.10). This boundary condition explicitly assumes that the wave is free from the potential at some point. This treatment excludes a quite important type of potential: the Coulomb potential. The Coulomb potential is 'problematic' because it has an infinite range. This means that in principle the wavefunction is never completely free of the potential and that the asymptotic form of the outgoing wavefunction cannot be represented by the pure spherical wave assumed in (2.10). Fortunately, it is possible to solve the Coulomb scattering problem analytically and derive the required modifications to treat this important case. The solution of the Coulomb scattering problem that is outlined below follows the treatment by Bransden and Joachain [29].

The Schrödinger equation for scattering of a simple particle from a Coulomb potential $V(r) = U_0/r$ can be solved exactly using parabolic coordinates. The parabolic coordinates (ζ, η, ϕ) are related to Cartesian coordinates (x, y, z) as follows

$$x = \sqrt{\zeta\eta}\cos\phi \qquad y = \sqrt{\zeta\eta}\sin\phi \qquad z = \frac{1}{2}(\zeta - \eta) \tag{2.50}$$

$$\zeta = r + z \qquad \eta = r - z \qquad \phi = \arctan y/x \tag{2.51}$$

where $r = \frac{1}{2}(\zeta + \eta)$. By treating the Schrödinger equation in parabolic coordinates one direction in space can be singled out for which the problem is symmetric. The Coulomb scattering problem is azimuthally symmetric around the propagation direction of the incoming projectile. From (2.50) it can be seen that this direction is parallel to the z-axis, since the coordinate transformation from parabolic to Cartesian coordinates does not depend on the azimuthal angle ϕ. Writing the Schrödinger equation for scattering from the Coulomb potential in parabolic coordinates leads to the following expression

$$\left[\nabla^2 + k^2 - \frac{2U_0}{\zeta + \eta}\right]\psi_c = 0 \tag{2.52}$$

where the Laplacian operator in parabolic coordinates is given by

$$\nabla^2 = \frac{4}{\zeta + \eta}\left[\frac{\partial}{\partial\zeta}\left(\zeta\frac{\partial}{\partial\zeta}\right) + \frac{\partial}{\partial\eta}\left(\eta\frac{\partial}{\partial\eta}\right)\right] + \frac{1}{\zeta\eta}\frac{\partial^2}{\partial\phi^2} \tag{2.53}$$

As the wavefunction ψ_c should exhibit azimuthal symmetry around the projectile direction, the solution is assumed to be of the following form

$$\psi_c = f(\zeta)g(\eta) \tag{2.54}$$

Substituting this *ansatz* into the parabolic Schrödinger equation results in two

differential equations

$$\frac{\partial}{\partial\zeta}\left(\zeta\frac{\partial f}{\partial\zeta}\right)+\left(\frac{1}{4}k^2\zeta-\nu_1\right)f=0 \tag{2.55}$$

$$\frac{\partial}{\partial\eta}\left(\eta\frac{\partial g}{\partial\eta}\right)+\left(\frac{1}{4}k^2\eta-\nu_2\right)g=0 \tag{2.56}$$

where ν_1 and ν_2 are separation constants such that

$$\nu_1+\nu_2=U_0/2 \tag{2.57}$$

It can be shown that a solution of (2.55) is given by the function

$$f(\zeta)=\exp\left(\frac{1}{2}\mathrm{i}k\zeta\right) \tag{2.58}$$

provided $\nu_1=ik/2$. Using (2.57) and introducing

$$g(\eta)=exp\left(-\frac{1}{2}ik\eta\right)h(\eta) \tag{2.59}$$

Eq. (2.56) is can be rewritten as

$$\eta\frac{\mathrm{d}^2h}{\mathrm{d}\eta^2}+(1-ik\eta)\frac{dh}{\mathrm{d}\eta}-\gamma kh=0 \tag{2.60}$$

which is also known as the *Kummer-Laplace differential equation* where $\gamma=U_0/2k$ is the *Sommerfeld parameter*. The regular solution of this equation is given by the confluent hypergeometric function

$$h(\eta)=C\,{}_1\mathrm{F}_1(-\mathrm{i}\gamma,1,ik\eta) \tag{2.61}$$

where C is an integration constant. Substituting (2.58), (2.59) and (2.61) into (2.54), and normalizing so that the incoming wave amplitude is unity, results in the following expression

$$\psi_c=\exp(-\pi\gamma/2)\Gamma(1+\mathrm{i}\gamma)\exp(ikz)\,{}_1\mathrm{F}_1(-\mathrm{i}\gamma,1,ik\eta) \tag{2.62}$$

for the *Coulomb wavefunction* (see also Fig. 2.4).

As explained in Sec. 2.2, in order to obtain the scattering amplitudes and cross-section it is necessary to examine the asymptotic behaviour of the Coulomb wavefunction as $r\to\infty$. It can be shown, using the asymptotic form of the confluent hypergeometric function [29, 32], that the asymptotic form of the Coulomb wavefunction is given by

$$\psi_f^{(+)}\underset{r\to\infty;\ \theta\neq0}{\longrightarrow}\exp\left\{\mathrm{i}\boldsymbol{k}\cdot\boldsymbol{r}+\mathrm{i}\gamma\log[kr(1-\cos\theta)]\right\}\left[1+\frac{\gamma^2}{\mathrm{i}kr(1-\cos\theta)}+\ldots\right]+$$

$$f_c(k,\theta)\frac{\exp\{\mathrm{i}kr-\mathrm{i}\gamma\log(2kr)\}}{r}\left[1+\frac{(1+\mathrm{i}\gamma)^2}{\mathrm{i}kr(1-\cos\theta)}+\ldots\right] \tag{2.63}$$

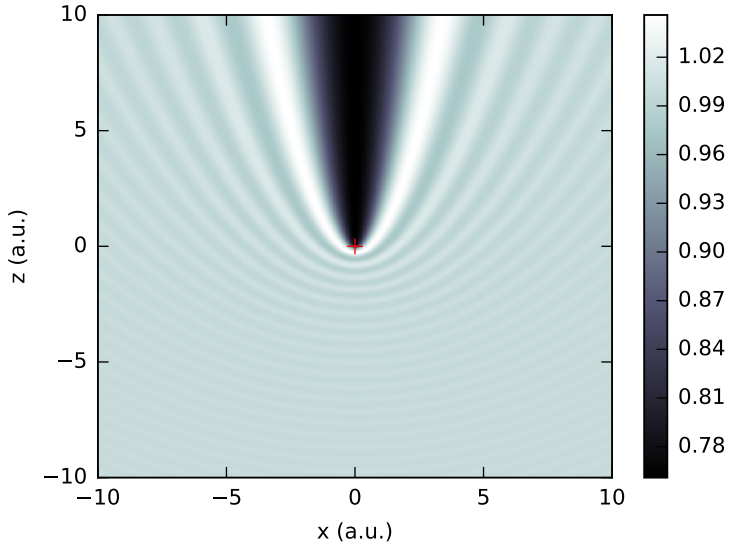

Figure 2.4: Probability density, i.e. $|\psi_c|^2$, of a Coulomb wavefunction with a momentum of $k = 6$ a.u. directed along the y-axis direction. The position of the scatterer at the origin is marked by the red cross.

where $f_c(k, \theta)$ is the *Coulomb scattering amplitude* given by

$$f_c(k,\theta) = -\frac{U_0}{4k^2 \sin^2(\theta/2)} \exp\{-\mathrm{i}\gamma \log[\sin^2(\theta/2)] + 2\mathrm{i} \arg[\Gamma(1+\mathrm{i}\gamma)]\} \quad (2.64)$$

Finally, the differential cross-section for scattering from the pure Coulomb potential can be calculated and is given by

$$\frac{\mathrm{d}^3\sigma_c}{\mathrm{d}k\,\mathrm{d}\theta\,\mathrm{d}\phi} = \frac{U_0}{16k^4 \sin^4(\theta/2)} \quad (2.65)$$

This expression is identical to the *Rutherford formula* that gives the *classical* cross-section for scattering by a Coulomb potential. In both the quantum mechanical and the classical treatment the Coulomb differential cross-section increases without bound as $\theta \to 0$ because the potential has an infinite range[5].

It is interesting to compare these results to the First Born Approximation (FBA) for Coulomb scattering. The FBA scattering amplitude is given by (2.49)

$$f^{B1} = -\frac{1}{4\pi} \int U_0 \frac{\exp(\mathrm{i}\boldsymbol{q}\cdot\boldsymbol{r})}{r}\,\mathrm{d}\boldsymbol{r} \quad (2.66)$$

where $\boldsymbol{q} = \boldsymbol{k_i} - \boldsymbol{k_f}$. This integral can be evaluated using the *Bethe integral*[6]

[5]Interestingly, the cross-section for classical scattering from a potential is always infinite as $\theta \to 0$ unless the potential is strictly zero outside some finite range. In quantum mechanical scattering this is not true, and for any potential that decreases faster than $1/r^3$ the cross-section converges to a finite value.

[6]The Bethe integral can be derived by evaluating the FBA for a Yukawa potential $U(r) = U_0 \exp(-\alpha r_{01})/r_{01}$ first. This is readily evaluated and gives $-U_0/(\alpha^2 + q^2)$. The Bethe integral follows from this result by taking the limit $\alpha \to 0$.

which gives the following relation

$$-\frac{1}{4\pi}\int \frac{\exp(\mathrm{i}\boldsymbol{q}\cdot\boldsymbol{r_0})}{|\boldsymbol{r_0}-\boldsymbol{r_1}|}\,\mathrm{d}\boldsymbol{r_0} = -\frac{\exp(\mathrm{i}\boldsymbol{q}\cdot\boldsymbol{r_1})}{q^2} \tag{2.67}$$

Using this expression to evaluate (2.66) and substituting $q = 2k\sin(\theta/2)$, which gives the momentum transfer magnitude in terms of the scattering angle θ for elastic scattering, leads to the following expression for the FBA scattering amplitude

$$f_c^{B1} = -\frac{U_0}{4k^2\sin^2(\theta/2)} \tag{2.68}$$

Comparing this expression to (2.64) it is clear that the true Coulomb scattering amplitude deviates from the FBA amplitude by a logarithmic phase factor. This phase factor has of course no influence on the differential cross-section which is indeed again given by (2.65). However, when the Coulomb scattering amplitude must be added coherently to other amplitudes, this phase factor does become important.

The final point considered in this section is the treatment of Coulomb scattering within the partial wave method. In the partial wave method phase shifts are determined by matching the asymptotic form of the radial part of the wavefunction to that of a plane wave. It is possible to generalize this approach by attempting to match the radial wavefunction to a spherical harmonic expansion of the Coulomb wave instead. By defining an expression for the Coulomb scattering amplitude that is identical to the previously obtained expressions (2.27) and (2.28), the *Coulomb phase shifts* can be explicitly obtained as [30]

$$\delta_\ell^c(k) = \arg\left[\Gamma(l+1+\mathrm{i}\gamma)\right] \tag{2.69}$$

Unfortunately, these Coulomb phase shifts do *not* go to zero as $\ell \to \infty$ so that the sum of partial scattering amplitudes for the pure Coulomb potential still does not converge. Nevertheless, the main application for Coulomb phase shifts is the treatment of scattering from the *modified Coulomb potential*

$$U_{\overline{c}} = \frac{U_0}{r} + U_s(r) \tag{2.70}$$

which is the sum of a pure Coulomb term and a short range potential $U_s(r)$. In this case it can be shown that the scattering amplitude is given by the coherent sum of the pure Coulomb scattering amplitude, given by (2.64), and a *Coulomb modified* short range scattering amplitude given by

$$f_s(k,\theta) = \sum_{\ell=0}^{\infty}\frac{2\ell+1}{2\mathrm{i}k}\exp[2\mathrm{i}\delta_\ell^c(k)]\left\{\exp[2\mathrm{i}\delta_\ell^s(k)]-1\right\}P_\ell(\cos\theta) \tag{2.71}$$

where $\delta_\ell^s(k)$ are *additional phase shifts* due to the short range potential. The short range potential phase shifts are determined by matching the asymptotic behaviour of the *full* radial wavefunction, which solves the radial equation for (2.70), to the Coulomb radial wavefunction outside the range of the potential $U_s(r)$. The short range potential phase shifts *do* go to zero as $\ell \to \infty$, so that the summation over the partial scattering amplitudes giving f_s does converge.

2.4 Electron-atom collisions

So far, the scattering of a *single* particle by an arbitrary potential has been considered. The electron-atom scattering problem requires finding the stationary states of a $N+1$ electron time-independent Schrödinger equation (see also Sec. 2.2). In order to calculate meaningful continuum quantities care must be taken that the correct asymptotic boundary conditions are applied to the N target electrons *and* to the projectile electron. Furthermore, as opposed to the simple potential scattering problem considered in Sec. 2.3, electron-atom scattering is concerned with a many-body system and in principle requires the *anti-symmetrization* of the wavefunction according to the Pauli principle. Solving such a problem, which includes continuum states, represents a formidable challenge and in practice different strategies have to be devised to obtain approximate solutions. Even with simplifying assumptions, obtaining approximate solutions can nevertheless require sophisticated theoretical and numerical work.

The appropriate choice of strategy enabling the (approximate) solution of the electron-atom scattering problem depends on the energy of the interacting electrons. Section 2.4.1 starts with the treatment of low energy scattering which is defined such that the incoming electron kinetic energy is up to several times the ionization threshold of the target system. In this case the incoming electron can interact strongly with a few of the lowest energy target states and *close coupling expansions* may be used. Based on the basic close coupling equations further simplifications can be introduced, e.g. the static-exchange approximation, such that the basic physical features of the problem are retained while the calculation and modelling effort is reduced. Section 2.4.2 continues with the treatment of high energy scattering where the incoming electron kinetic energy is much higher than the ionization energy of the target electrons. In the high energy domain one can treat the interaction of the incoming electron with the target system as a *perturbation* and use the Born approximation to define and evaluate transition matrix elements for electron scattering from an atomic target. Electron impact ionization is also considered a high energy scattering problem and is also treated in this section using the Born approximation.

2.4.1 Low energy scattering

The derivation of the close coupling equations outlined in the following largely follows the treatments found in Burke [33] and in Bransden and Joachain [29]. The target electrons, with the coordinates $\boldsymbol{r_1}, \ldots, \boldsymbol{r_N}$, are initially assumed to be in some eigenstate of the target atom, while the projectile, with the coordinate $\boldsymbol{r_0}$, is a freely propagating electron with a specific kinetic energy. With this in mind the full $N+1$ electron Hamiltonian is partitioned as follows

$$H = H_t + T_0 + V_{int} \tag{2.72}$$

where H_t is the target Hamiltonian given by

$$H_t = \sum_{p=1}^{N} \left(-\frac{\hbar^2}{2m} \nabla^2_{\boldsymbol{r_p}} - \frac{Z}{r_p} \right) + \frac{1}{2} \sum_{p,q=1}^{N} \frac{1}{r_{pq}} \tag{2.73}$$

T_0 is the kinetic energy operator of the projectile electron

$$T_0 = -\frac{\hbar^2}{2m} \nabla^2_{\boldsymbol{r_0}} \tag{2.74}$$

and V_{int} is the projectile-target interaction potential given by

$$V_{int} = -\frac{Z}{r_0} + \sum_{p=1}^{N} \frac{1}{r_{0p}} \tag{2.75}$$

In the above equations, attractive nuclear potential terms are given by $-Z/r_n$ and it is assumed that the nucleus is infinitely heavy and located at the center of the coordinate system. The repulsive electron-electron interaction terms are given by the $1/r_{mn}$ terms. The *target eigenstates* can be obtained by solving the N electron target Schrödinger equation, using the Hamiltonian (2.73).

The *general* solution of the full Schrödinger equation with the Hamiltonian H given by (2.72) can be obtained using the *close coupling expansion* which states that the eigenfunction ψ can be expressed as a sum of products of target eigenfunctions ϕ_i and corresponding projectile wavefunctions F_i as follows

$$\psi(\boldsymbol{r_N}, \ldots, \boldsymbol{r_0}) = \sum_i \int \phi_i(\boldsymbol{r_N}, \ldots, \boldsymbol{r_1}) F_i(\boldsymbol{r_0}) \tag{2.76}$$

where the sum runs over all discrete and the integral over all continuum eigenstates of the target ϕ_i [33]. By substituting (2.76) into the full Schrödinger equation and projecting onto the target eigenstates ϕ_i one obtains an infinite set of coupled integro-differential equations for the unknown scattered electron wavefunctions F_i given by

$$(\nabla^2_{\boldsymbol{r_0}} + k_i^2) F_i(\boldsymbol{r_0}) = 2 \sum_j \int V_{ij}(\boldsymbol{r_0}) F_j(\boldsymbol{r_0}) \, \mathrm{d}\boldsymbol{r_0} \tag{2.77}$$

where V_{ij} is a potential matrix defined as follows

$$V_{ij}(\boldsymbol{r_0}) = \langle \phi_i(\boldsymbol{r_N}, \ldots, \boldsymbol{r_1}) | \sum_{p=1}^{N} \frac{1}{r_{0p}} - \frac{Z}{r_0} \, | \phi_j(\boldsymbol{r_N}, \ldots, \boldsymbol{r_1}) \rangle \tag{2.78}$$

The value of the momentum k_i in (2.77) follows from energy conservation for each included channel and is given by

$$k_i^2 = 2(E - E_i) \tag{2.79}$$

where E_i is the energy of the target state that is involved, i.e. $E_i = \langle \phi_i | \, H_t \, | \phi_i \rangle$.

Expansion (2.76) is obviously problematic since it includes an infinite number of coupled bound *and* continuum target states. Moreover, since this is a many-body system of electrons, the total electronic wavefunction must satisfy the Pauli exclusion principle, which is not explicitly taken into account in the expansion. Trying to represent *particle exchange* between the incoming electron and one of the target electrons results in a bound state wavefunction for the projectile $\boldsymbol{r_0}$ and a corresponding continuum state for one of the target electrons $\boldsymbol{r_N}, \ldots, \boldsymbol{r_1}$. It turns out that this leads to singularities in the integration over continuum terms in (2.77) [33].

The formal, but impractical, infinite expansion (2.77) can be truncated to a limited number of strongly coupled states. It was also shown that truncating expansion (2.76) to a finite number of *bound* target states enables the generalization of the Hartree-Fock treatment such that it can be applied to wavefunctions

containing continuum states [33]. This leads to the following expression for the full wavefunction

$$\psi(\boldsymbol{r_N},\ldots,\boldsymbol{r_0}) = \mathcal{A}\sum_{i}^{N}\phi_i(\boldsymbol{r_N},\ldots,\boldsymbol{r_1})F_i(\boldsymbol{r_0}) \tag{2.80}$$

where the sum now runs over a finite number of bound target states and the total wavefunction is explicitly anti-symmetrised with the operator $\mathcal{A}$ defined by

$$\mathcal{A} = \frac{1}{\sqrt{N+1}}\left(1 \pm \sum_{\beta=1}^{N} P_{0\beta}\right) \tag{2.81}$$

where $P_{0\beta}$ is a permutation operator exchanging the spatial coordinates of electrons 0 and β. The spatial wavefunction symmetry, which is given by the sign within the operator $\mathcal{A}$, depends on the spin of the two electrons that are exchanged and is chosen such that the total wavefunction, including spin, is anti-symmetric.

The problem of determining which states are *strongly* coupled, and should thus be retained in the truncated expansion (2.80), is quite non-trivial. Also, since the expansion has been truncated to bound states only, it is strictly speaking not possible to represent ionization of one of the bound electrons any longer. Moreover, in some processes, such as long-range polarisation effects, continuum states of the *target* electrons are involved as an intermediate step. In order to partly represent relevant continuum and highly excited states it is possible to introduce square integrable, anti-symmetrised wavefunctions χ_p which are known as *correlation functions*. The expansion now becomes

$$\psi(\boldsymbol{r_N},\ldots,\boldsymbol{r_0}) = \mathcal{A}\sum_{i}\phi_i(\boldsymbol{r_N},\ldots,\boldsymbol{r_1})F_i(\boldsymbol{r_0}) + \sum_{p} c_p\chi_p(\boldsymbol{r_N},\ldots,\boldsymbol{r_0}) \tag{2.82}$$

The correlation functions χ_p can be chosen in such a manner that they diagonalize the full $N+1$ electron Hamiltonian and that they are orthogonal to the space spanned by the first expansion in (2.82) so that

$$\langle\chi_p|\,H\,|\chi_q\rangle = \varepsilon_k\delta_{pq} \tag{2.83}$$

and

$$\langle\chi_p|\phi_i F_i\rangle = 0 \tag{2.84}$$

The first step in obtaining the *close coupling equations* for the approximate expansion (2.82) is to substitute it into the full Schrödinger equation and project onto the square integrable correlation functions χ_p, i.e.

$$\langle\chi_p(\boldsymbol{r_N},\ldots,\boldsymbol{r_0})\,|\,H-E\,|\,\psi(\boldsymbol{r_N},\ldots,\boldsymbol{r_0})\rangle = 0 \tag{2.85}$$

Using the fact that the correlation functions diagonalize the Hamiltonian according to (2.83), and that they are orthogonal to the first term in the expansion, these equations can be used to yield the expansion coefficients c_p giving

$$c_p = \pm\frac{1}{E-\varepsilon_p}\,\langle\chi_p|(H-E)\sum_{\beta=1}^{N}P_{0\beta}|\phi_j(\boldsymbol{r_N},\ldots,\boldsymbol{r_1})F_j(\boldsymbol{r_0})\rangle \tag{2.86}$$

The second step is to substitute expansion (2.82) into the Schrödinger equation and project onto the *target* eigenfunctions, i.e.

$$\langle \phi_i(\boldsymbol{r_N}, \ldots, \boldsymbol{r_1})| \, H - E \, |\psi(\boldsymbol{r_N}, \ldots, \boldsymbol{r_0})\rangle = 0 \tag{2.87}$$

which leads to a set of coupled equations for the unknown projectile functions $F_i(\boldsymbol{r_0})$. These equations are a finite set of integro-differential equations that can be written as follows

$$(\nabla^2_{\boldsymbol{r_0}} \, + \, k_i^2) F_i(\boldsymbol{r_0}) \;\; = \;\; 2 \sum_j \Big\{ V_{ij}(\boldsymbol{r_0}) F_j(\boldsymbol{r_0}) \, + \, W_{ij}(\boldsymbol{r_0}) \, + \, X_{ij}(\boldsymbol{r_0}) \Big\} \tag{2.88}$$

where V_{ij} is the *direct potential* matrix given by (2.78), and W_{ij} and X_{ij} are the *exchange potential* and *correlation potential* matrices respectively. In analogy with the Hartree-Fock treatment, the exchange potential matrix arises due to the anti-symmetrization of the first term in (2.82) and is an explicit representation of the exchange between the projectile and one of the target electrons. It is given by

$$W_{ij}(\boldsymbol{r_0}) = \pm \langle \phi_i(\boldsymbol{r_N}, \ldots, \boldsymbol{r_1})| \left(\frac{1}{r_{0\beta}} + E_i + E_j - E \right) \sum_{\beta=1}^{N} P_{0\beta} \times |\phi_j(\boldsymbol{r_N}, \ldots, \boldsymbol{r_1}) F_j(\boldsymbol{r_0})\rangle \tag{2.89}$$

The inclusion of square integrable, anti-symmetrised wavefunctions χ_k gives rise to a correlation potential that, as mentioned above, represents the short-range effects of electron correlation between the projectile and target electrons. This potential is given by the expression

$$X_{ij}(\boldsymbol{r_0}) = \sum_k c_k \times \langle \phi_i(\boldsymbol{r_N}, \ldots, \boldsymbol{r_1})| \, H - E \, |\chi_k(\boldsymbol{r_N}, \ldots, \boldsymbol{r_0})\rangle \tag{2.90}$$

where c_k are the expansion coefficients obtained previously in (2.86).

Clearly, it is only possible to solve the close coupling equations numerically. Typically this is done by expanding the wavefunctions and potentials in spherical harmonics and applying the partial wave method. Many different numerical packages exist for this task using different degrees of approximation to solve the close coupling equations. The Belfast atomic R-matrix package is a well known example of a rather sophisticated one, which requires elaborate models of the coupled atomic states and the correlation functions as input [34, 33]. Another example is the EPolyScat package, which applies a variational approach based on the Lippman-Schwinger equation in order to solve the close coupling equations. It is specifically designed to treat scattering from a molecular target [35]. Though the mentioned packages are quite powerful and can calculate cross-sections accurately, they are also relatively complicated to use and require a large computational effort.

In the case of elastic scattering the problem may be simplified very much by using the *static-exchange approximation*. This basically means that only a single target state is retained in expansion (2.80) and the set of coupled integro-differential equations (2.88) reduces to the single integro-differential equation

$$(\nabla^2_{\boldsymbol{r_0}} + k_i^2) F_i(\boldsymbol{r_0}) = 2(V_{ii} + W_{ii}) F_i(\boldsymbol{r_0}) \tag{2.91}$$

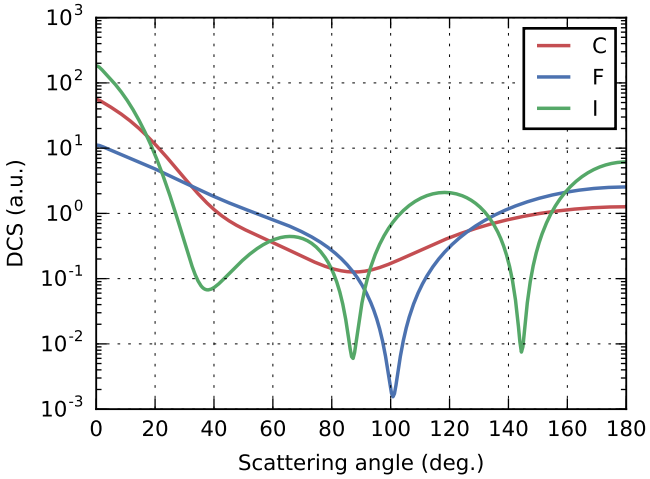

Figure 2.5: Differential cross-sections for elastic scattering from C, F and I atoms at projectile energy $E_i = 50$ eV. Calculated using the software package ELSEPA [36].

The direct potential V_{ii} is simply the static potential corresponding to the sum of the average electron-electron repulsion between the projectile and target electrons and an attractive nuclear term. The static-exchange approximation can clearly *only* represent elastic scattering. Due to the lack of a correlation potential it also does not take into account polarisation of the target atom due to the interaction with the incoming projectile. These shortcomings are in practice often alleviated through the use of approximate semi-empirical potentials, e.g. Buckingham polarization potential. The static-exchange equation is actually still quite computationally intensive due to presence of the non-local exchange potential W_{ii}. A further computational simplification is possible if one uses an approximate potential for the exchange potential as well. Figure 2.5 shows elastic scattering differential cross-sections calculated with the scattering code ELSEPA [36]. This software package uses the static-exchange approximation in combination with approximate exchange and polarization potentials in order to calculate elastic scattering cross-sections for a wide range of atoms.

2.4.2 High energy scattering

The scattering of an electron by an arbitrary scalar potential using a *perturbative expansion*, where the scattering potential is treated as a perturbation, was considered in Sec. 2.3.2. It was shown that a simple and intuitive picture of the resulting Born series is that it represent a *multiple scattering series* where the n^{th} term in the series corresponds to the situation where the projectile interacts n times with the potential before ending up in the final state. The First Born Approximation (FBA) assumes that the projectile interacts a *single time* with the scattering potential and is given by

$$f_{fi}^{B1} = -\frac{1}{4\pi} \langle \psi_f \,|\, V \,|\, \psi_i \rangle \tag{2.92}$$

where $|\psi_i\rangle$ and $|\psi_f\rangle$ are the initial and final states of the projectile, and V is an arbitrary scattering potential. The generalization of this FBA expression to electron-atom scattering can be achieved by considering the following two points. First, from the partitioning of the Hamiltonian given by (2.72) it is clear that the projectile-atom *interaction potential* V_{int}, which is given by (2.75), can be seen as a perturbation. The FBA scattering amplitude (2.92) for electron-*atom* scattering can therefore be obtained by setting $V = V_{int}$. Second, in the case of electron-atom scattering the initial and final states, $|\psi_i\rangle$ and $|\psi_f\rangle$, must be described by a many-body wavefunction, and should be constructed such that they represent the bound atomic states *and* the continuum states for the reaction under consideration. In the case of inelastic scattering the continuum states may consist of more than one electron, which leads to a description of electron impact ionization. This section will show how elastic and inelastic scattering amplitudes for electron-atom scattering can be calculated using the FBA and is mainly based on the treatment by Bransden and Joachain in [29]. It is noted that the scattering reactions considered in this section are assumed to be *highly asymmetric*, i.e. the final state kinetic energy of the projectile is much larger than that of all the other electrons, so that electron exchange effects can be neglected.

Elastic scattering

In order to evaluate the first Born amplitude (2.92) for *elastic* scattering it is necessary to assume a form for the initial and final state wave functions $|\psi_i\rangle$ and $|\psi_f\rangle$. The initial state $|\psi_i\rangle$ can be taken as a product of the target ground state and an incoming plane wave with momentum $\boldsymbol{k_i}$. In the case of elastic scattering from a neutral atom the *asymptotic* form of the scattered electron wave function is a plane wave with momentum $\boldsymbol{k_s}$ which is equal in magnitude to the incoming plane wave momentum, i.e. $k_s = k_i$. In a very first approximation we may thus assume that the final state $|\psi_f\rangle$ is a product of the target in the same atomic ground state and an outgoing plane wave. Using this form for the initial and final states implies that the incoming electron is not influenced by, or has an influence on, the target atom except through an impulse-like interaction with the perturbation potential V_{int}. In other words the initial and final plane waves are not distorted in any way as they get closer to the atom, nor do the target states feel any effect of the incoming electron. This approximation is called the Plane Wave Born Approximation (PWBA). Writing out the PWBA scattering amplitude (2.92) explicitly gives

$$f_{ii}^{PWBA} = -\frac{1}{4\pi}\int \exp(-\mathrm{i}\boldsymbol{k_s}\cdot\boldsymbol{r_0})\phi_i^*(\boldsymbol{r_N},\ldots,\boldsymbol{r_1})\left(-\frac{Z}{r_0}+\sum_{n=1}^{N}\frac{1}{r_{0n}}\right)\times \exp(\mathrm{i}\boldsymbol{k_i}\cdot\boldsymbol{r_0})\phi_i(\boldsymbol{r_N},\ldots,\boldsymbol{r_1})\ \mathrm{d}^{N+1}\boldsymbol{r_{0\ldots N}} \quad (2.93)$$

where ϕ_i is the initial state of the atom.

Before continuing with calculations using the PWBA approximation it is interesting to compare (2.93) to the close coupling equations introduced in the previous section. Using (2.78), which defines the direct potential matrix in the close coupling equations, (2.93) can be rewritten as

$$f_{ii}^{PWBA} = -\frac{1}{4\pi}\int \exp(\mathrm{i}\boldsymbol{q}\cdot\boldsymbol{r_0})V_{ii}(\boldsymbol{r_0})\,\mathrm{d}\boldsymbol{r_0} \quad (2.94)$$

where $\boldsymbol{q} = \boldsymbol{k_i} - \boldsymbol{k_s}$ is the *momentum transfer* vector. Thus in the PWBA, the first Born scattering amplitude is given by the Fourier transform of the *static potential* between the incoming electron and all the target electrons, plus the attractive term of the nucleus. Comparing to (2.88) it is again made clear that this approximation does not include exchange effects or any short-range electron correlation effects.

Returning to (2.93) and performing the integration over projectile coordinate $\boldsymbol{r_0}$ using the Bethe integral (2.67) leads to the following general expression for the atomic scattering amplitude

$$f_{ii}^{PWBA}(q) = \frac{Z - D_i(\boldsymbol{q})}{q^2} \tag{2.95}$$

This expression contains two contributions: one Coulombic term Z/q^2 which takes scattering from the nucleus only into account and the term $D_i(\boldsymbol{q})/q^2$ which is the electron charge scattering factor[7] $D_i(\boldsymbol{q})$ is given by

$$D_i(\boldsymbol{q}) = \int \rho_i(\boldsymbol{r}) \exp(\mathrm{i}\boldsymbol{q} \cdot \boldsymbol{r}) \, \mathrm{d}\boldsymbol{r} \tag{2.96}$$

In this expression $\rho_i(\boldsymbol{r}) = |\psi_i|^2$ is the electron charge density. For the case of an isolated atom the electron charge distribution $\rho_i(\boldsymbol{r})$ is spherically symmetric so that (2.96) becomes

$$D_i(q) = \int_r r^2 \rho_i(r) \frac{\sin(qr)}{qr} \, \mathrm{d}r \tag{2.97}$$

Using these relations it is straightforward to calculate PWBA atomic scattering amplitudes for any atom once its wavefunction, or an approximation, is known. In practice the charge scattering factors, i.e. $D_i(\boldsymbol{q})$, can be retrieved using reference tables such as [38, 39].

It is instructive to evaluate (2.93) for the two simple cases of hydrogen and helium. The hydrogen 1s state is known exactly and is given by

$$\phi_{H,1s} = \frac{1}{\sqrt{\pi}} \exp(-r_1) \tag{2.98}$$

where $\boldsymbol{r_1}$ is the bound electron position coordinate. For the helium atom an approximate wavefunction given by

$$\phi_{He,1s} = \frac{Z_e^3}{\pi} \exp[-Z_e(r_1 + r_2)] \tag{2.99}$$

with $Z_e = 1.69$ is used. Substituting (2.99) into(2.93) and performing the integration over the bound electron coordinates $\boldsymbol{r_1}$ and $\boldsymbol{r_2}$ leads to an expression of the form (2.94) with the potential V_{ii} given by

$$V_{1s,1s}(r_0) = -nZ_e \left(1 + \frac{1}{Z_e \, r_0}\right) \exp(-2Z_e \, r_0) \tag{2.100}$$

[7] A perturbative approach to calculating elastic *X-ray* scattering by atoms results in the expression $f_{ii}(q) = D_i(\boldsymbol{q})/q^2$ where $D_i(\boldsymbol{q})$ is the same as in (2.95) [37]. X-rays are almost exclusively scattered by the electron charge distribution, which reacts much more readily to the electro-magnetic field, so that the nuclear scattering factor becomes negligible.

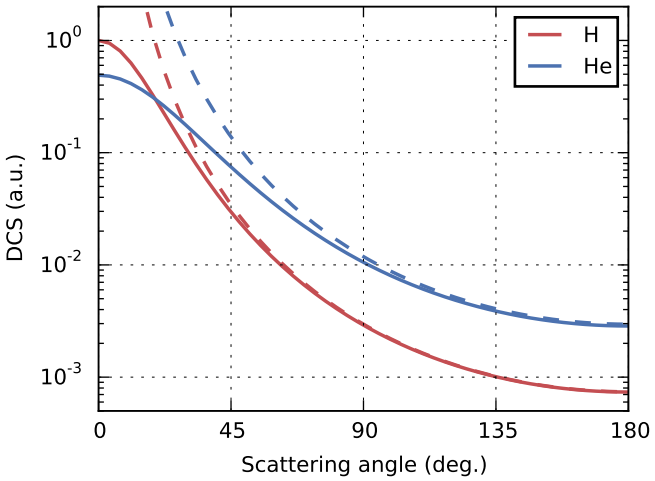

Figure 2.6: Elastic differential scattering cross-section (DCS) in the Plane Wave Born Approximation for hydrogen and helium (full lines) for a scattered electron energy of $E_i = 250$ eV. The scattering cross-sections for scattering from the bare nuclear charge of hydrogen and helium, i.e. $Z = 1$ and $Z = 2$, are shown as well (dashed lines).

where $n = 2$. The potential V_{ii} for scattering from hydrogen is given by the same expression, but with $n = 1$ and $Z_e = 1$ [29]. The scattering amplitude is obtained by performing the final integration over the projectile position coordinate $\boldsymbol{r_0}$ which results in the Fourier transform of $V_{1s,1s}$ in the momentum transfer variable $\boldsymbol{q}$ giving

$$f_{1s,1s}^{PWBA} = 2n\frac{q^2 + 8Z_e^2}{(q^2 + 4Z_e^2)^2} \tag{2.101}$$

The total elastic cross-sections, given by the absolute square of the scattering amplitude (2.101), for the hydrogen and helium atom are plotted in Fig. 2.6. Using the Bethe integral, it is also possible to calculate the cross-section for electron scattering from the *nucleus only* which is plotted with dashed lines.

It is interesting to observe that the scattering cross-section for hydrogen is more concentrated around small scattering angles compared to that of helium. This is a direct consequence of the fact that the helium wavefunction is more tightly bound, i.e. more sharply defined in position, and thus has a broader *momentum-space* representation. A simple physical picture is that in the PWBA the difference in the momentum between incoming and outgoing scattered electron, i.e. momentum transfer $\boldsymbol{q}$, is provided by the initial momentum of the *target* electron. The scattering amplitude is therefore given by the probability of the target electron having the required momentum. This is directly obtained from (2.94), which gives the scattering amplitude as the magnitude of the momentum-space representation of the potential V_{ii} for a given momentum transfer $\boldsymbol{q}$. As may be inferred from the above discussion it is a general feature of high energy electron-atom scattering that the cross-section tends to be wider for heavier atoms because they have more tightly bound electrons,

and thus higher target electron momenta available for scattering.

Finally, Fig. 2.6 also shows that as the scattering angle increases, the cross-section starts resembling more and more that of pure electron-nucleus scattering (dashed lines). This can again be explained with a simple physical picture that for a large momentum transfer the projectile has interacted rather strongly with the target and thus starts seeing the unscreened nucleus. For small momentum transfer values, the interaction is rather weak and the electron is mainly sees the exponential tail of the static potential (2.100). Because the exponential tail falls off faster than $1/r$, the static potential is a *short range* potential (see Sec. 2.2) and the total cross-section remains finite for $q = 0$. This can be contrasted to the cross-section for scattering from a Coulomb potential, e.g. pure electron-nucleus scattering in Fig. 2.6 (dashed line), which diverges for $q \to 0$ (see also Sec. 2.3.3).

Inelastic scattering and ionization

The general high energy electron-atom *ionization* problem requires the treatment of a three-body continuum system, consisting of the incoming and the ejected electron, and the residual ion, for which there is no analytical solution. In principle, the solution cannot *a priori* be obtained in a perturbative way since, depending on the scattering conditions, there can be a strong interaction over an extended range between any of the two fragments through the Coulomb potential. For example, the two outgoing electrons may have an outgoing energy and direction that are very similar, e.g. in a symmetric (e,2e) reaction, and will interact in a very extended region [40]. However, depending on the initial and final conditions one can use simplifying assumptions which enable the calculation of the differential cross-section for the specific process. The main focus of this work are *asymmetric reactions* where the incoming electron is very fast compared to the ejected electron. In this case one can ignore the long-range Coulomb potentials acting on the projectile and treat the collision perturbatively. In a first approximation the residual ionic potential acting on the ejected electron may also be neglected, which leads to the Plane Wave Born Approximation (PWBA) for impact ionization that is treated in the first part of this section. Following this it will be shown that it is also possible to take the ionic Coulomb potential acting on the ejected electron into account using the Distorted Wave Born Approximation (DWBA). At the end of this section, the PWBA and DWBA will be applied to calculate differential cross-sections for electron impact ionization of the hydrogen atom. This will give some basic insight into the different contributions that make up the cross-section and enable an interpretation of it in terms of reaction kinematics.

Before moving on to the main discussion, which is electron impact ionization, inelastic electron scattering resulting in target *excitation* shall be considered. Writing down the PWBA scattering amplitude for inelastic electron scattering which to (2.93) is relatively straightforward. The main difference here is that the initial and final state of the *target* are not the same any longer. Therefore, assuming that the target states are orthogonal to each other, the projectile-nucleus term Z/r_0 in the perturbation potential does not contribute to the scattering amplitude. Also, since the outgoing electron loses a part of its energy

to the target electron, the final outgoing electron momentum is now given by

$$k_s^2 = k_i^2 + 2E_{ij} \tag{2.102}$$

where E_{ij} is the energy difference between the initial and final target state. Using these conditions, the PWBA amplitude for inelastic scattering is given as follows

$$f_{ij}^{PWBA} = -\frac{1}{4\pi}\int \exp(\mathrm{i}\boldsymbol{q}\cdot\boldsymbol{r_0})\phi_j^*(\boldsymbol{r_N},\ldots,\boldsymbol{r_1})\left(\sum_{n=1}^{N}\frac{1}{r_{0n}}\right)\times \\ \phi_i(\boldsymbol{r_N},\ldots,\boldsymbol{r_1})\ \mathrm{d}^{N+1}\boldsymbol{r_{0\ldots N}} \tag{2.103}$$

where $\boldsymbol{q} = \boldsymbol{k_i} - \boldsymbol{k_s}$. Using the Bethe integral (2.67) to evaluate the integration over $\boldsymbol{r_0}$ this expression can be rewritten as follows

$$f_{ij}^{PWBA} = -\frac{2}{q^2}\sum_{n=1}^{N}\langle\phi_j|\exp(\mathrm{i}\boldsymbol{q}\cdot\boldsymbol{r_n}\,|\phi_i\rangle \tag{2.104}$$

This expression shows a remarkable similarity to the transition matrix elements describing the interaction of atoms with an electro-magnetic field in a standard perturbative treatment [29]. In the limit $q \to 0$, the dipole approximation may be applied to the operator in (2.104) so that the transition can even be linked directly to the *optical oscillator strength*. In the early years of research on electron collisions this was especially interesting as it provided a convenient method to investigate the optical properties of atoms and molecules at high energies [41].

The PWBA may also be applied in the context of electron impact ionization and is widely used in the field of (e,2e)-spectroscopy [42]. In this case plane waves are used for the single incoming and the two outgoing electrons, and the final target state φ_e is an ionic (ground) state. Within this approach the influence of the ionic Coulomb field on both of the outgoing electrons, as well as the Coulomb interaction between the two ejected electrons, is neglected. This of course implies that the relative velocity between all three fragments is large. Again writing out (2.93) for the case of electron impact ionization leads to

$$f_{ie}^{PWBA} = -\frac{1}{4\pi}\int \exp(\mathrm{i}\boldsymbol{q}\cdot\boldsymbol{r_0})\exp(-\mathrm{i}\boldsymbol{k_e}\cdot\boldsymbol{r_N})\varphi_e^*(\boldsymbol{r_{N-1}},\ldots,\boldsymbol{r_1})\times \\ \left(-\frac{Z}{r_0}+\sum_{n=1}^{N}\frac{1}{r_{0n}}\right)\phi_i(\boldsymbol{r_N},\ldots,\boldsymbol{r_1})\ \mathrm{d}^{N+1}\boldsymbol{r_{0\ldots N}} \tag{2.105}$$

where $\boldsymbol{k_e}$ is the momentum of the ejected electron which is obtained from energy conservation which is given by

$$k_s^2 = k_i^2 - k_e^2 + 2E_{ie} \tag{2.106}$$

Integral (2.105) consists of two terms: a *projectile-nucleus* and a *projectile-electron* interaction term. In contrast to the case of electron impact excitation, the initial and final target states are *not* orthogonal, as one of the bound electrons is promoted to the continuum, so that the projectile-nucleus term must

be retained. The projectile-nucleus term represents an indirect interaction term which leads to the ejection of electron $\boldsymbol{r_N}$ *via* the interaction of the projectile with the nucleus. Using the Bethe integral to effect integration over the projectile coordinate $\boldsymbol{r_0}$, the projectile-nucleus term may be rewritten as follows

$$\kappa_{ie}^{PWBA} = Z\frac{2}{q^2}\int \exp(-\mathrm{i}\boldsymbol{k_e}\cdot\boldsymbol{r_N})\Phi_{ei}(\boldsymbol{r_N})\ \mathrm{d}\boldsymbol{r_N} \tag{2.107}$$

where

$$\Phi_{ei}(\boldsymbol{r_N}) = \int \varphi_e^*(\boldsymbol{r_{N-1}},\ldots,\boldsymbol{r_1})\phi_i(\boldsymbol{r_N},\ldots,\boldsymbol{r_1})\ \mathrm{d}^{N-1}\boldsymbol{r_{1\ldots N-1}} \tag{2.108}$$

is the spatial overlap integral between the initial and final (ionic) target state, i.e. the Dyson orbital. The projectile-nucleus scattering amplitude (2.107) is thus given by the Fourier component, or equivalently the momentum-space value, of the Dyson orbital (2.108) at the momentum $\boldsymbol{k_e}$. The projectile-electron term represents the interaction with *one* of the target electrons $\boldsymbol{r_1},\ldots,\boldsymbol{r_N}$ leading to ejection of electron $\boldsymbol{r_N}$ and therefore includes direct *and* indirect interactions. Proceeding in a similar fashion as with the projectile-nucleus term, the projectile-electron term can be written as

$$\eta_{ie}^{PWBA} = -\frac{2}{q^2}\Bigg\{\int \exp(\mathrm{i}\boldsymbol{\Delta}\cdot\boldsymbol{r_N})\Phi_{ei}(\boldsymbol{r_N})\ \mathrm{d}\boldsymbol{r_N} + \sum_{n=1}^{N-1}\int \exp(-\mathrm{i}\boldsymbol{k_e}\cdot\boldsymbol{r_N})\Upsilon_{ei}(\boldsymbol{r_N})\ \mathrm{d}\boldsymbol{r_N}\Bigg\} \tag{2.109}$$

where $\boldsymbol{\Delta} = \boldsymbol{q} - \boldsymbol{k_e} = \boldsymbol{k_i} - \boldsymbol{k_s} - \boldsymbol{k_e}$ and

$$\Upsilon_{ei}(\boldsymbol{r_N}) = \int \exp(\mathrm{i}\boldsymbol{q}\cdot\boldsymbol{r_n})\varphi_e^*(\boldsymbol{r_{N-1}},\ldots,\boldsymbol{r_1})\phi_i(\boldsymbol{r_N},\ldots,\boldsymbol{r_1})\ \mathrm{d}^{N-1}\boldsymbol{r_{1\ldots N-1}} \tag{2.110}$$

Comparing (2.109) to (2.107) it is first seen that the *sign* of the projectile-electron scattering amplitude contributions is opposite to that of the projectile-nucleus term. The first term in (2.109) is a direct interaction term which represents *binary scattering* between the incoming projectile and the *ejected* electron. This integral may be interpreted in the same way as (2.107) as being given by the momentum-space value of the Dyson orbital (2.108), but now at the momentum value $\boldsymbol{\Delta}$ instead of $\boldsymbol{k_e}$. The remaining terms under the summation in (2.109) represent *indirect* projectile-electron interactions, in which the projectile interacts with a target electron $\boldsymbol{r_n}$ that is *not* ejected but acts as an intermediary instead and transfers the energy to the ejected electron $\boldsymbol{r_N}$. Comparing these indirect terms to (2.107), which gives the *indirect* projectile-nucleus scattering contribution, it is seen that they are again given by the Fourier transform of a function at the momentum value $\boldsymbol{k_e}$. However, unlike in (2.107), this function is *not* the Dyson orbital any longer. The function $\Upsilon(\boldsymbol{r_N})$ differs from the Dyson orbital (2.108) in the fact that the integration over $\boldsymbol{r_n}$ now includes a complex exponential term. This can be interpreted as giving the *momentum-space* value of the $\boldsymbol{r_n}$ electron orbital at the momentum given by $\boldsymbol{q}$.

In order to demonstrate basic features of the theory in a relatively simple setting, the PWBA scattering amplitude for electron impact ionization of the

hydrogen atom will be considered. The initial target wavefunction is given by $\phi_{1s}(r_1) = \sqrt{Z^3/\pi}\exp(-Zr_1)$, where $Z = 1$. As there is by definition only a single target electron, the Dyson orbital is identical to the initial target wavefunction. The total scattering amplitude is the sum of the nuclear and electron scattering amplitudes given by (2.107) and (2.109) which leads to the following expression after the substitution of $\phi_{1s}(r_1)$

$$f_{H,1s}^{PWBA} = \frac{2}{q^2}\frac{1}{\sqrt{\pi}}\left\{\int \exp(-\mathrm{i}\boldsymbol{k_e}\cdot\boldsymbol{r_1})\exp(-r_1)\ \mathrm{d}\boldsymbol{r_1} - \int \exp(\mathrm{i}\boldsymbol{\Delta}\cdot\boldsymbol{r_1})\exp(-r_1)\ \mathrm{d}\boldsymbol{r_1}\right\} \quad (2.111)$$

The two integrals in (2.111) are given by the momentum-space representation of the target wavefunction $\phi_{1s}(r_1)$, evaluated at the momentum value $\boldsymbol{k_e}$ and $\boldsymbol{\Delta}$ respectively. Momentum-space representations of hydrogenic wave functions have been obtained in analytical form by Podolsky and Pauling [43]. For the 1s hydrogenic orbital it is given by

$$\phi_{1s}(p) = \frac{2^{3/2}}{\pi Z^{3/2}}\frac{1}{[(p/Z)^2+1]^2} \quad (2.112)$$

where p is the momentum magnitude. The scattering amplitude integrals can now be evaluated analytically and are found to be given by

$$f_{H,1s}^{PWBA} = \frac{2}{q^2}\frac{2^{3/2}}{\pi}\left[\frac{1}{(k_e^2+1)^2} - \frac{1}{(\Delta^2+1)^2}\right] \quad (2.113)$$

Figure 2.7 shows the Triply Differential Cross-Section (TDCS) for electron impact ionization of hydrogen calculated using (2.113) and (2.13) for the projectile energy $E_i = 500$ eV, scattering angle $\theta_s = 8°$ and ejected electron energy $E_e = 10$ eV. The first observation that can be made from this plot is that the projectile-nucleus term is independent of the ejected electron angle, while the projectile-electron term peaks at a certain ejection angle giving rise to the so-called *binary peak*. The behaviour of these contributions can be most easily understood by considering the scattering amplitude expression (2.113) together with the kinematics of the reaction using the graphical representation shown in Fig. 2.8. From this graphical representation it is indeed obvious that the projectile-electron interaction term should peak at some ejection angle θ_e which minimizes the magnitude of $\boldsymbol{\Delta}$, and that the projectile-nucleus contribution should be constant. Using basic trigonometry the binary peak angle can be explicitly calculated as

$$\theta_{bin} = -\arctan\left(\frac{k_s\sin\theta_s}{k_i - k_s\cos\theta_s}\right) \quad (2.114)$$

An understanding of the kinematic conditions at which the magnitude of $\boldsymbol{\Delta}$ is minimized, and the corresponding location of the binary peak, can be very useful for obtaining qualitative insight into the shape of the ejected electron spectrum, see e.g. Sec. 2.5.2 or Sec. 4.3. The second observation that is made with respect to Fig. 2.7 is that the interference between the two terms in (2.113), which is due to the opposite *sign* of the two contributions, leads to a minimum

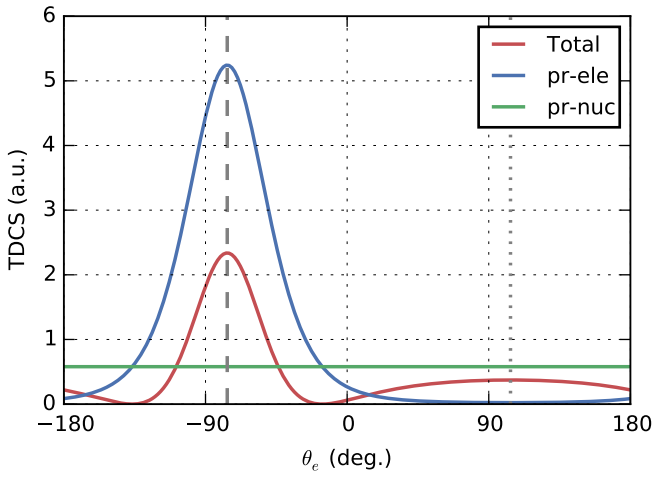

Figure 2.7: Electron impact ionization Triply Differential Cross-Section (TDCS) in the PWBA for atomic hydrogen. The projectile energy $E_i = 500$ eV, scattering angle $\theta_s = 8°$ and ejected electron energy $E_e = 10$ eV. The total cross-section (red) is plotted together with the partial cross-sections for projectile-electron (blue) and projectile-nucleus (green) scattering only. The *binary peak* location can be calculated using (2.114) and is at $\theta_e = -76°$ (dashed gray), while the *recoil peak* is in the exact opposite direction at $\theta_e = 103°$ (dotted gray).

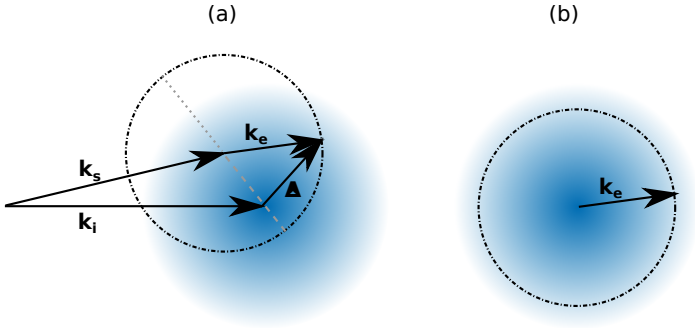

Figure 2.8: Graphical representation of the hydrogen scattering amplitude (2.113) where (a) is the projectile-electron and (b) the projectile-nucleus scattering contribution. The possible values that the momentum variables $\mathbf{\Delta}$ in (a) and $\boldsymbol{k_e}$ in (b) can take as a function of the ejection angle θ_e are shown by the dash-dotted line. The scattering amplitude for each contribution is a function of the momentum-space Dyson orbital which is illustrated by the blue gradient. Contribution (a) peaks at the minimum magnitude of $\mathbf{\Delta}$ (dashed gray line) whereas contribution (b) is constant with respect to θ_e.

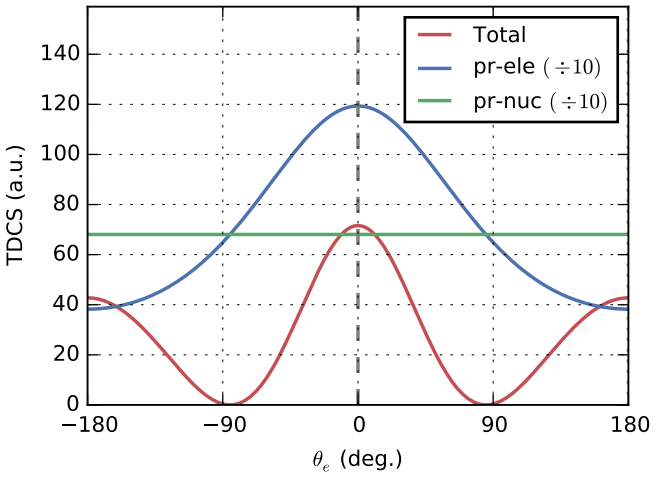

Figure 2.9: Same as Fig. 2.7 but for scattering angle $\theta_s = 0°$. The partial cross-sections for projectile-electron (green) and projectile-nucleus (red) scattering are divided by 10 for visibility.

in the cross-section and the appearance of a local maximum in the opposite direction to the binary peak. This is the so-called *recoil peak*. From the previous discussion of kinematics it can be inferred that the relative contribution of the projectile-nucleus term should become more important for small k_e and/or for small projectile scattering angle θ_s, i.e. small $\boldsymbol{q}$. This is illustrated in Fig. 2.9 where all the scattering parameters are equal except for the scattering angle θ_s, which is set to zero. The recoil peak is indeed seen to be much stronger relative to the binary peak which is now located at $\theta_e = 0°$. The emission pattern is actually starting to resemble a p-wave. This is consistent with the 'dipole like' interaction regime at small momentum transfers mentioned in the inelastic scattering treatment at the beginning of this section. Comparing the absolute values of the cross-section it is also seen that they are much larger than in Fig. 2.7 which is due to the q^{-2} dependence of the scattering amplitude on the momentum transfer $\boldsymbol{q} = \boldsymbol{k_i} - \boldsymbol{k_s}$.

In section 2.3.2 it was shown that the PWBA is just the first term in a Born series and that improving the calculation accuracy would in principle require taking further series terms into account, i.e. Second Born Approximation. Another powerful approach is to use a 'distorted' form for the initial and final wavefunctions which are an exact solution to some part of the perturbation potential, e.g. the Coulomb potential of the core. This gives rise to the Distorted Wave Born Approximation (DWBA) which is still a first-order perturbation approach, but which improves the accuracy of the calculation by adapting the wavefunction to the perturbation potential. The distorted initial and final wavefunctions can for example be computed using the partial wave method as continuum solutions to the *static potentials* given by the initial and final state of the target atom respectively [44].

The DWBA is conveniently illustrated by treating electron impact ionization of the hydrogen atom by a relatively fast projectile. Considering the asymmet-

ric reaction where the ejected electron is slow compared to the projectile it is expected that the parent ion Coulomb field has an important influence on the *ejected electron*. A logical step would therefore be to use a Coulomb wavefunction, introduced in Sec. 2.3.3, for the slow ejected electron instead of the plane wave assumed in the PWBA. The DWBA scattering amplitude for electron impact ionization of hydrogen can therefore be written as

$$f_{H,1s}^{DWIA} = -\frac{1}{4\pi}\int \exp(\mathrm{i}\boldsymbol{q}\cdot\boldsymbol{r_0})\psi_c^*(\boldsymbol{r_1})\frac{1}{r_{01}}\phi_{1s}(\boldsymbol{r_1})\,\mathrm{d}\boldsymbol{r_0}\,\mathrm{d}\boldsymbol{r_1} \tag{2.115}$$

where $\psi_c(\boldsymbol{r_1})$ is the Coulomb wavefunction given by (2.62). Comparing this expression to the PWBA scattering amplitude (2.105) it is seen that the $1/r_0$ interaction potential is eliminated from the DWBA integral due to the orthogonality of the Coulomb wave and the bound hydrogen state. This is a specific example of a general feature of the DWBA approach, which eliminates a part of the perturbation potential from the first-order Born term by adapting the continuum electron wavefunctions to the problem at hand. The next step is to use the Bethe integral to effect integration over the projectile coordinate $\boldsymbol{r_0}$ which leads to the following expression

$$f_{H,1s}^{DWIA} = \frac{2}{q^2}(2\pi)^{-3/2}\pi^{-2}\exp[\pi Z/(2k)]\Gamma(1-\mathrm{i}Z/k)\times \int \exp(\mathrm{i}\boldsymbol{\Delta}\cdot\boldsymbol{r_0})\,{}_1\mathrm{F}_1[\mathrm{i}Z/k,1,\mathrm{i}(k_e r_1+\boldsymbol{k_e}\cdot\boldsymbol{r_1})]\,\phi_{1s}(\boldsymbol{r_1})\,\mathrm{d}\boldsymbol{r_1} \tag{2.116}$$

This expression can be evaluated analytically for the 1s hydrogenic wavefunction and the scattering amplitude is finally given by [29]

$$f_{H,1s}^{DWBA} = \frac{4\sqrt{2}}{\pi}\exp[\pi/(2k_e)]\Gamma(1-\mathrm{i}/k_e)\exp[-\mathrm{i}/k_e\log v(\boldsymbol{\Delta},\boldsymbol{k_e})]\times \frac{\boldsymbol{q}[\boldsymbol{q}-\boldsymbol{k_e}(\mathbf{1}+\mathbf{i}/\boldsymbol{k_e})]}{[q^2-(k_e+\mathrm{i})^2][(\boldsymbol{q}-\boldsymbol{k_e})^2+1]^2} \tag{2.117}$$

where $v(\boldsymbol{\Delta},\boldsymbol{k_e})$ is given by

$$v(\boldsymbol{\Delta},\boldsymbol{k_e}) = \frac{q^2-k_e^2+1-2\mathrm{i}k_e}{(\boldsymbol{q}-\boldsymbol{k_e})^2+1} \tag{2.118}$$

The PWBA and DWBA calculations for electron impact ionization of the hydrogen atom are shown together in Fig. 2.10 for two projectile scattering angles. Comparing the two approximations in Fig. 2.10(a) it can be seen that the main features are comparable in the sense that both the calculations display the binary and recoil peaks. However, the PWBA calculation clearly overestimates the total magnitude of the cross-section and the relative strength of the recoil peak. This is attributed to the lack of screening of the nucleus by the electron charge, because the PWBA considers the cross-section as given by a coherent sum of scattering from the *bare* nucleus and from the electron charge distribution separately. For larger scattering angles of the incoming projectile, shown in Fig. 2.10(b), the projectile-nucleus contribution dominates the total PWBA cross-section so that the binary peak has almost disappeared while the recoil peak is very strong. On the other hand, in the DWBA this behaviour is absent

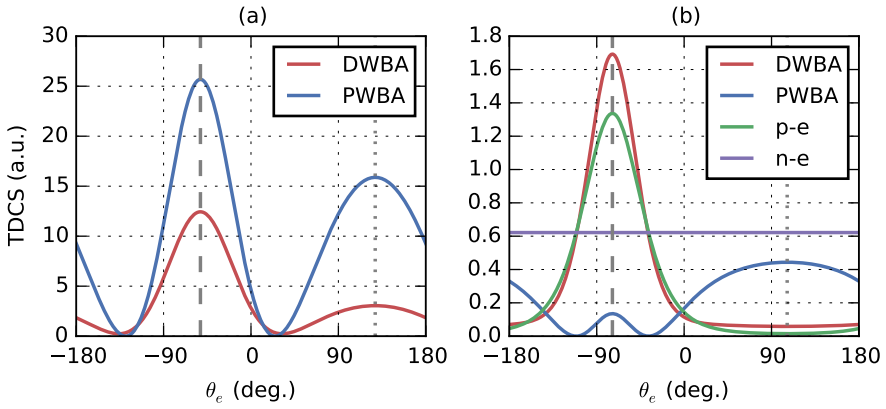

Figure 2.10: Comparison of the electron impact ionization Triple Differential Cross-Section (TDCS) in the PWBA (blue) and DWBA (red) for the hydrogen atom. The projectile scattering angles are (a) $\theta_s = 3°$ and (b) $\theta_s = 13°$. In (b) the partial PWBA scattering amplitudes for the projectile-electron (green) and projectile-nucleus (purple) contribution are also plotted. The projectile and ejected electron energies are $E_i = 250$ eV and $E_e = 5$ eV.

and on comparing the DWBA cross-section to the PWBA partial contributions from projectile-electron (green line) and projectile-nucleus (purple line) interaction terms it is concluded that the DWBA curve can largely be attributed to the projectile-electron interaction term from the PWBA.

2.5 Electron-molecule collisions

The general theoretical tools introduced in the treatment of electron-atom collisions, are of course, also applicable to the treatment of electron-molecule collisions. In practice the treatment of electron-molecule collisions brings with it its own complexities. One major difference in the treatment of the electron-molecule problem is the inherent multi-center nature of the molecule, which defines its structure and is also the property of interest in the study of structural dynamics. Many powerful Quantum Chemistry packages exist which can solve for the molecular nuclear and electronic structure providing molecular properties such as the electronic charge distribution. Such a target molecule description may be used directly to calculate scattering amplitudes and cross-sections with software packages such as EPolyScat [35]. However, this approach can require a large amount of computing power and does not give a very direct physical insight into the relation between the molecular structure and the experimentally observed quantities.

This section will concentrate on the Independent Atom Model (IAM) of electron-molecule scattering, which gives a very direct and intuitive relation between the molecular structure and the differential cross-section. The IAM is an approximation that treats molecular scattering by assuming that each atom within the molecule scatters the projectile independently so that the total scat-

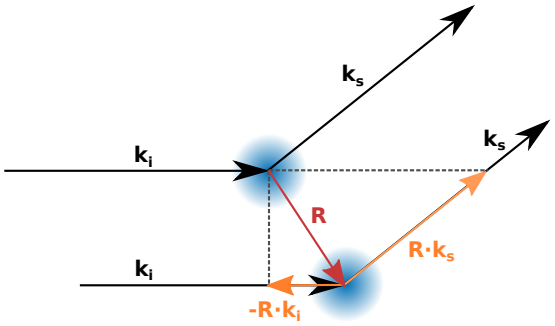

Figure 2.11: Graphical representation of the Independent Atom Model (IAM) for elastic electron scattering. The electron with incident momentum $\boldsymbol{k_i}$ is elastically scattered by two independent atomic centres (blue) which results in a path length difference (yellow) that is given by the scalar product between the inter-atomic displacement vector and the momentum transfer, i.e. $\boldsymbol{R} \cdot \boldsymbol{q} = \boldsymbol{R} \cdot (\boldsymbol{k_s} - \boldsymbol{k_i})$.

tering amplitude is a coherent sum of the atomic scattering amplitudes. Section 2.5.1 treats the IAM in case of elastic scattering and shows how diffraction arises from the molecular structure. Section 2.5.2 will introduce a simple theoretical treatment of the effects of the molecular structure on the *impact ionized electron* and will show how this is related to the IAM in elastic scattering. In both sections, the effects of averaging over the molecular frame on the experimentally observable cross-sections will also be discussed.

Before continuing it is worth mentioning an important limitation of the IAM. In the case of bound atoms the assumption that the atomic charge distribution remains identical to the free atom distribution is obviously not true. The perturbation is not very large for core electrons, which are not influenced much by chemical bonding, but for higher-lying orbitals the influence may be especially significant. In traditional X-ray and electron diffraction this limitation is not very severe, because typically high energy projectiles are used which penetrate deeper into the molecule and map out the core potential [45, 37].

2.5.1 Independent Atom Model of diffraction

The Independent Atom Model (IAM) is an electron diffraction model used traditionally to describe high-energy X-ray and electron diffraction due to *elastic* scattering from a molecular target [45, 37]. The IAM scattering amplitude for a molecule is obtained as a coherent superposition of the scattered wave contributions from each *independent atom* within the molecule. Elastic electron scattering from atoms was treated in Sec. 2.4.2 where it was shown that in the Plane Wave Born Approximation (PWBA) the scattering amplitude is given by the integral (2.93). The scattering amplitude from a single displaced atomic centre can be derived from this expression by a change of coordinates so that the scattering centre is located at a point $-\boldsymbol{R}$. Applying the coordinate trans-

formation $\boldsymbol{r_n} \mapsto \boldsymbol{r_n} + \boldsymbol{R}$ to (2.93) the integral is modified to

$$f_{ii,+\boldsymbol{R}}^{PWBA} = -\frac{1}{2\pi}\int \exp[-\mathrm{i}\boldsymbol{k_s}\cdot(\boldsymbol{r_0}+\boldsymbol{R})]\phi_i^*(\boldsymbol{r_N},\ldots,\boldsymbol{r_1})\left(-\frac{Z}{r_0}+\sum_{n=1}^{N}\frac{1}{r_{0n}}\right)\times \exp[\mathrm{i}\boldsymbol{k_i}\cdot(\boldsymbol{r_0}+\boldsymbol{R})]\phi_i(\boldsymbol{r_N},\ldots,\boldsymbol{r_1})\ \mathrm{d}^{N+1}\boldsymbol{r_{0\ldots N}} \quad (2.119)$$

In rewriting this expression use was made of the fact that the perturbation potential and the bound state wavefunction ϕ_i only depend on the *relative position* of the atomic core with respect to the integration coordinates. These terms in the integrand are therefore invariant with respect to the change of coordinates. The exponential plane wave terms, on the other hand, acquire an *additional phase* term. This phase shift can be taken out of the integral so that the scattering amplitude in the displaced coordinate system can simply be written as

$$f_{ii,+\boldsymbol{R}}^{PWBA} = \exp(\mathrm{i}\boldsymbol{q}\cdot\boldsymbol{R}) \times f_{ii}^{PWBA} \quad (2.120)$$

where $\boldsymbol{q} = \boldsymbol{k_i} - \boldsymbol{k_s}$. This result is also illustrated graphically in Fig. 2.11, from which it is seen that the phase factor can in fact be interpreted as a *path length difference*. Generalizing this result to a multi-atomic molecule consisting of N atomic scattering centres located at positions $\boldsymbol{R_n}$ leads to the following expression for the total scattering amplitude

$$f^{IAM} = \sum_{n=1}^{N} f_n \exp(\mathrm{i}\boldsymbol{q}\cdot\boldsymbol{R}_n) \quad (2.121)$$

where f_n are individual atomic scattering amplitudes which can be calculated using any of the techniques described in Sec. 2.4. Substituting (2.121) in (2.12) from Sec. 2.2 gives the total Differential Cross-Section (DCS) for electron molecule scattering in the IAM as

$$\frac{\mathrm{d}\sigma^{IAM}}{dk\ \mathrm{d}\Omega_s} = \sum_{n=1}^{N}|f_n|^2 + 2\sum_{n=1}^{N}\sum_{m=n+1}^{N}\mathrm{Re}\left\{f_n f_m^* \exp(\mathrm{i}\boldsymbol{q}\cdot\boldsymbol{R}_{nm})\right\} \quad (2.122)$$

where $\boldsymbol{R}_{nm} = \boldsymbol{R_n} - \boldsymbol{R_m}$. The first factor in this expression is simply the sum of the differential cross-sections for scattering from each of the constituent atomic centres within the molecule independently. This factor does not depend on the structure of the molecule and is inherent to the atoms only. The second term in this expression is the *structural interference* term, which arises from the coherent addition of the scattering amplitudes from all pairs of atomic scattering centres within the molecule.

The general DCS expression (2.122) assumes a particularly simple form in the case of a homo-nuclear diatomic molecule which is given by

$$\frac{\mathrm{d}\sigma_{A2}^{IAM}}{dk\ \mathrm{d}\Omega_s} = |f(q)|^2[2 + 2\cos(\boldsymbol{q}\cdot\boldsymbol{R})] \quad (2.123)$$

where $\boldsymbol{R}$ is the position coordinate of the second atom relative to the first one, and $|f(q)|^2$ is the atomic cross-section. The first term in (2.123) is twice the atomic cross-section while the second term is a two-centre interference factor

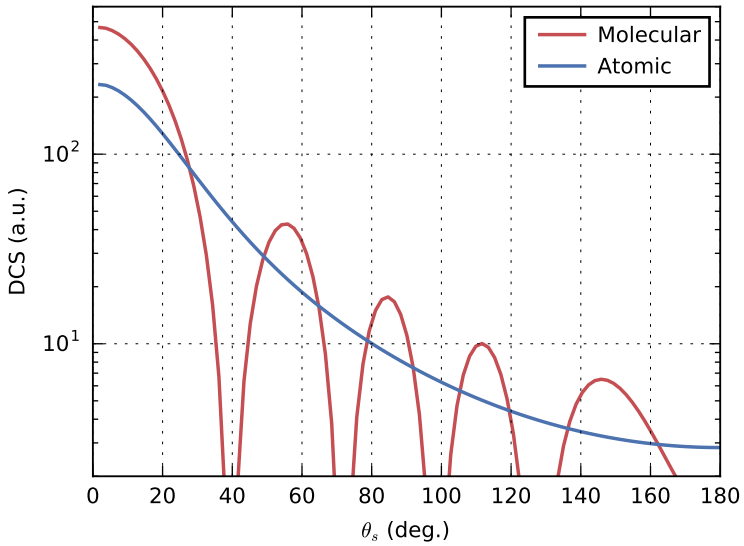

Figure 2.12: Differential cross-section of I_2 (red) within the Independent Atom Model (IAM) and of the two independent Iodine atoms only (blue), i.e. first term in (2.123). Atomic cross-sections were calculated using reference data from [38, 39] with a projectile energy of $E_i = 100$ eV. The inter-nuclear vector $\boldsymbol{R}$ is parallel to the projectile momentum $\boldsymbol{k_i}$, and has a magnitude of 2.67 Å.

with an oscillation period depending on the inter-nuclear distance. The calculated (DCS) for the homo-nuclear diatomic molecule I_2 using the IAM is shown in Fig. 2.12. The atomic term is calculated using reference data from [38, 39] and is monotonously decreasing over the whole range of scattering angle θ_s (blue line). The total DCS (red line) on the other hand shows pronounced oscillations which result from the cosine term in (2.123).

The DCS calculated using (2.122) assumes that the molecule is completely fixed in space with the atomic positions given by $\boldsymbol{R_n}$. For gas-phase targets, but also for unordered solid state targets, this is obviously not the case and (2.122) must be suitably averaged to obtain experimental DCS expressions. It is therefore expected that the structural interference oscillations that are so pronounced in Fig. 2.12 will wash out to a certain degree. It turns out that molecular interference oscillations are not washed out completely in the DCS even for *randomly oriented*, i.e. unaligned, molecules. In order to see this (2.122) is integrated over all the molecular frame angles in polar coordinates. The first term in (2.122) does not depend on the atomic positions $\boldsymbol{R_{nm}}$ and can thus be taken out of the integral. The terms in the summation do depend on molecular orientation and the integration over molecular frame angles gives for each term the expression

$$\sigma_{nm} = \frac{1}{4\pi} \int_\phi \int_\theta f_n(q) f_m^*(q) \exp(\mathrm{i}\boldsymbol{q} \cdot \boldsymbol{R}_{nm}) \sin\theta \, \mathrm{d}\phi \, \mathrm{d}\theta \tag{2.124}$$

where the integration is performed over the molecular polar and azimuthal angle coordinates θ and ϕ with respect to an appropriately chosen reference frame.

For *unaligned molecules* one can take the direction of $\boldsymbol{q}$ as the reference axis to which the integration variables refer and this can be done for *each* atomic pair term $\boldsymbol{R}_{nm}$ separately. This crucial observation allows one to write the dot product in the exponential as $\boldsymbol{q}\cdot\boldsymbol{R}_{nm} = qR_{nm}\cos\theta$ where θ is the angle between the momentum transfer vector and the atomic distance vector $\boldsymbol{R_{nm}}$. Equation (2.124) now simplifies to

$$\sigma_{nm} = f_n(q)f_m^*(q)\frac{1}{4\pi}\int_\phi \mathrm{d}\phi \int_\theta \exp(\mathrm{i}qR_{nm}\cos\theta)\sin\theta\,\mathrm{d}\theta \tag{2.125}$$

which can be integrated using the variable substitution $x = \mathrm{i}qR_{jk}\cos\theta$, leading to the final expression

$$\begin{aligned}\sigma_{nm} &= f_n(q)f_m^*(q)\frac{1}{2}\left(\frac{-1}{\mathrm{i}qR_{nm}}\right)\int_{\mathrm{i}qR_{nm}}^{-\mathrm{i}qR_{nm}} \exp(x)\,\mathrm{d}x \\ &= f_n(q)f_m^*(q)\frac{sin(qR_{nm})}{qR_{nm}}\end{aligned} \tag{2.126}$$

The total cross-section for randomly oriented molecules is therefore given by

$$\frac{\mathrm{d}\sigma_U^{IAM}}{dk\ \mathrm{d}\Omega_s} = \sum_{n=1}^{N}|f_n(q)|^2 + 2\sum_{n=1}^{N}\sum_{m=n+1}^{N}\mathrm{Re}\left\{f_n(q)f_m^*(q)\right\}\frac{sin(qR_{nm})}{qR_{nm}} \tag{2.127}$$

The second term in this expression shows that for randomly oriented molecules there are residual oscillatory terms which have an oscillation period that depends on the distances between all the atomic pairs R_{nm} within the molecule. For the homo-nuclear diatomic molecule this expression reduces to

$$\frac{\mathrm{d}\sigma_{U,2A}^{IAM}}{dk\ \mathrm{d}\Omega_s} = |f(q)|^2\left[2 + 2\frac{sin(qR)}{qR}\right] \tag{2.128}$$

Figure 2.13 shows the calculated DCS for unaligned I_2 (red line). Compared to the perfectly aligned molecule calculation plotted in 2.12 it is clear that the molecular interference is much less pronounced, but that it is nevertheless still there.

Traditional gas-phase diffraction experiments were necessarily performed on unaligned molecules, but the recent development of new techniques capable of partially aligning gas-phase molecules has enabled a new class of diffraction experiments [24, 22]. Intuitively one would expect that the partially aligned molecule DCS is somewhere between the two extremes of perfectly aligned molecules (2.122) and unaligned molecules (2.127). Unfortunately, for *partially aligned* molecules it is not possible to obtain a simple analytical expression for the DCS such as the one for unaligned molecules (2.127) any longer. A part of the difficulty is that the momentum transfer vector *can not* be taken as the arbitrary reference axis any longer because the integration over the molecular angular coordinates is referenced to the *alignment axis*. The relative orientation between $\boldsymbol{q}$, the alignment axis, and the inter-atomic vector $\boldsymbol{R_{nm}}$ must now explicitly be taken into account when expanding the dot product $\boldsymbol{q}\cdot\boldsymbol{R}_{nm}$, giving rise to much more complex expressions. Nevertheless, these integrals can be evaluated numerically with relative ease and the effect of partial alignment I_2

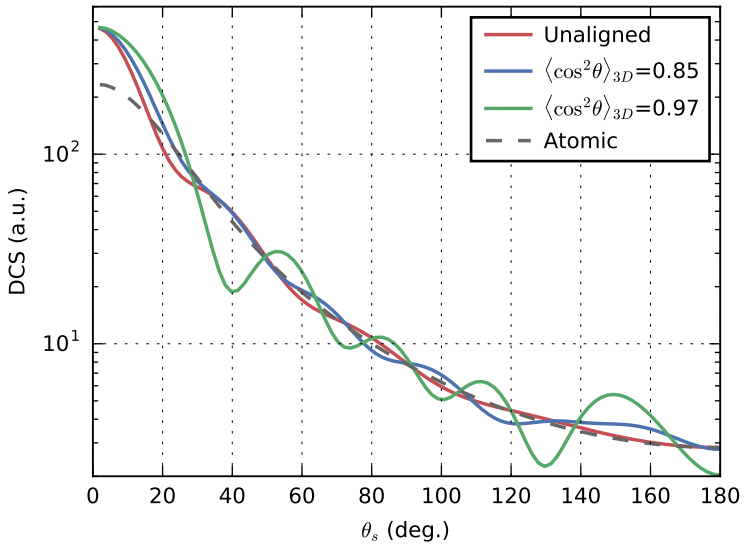

Figure 2.13: Differential cross-section for I_2 under the same conditions as in 2.12, but for unaligned (red) and partially aligned (blue and green) molecules.

on its elastic scattering DCS is shown in Fig. 2.13 (green and blue lines). For a relatively low degree of alignment of $\langle\cos^2\theta\rangle_{3D} = 0.85$ (blue line) the difference from the unaligned molecular DCS is, as expected, quite small. For a larger degree of alignment $\langle\cos^2\theta\rangle_{3D} = 0.97$ (green line) the molecular oscillations become much stronger and the nodes that are visible in the perfectly aligned case in Fig. 2.12 are starting to form.

A powerful way of visualising the influence of the molecular frame on the DCS is to look at the contrast between the DCS for aligned and unaligned molecules. The molecular oscillations in the case of unaligned molecules (red line) and for low degrees of alignment (green line) in Fig. 2.13 approach the atomic DCS (grey dashed line) very quickly for increasing scattering angle, i.e. momentum transfer. In experiments this small difference of the molecular DCS from the atomic case can quickly be drowned out by noise sources. Moreover, the extraction of the molecular oscillatory factor from the DCS requires knowing very precisely the atomic DCS factors. Manipulating the molecular frame, through partial alignment of the molecules, offers the extremely useful advantage of being able to extract the molecular factor from the DCS is a very direct way. One way to do this is by calculating the *normalized difference* between two experimental DCS curves as follows

$$\delta_{norm} = \frac{\sigma_A - \sigma_U}{\sigma_A + \sigma_U} \tag{2.129}$$

where σ_A is the partially aligned molecular DCS and σ_U some reference DCS, e.g. for unaligned molecules. Figure 2.14 shows the normalized difference between the DCS for unaligned I_2 and the two partially aligned cases shown in Fig. 2.13. Figure 2.14 shows that the enhanced oscillations caused by the change in molecular frame distribution are indeed brought out very cleanly through the

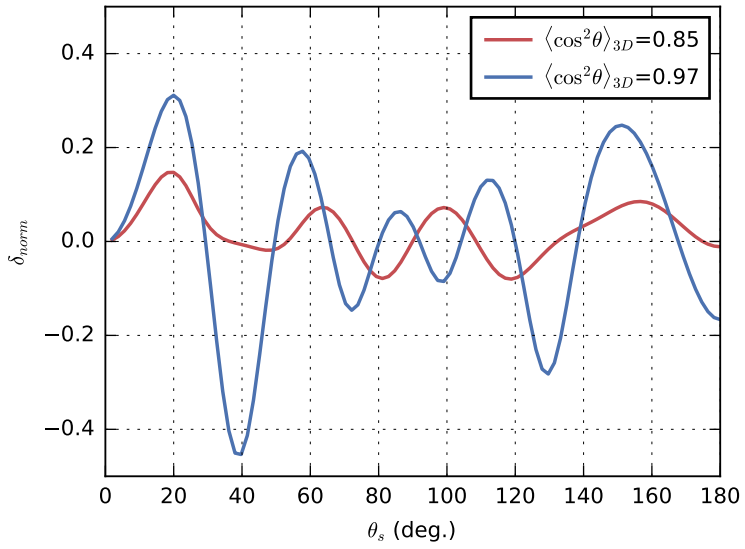

Figure 2.14: Normalized difference (2.129) between the differential cross-sections for elastic electron scattering from partially aligned and unaligned I_2 molecules shown in Fig. 2.13.

normalized difference. In experimental settings, the normalized difference can typically be acquired easily by simply delaying or switching off the means of alignment. This has the major advantage that all other experimental conditions are unaltered so that systematic sources of error can be minimized effectively.

2.5.2 Molecular effects in electron impact ionization

Secondary electrons produced by electron impact ionization may carry information on the *molecular structure* through different physical mechanisms, as illustrated in Fig. 2.15. Impact Ionized Coherent Electron Emission (IICEE) leads to the interference between electrons emitted from two distinct atomic centres within a molecule, which depends on the relative position of the two emitters. It is a generalization of the well-known Cohen-Fano interference effect, which is due to coherent *photoelectron* emission from molecules, to the case where the ionized electron is produced by charged particle impact [46, 4]. IICEE has been demonstrated in a number of experiments using heavy ions [47, 48, 49] as well as electrons [50, 51, 52] as projectiles. A second mechanism that can give rise to molecular interference effects is Impact Ionized Secondary Electron Diffraction (IISED). An impact ionized electron that is ejected from one of the atomic centres within the molecule can scatter elastically from *another* atomic center, which leads to interferences between the scattered and *non*-scattered electrons. IISED can be seen as a generalization of the photoelectron diffraction effect, see e.g. [21]. Though there are some experimental observations that may be attributed to IISED effects [48, 49], a conclusive demonstration of the effect has not yet been provided [53, 4]. The theoretical description of IISED, or other higher-order scattering effects, is very limited and one of the first theo-

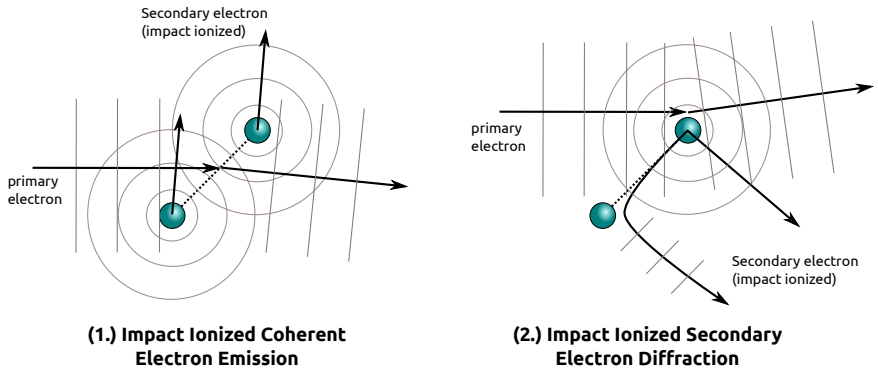

Figure 2.15: Schematic illustration of two processes that may give rise to molecular interference effects in the spectrum of impact ionized electrons. Impact Ionized Coherent Electron Emission (IICEE) leads to interferences between secondary electrons emitted from two distinct atomic centres within the molecule. Impact Ionized Secondary Electron Diffraction (IISED) arises when a secondary electron produced at one atomic centre is scattered by another atomic centre within the same molecule.

retical publications specifically dealing with this problem was only published in 2016 by Agueny *et al.* [54]. From both the theoretical treatments and the experimental data published so far it is clear that the IISED effect is relatively weak compared to IICEE interference effects[8]. The theory in this section will focus on the treatment of the more established and experimentally more accessible IICEE mechanism.

Theoretical treatments on the topic of IICEE are relatively sparse and tend to focus on the fundamental case of H_2. The molecular electron impact ionization of H_2 and H_2^+ was treated theoretically in a series of papers by Rivarola, Joulakian *et al.* [55, 56, 57, 58]. In these papers the first Born amplitude for electron impact ionization of H_2 and H_2^+ is evaluated using special forms of the ejected and scattered electron wavefunctions based on the Briggs, Brauner and Klar (BBK) treatment of a three-body Coulomb system [59]. The BBK theory uses products of Coulomb waves to describe the final continuum wavefunctions in order to take long range interactions of the outgoing particles into account and can thus be classified as a type of Distorted Wave Born Approximation (DWBA) treated in Sec. 2.4.2. In the last paper in the series by Stia *et al.* [58] the treatment of electron impact ionization H_2 is finally distilled into a treatment of structural diffraction effects and its signature in the Triple Differential

[8] In the case where the IICEE effects are suppressed, such as in electron impact ionization of N_2 where contributions from multiple orbitals tend to cancel IICEE effects, it can happen that IISED effects become more dominant [49].

Cross-Section (TDCS)[9]. The TDCS is given by Stia et.al. as

$$\frac{\mathrm{d}\sigma_M}{\mathrm{d}k_e\,\mathrm{d}\Omega_e\,\mathrm{d}\Omega_s} = \sigma_A\big[2+2\cos(\boldsymbol{\Delta}\cdot\boldsymbol{R})\big] \tag{2.130}$$

where σ_A is the *atomic* hydrogen TDCS, $\boldsymbol{\Delta} = \boldsymbol{k_i} - \boldsymbol{k_s} - \boldsymbol{k_e}$ is a momentum variable depending on the incoming, scattered and ejected electron momentum and $\boldsymbol{R}$ is the molecular axis vector. This expression is very similar to the traditional expression for elastic scattering from homo-nuclear molecules in the IAM given by (2.123). In both cases there are two terms in the equation, the first of which describes independent scattering from the atomic centres, and the second, the *interference* between the outgoing waves originating from the two centres.

Using the same reasoning as in the previous section it will now be shown that the expression for H_2 derived by Stia *et al.* is a generalization of the IAM expression for elastic scattering from a homo-nuclear diatomic molecule for the case of *electron impact ionization.* Following the approach to deriving the IAM for elastic scattering outlined in the previous section, the coordinate transformation $\boldsymbol{r_n} \mapsto \boldsymbol{r_n} + \boldsymbol{R}$ is applied to the PWBA for electron impact ionization given by (2.105). This results in

$$f_{ie,+\boldsymbol{R}}^{PWBA} = -\frac{1}{2\pi}\int \exp\big[\mathrm{i}\boldsymbol{q}\cdot(\boldsymbol{r_0}+\boldsymbol{R})\big]\exp\big[-\mathrm{i}\boldsymbol{k_e}\cdot(\boldsymbol{r_N}+\boldsymbol{R})\big]\times$$
$$\varphi_e^*(\boldsymbol{r_{N-1}},\ldots,\boldsymbol{r_1})\left(-\frac{Z}{r_0}+\sum_{n=1}^{N}\frac{1}{r_{0n}}\right)\phi_i(\boldsymbol{r_N},\ldots,\boldsymbol{r_1})\;\mathrm{d}^{N+1}\boldsymbol{r_{0\ldots N}} \tag{2.131}$$

where again use was made of the fact that the perturbation potential and the bound state wavefunctions ϕ_i and φ_e only depend on the *relative position* of the atomic core with respect to the integration coordinates and are therefore invariant with respect to the change of coordinates. Taking the phase shift in the plane wave factors resulting from the coordinate displacement out of the integral, the scattering amplitude can be written as

$$f_{ie,+\boldsymbol{R}}^{PWBA} = \exp(\mathrm{i}\boldsymbol{\Delta}\cdot\boldsymbol{R})\times f_{ie}^{PWBA} \tag{2.132}$$

which is analogous to (2.120) for the case of elastic scattering. Generalizing this to the multi-atomic molecule one obtains the IAM cross-section for electron impact ionization as follows

$$\frac{\mathrm{d}\sigma^{IAM}}{dk_e\,\mathrm{d}\Omega_e\,\mathrm{d}\Omega_s} = \sum_{n=1}^{N}|f_n|^2 + \;2\sum_{n=1}^{N}\sum_{m=n+1}^{N}\mathrm{Re}\left\{f_n f_m^*\exp(\mathrm{i}\boldsymbol{\Delta}\cdot\boldsymbol{R}_{nm})\right\} \tag{2.133}$$

where f_n are the individual atomic scattering amplitudes, which are in general a function of the *three* momenta $\boldsymbol{k_i}$, $\boldsymbol{k_e}$ and $\boldsymbol{k_s}$ and can be calculated using the techniques outlined in Sec. 2.4.2. Applying (2.133) to the case of a homo-nuclear diatomic molecule one readily retrieves (2.130) which was derived by Stia et.al. for the case of H_2 [58].

[9]Here it is assumed that $\boldsymbol{k_i}$ and the atomic position vectors $\boldsymbol{R_n}$ are *parameters.* The magnitude of the scattered electron momentum is fixed through energy conservation constraints. The remaining three degrees of freedom are the magnitude and direction of the ejected electron k_e and Ω_e and the direction of the scattered electron Ω_s.

Though the IAM expressions derived for electron impact ionization of molecules and those for elastic scattering are quite similar, there are important differences that need to be borne in mind. The momentum variable $\boldsymbol{\Delta}$ appearing in the molecular *structure* terms in (2.133) is a function of all *three* continuum electron momentum vectors. The structural terms, which depend on the kinematics of the reaction, are therefore more complex as compared to elastic scattering where $\boldsymbol{k_e} \equiv 0$ and $\boldsymbol{\Delta}$ reduces to the momentum transfer variable $\boldsymbol{q} = \boldsymbol{k_i} - \boldsymbol{k_s} = 2k\sin(\theta_s/2)$. Besides the structural interference terms, the *atomic* terms f_n are also triply differential and depend on the *ejected* as well as the *scattered* electron momenta, as was shown in Sec. 2.4.2. This means that in evaluating (2.133) to obtain experimentally accessible information these extra degrees of freedom must be properly taken into account through suitable averaging. In principle the information contained in (2.130) can only be completely accessed through an experiment that can determine all three momentum vectors $\boldsymbol{k_i}$, $\boldsymbol{k_s}$, $\boldsymbol{k_e}$ *and* the molecular frame vectors $\boldsymbol{R_n}$ simultaneously.

To get an impression of the effect of averaging on the molecular electron impact ionization TDCS, molecular frame *orientation* averaging will be considered and compared to the case of elastic electron scattering. In their publication Stia et.al. also provide an expression for the TDCS of randomly oriented H_2 [58]

$$\frac{\mathrm{d}\sigma_M}{\mathrm{d}k_e\,\mathrm{d}\Omega_e\,\mathrm{d}\Omega_s} = \sigma_A\left[2 + 2\frac{\sin(\Delta R)}{\Delta R}\right] \tag{2.134}$$

This expression can easily be derived following the same approach as in the previous section on elastic electron scattering from unaligned molecules. Again the total cross-section is a sum of an atomic term that describes scattering from the two independent atoms and an oscillatory term due to the residual two-center interference effect. However, this term is now a function of the momentum variable $\boldsymbol{\Delta}$ which has some important implications. Figure 2.16 shows a plot of the two-centre interference factor $2\sin(\Delta R)/(\Delta R)$ from (2.134) as a function of the ejected electron angle θ_e for several values of the *scattered electron* angle θ_s. The reaction is constrained to be coplanar, meaning that the incoming, scattered and ejected electron are in one plane. From this plot it becomes clear that the interference factor behaves quite differently from the elastic case treated in the previous section. The $\theta_s = 4^\circ$ curve resembles the elastic case the most as there is a strong peak in the interference term followed by oscillations which decrease in magnitude rapidly. The strong peak is due to the fact that $\Delta = 0$ at a specific ejection angle so that the $2\sin(\Delta R)/(\Delta R)$ term reaches its maximum value of two. This can also be understood by considering the kinematics of this case as illustrated in Fig. 2.17. From this figure it is also inferred that there is always a specific scattered electron angle for which the ejected electron wavevector with a fixed magnitude will reach $\Delta = 0$. The position of the peak can also be calculated using kinematics and is the same as that for the binary peak discussed in 2.4.2 given by (2.114). The case of $\theta_s = 4^\circ$ is unique in the sense that the momentum variable Δ goes through zero. For other scattered electron angles, the momentum variable Δ will have a specific range of values with a *non-zero* minimum that depends on the specific kinematics of that situation. Especially interesting is the fact that the apparent oscillation frequency of the curves in Fig. 2.16 also varies with the *scattered electron* angle, and does not depend on the inter-atomic distance R only. For $\theta_s = 0^\circ$ the oscillation has a very long period compared to the other curves,

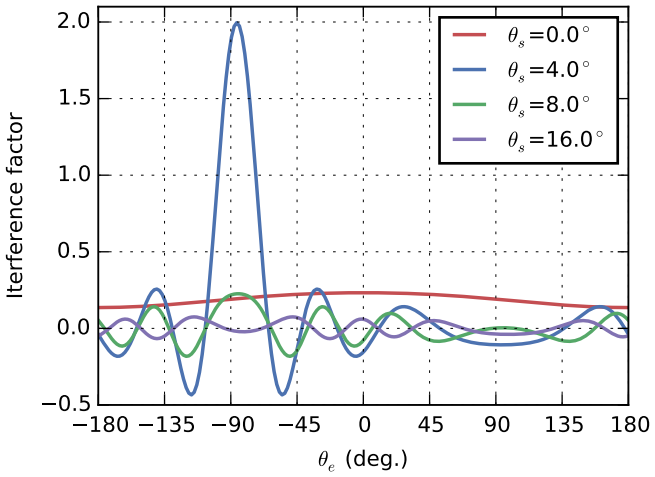

Figure 2.16: Plot of the structural interference factor $2\sin(\Delta R)/(\Delta R)$ from (2.134), where $\Delta = |\boldsymbol{k_i} - \boldsymbol{k_s} - \boldsymbol{k_e}|$, as a function of the ejected electron angle for four different scattered electron angles θ_s. The projectile energy $E_i = 100$ keV, the ejected electron energy $E_e = 500$ eV and the inter-nuclear distance $R_{H_2} = 0.74$ Å.

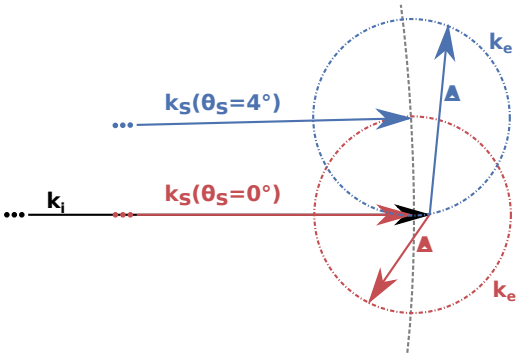

Figure 2.17: Illustration of kinematics for $\theta_s = 0°$ (red) and 4° (blue) shown in Fig. 2.16. Dashed-dotted circles indicate the possible values that the sum of $\boldsymbol{k_s}$ and $\boldsymbol{k_e}$ can take in the two cases. $\boldsymbol{\Delta} = \boldsymbol{k_i} - (\boldsymbol{k_s} + \boldsymbol{k_e})$ is given by the difference between points on the dashed-dotted circles and $\boldsymbol{k_i}$, as indicated by the two example vectors.

which is because the magnitude of $\mathbf{\Delta}$ is barely changing. This situation is also illustrated in Fig. 2.17.

From the above discussion it is clear that any further averaging of the unaligned electron impact ionization TDCS (2.134) with respect to the other degrees of freedom, such as the scattered electron angle, will have very strong influence on the visibility of the molecular structure in the experimental spectra. For example, in experiments which use a Velocity Map Imaging Spectrometer to detect the ejected electron one must average over all the scattered electron angles. This topic will be treated in more detail in Chapter 4.

2.6 Strong field ionization and electron scattering

One of the main topics of this thesis is Laser Induced Electron Diffraction (LIED). This is a new and promising technique for the realization of the long-standing goal of *imaging* structural dynamics in molecules at femtosecond time scales and with Ångström spatial resolution [60, 3]. Fig. 2.18 illustrates the three-step model of LIED where the laser field-induced tunnelling ionization of a molecule is followed by subsequent acceleration and *re-scattering* of the photoelectron under the influence of the strong laser field. The photoelectrons that scatter elastically can be used to construct ultrafast diffraction images of the parent molecule. This section will introduce some of the basic concepts of strong field theory and show how photoelectron scattering and LIED can be treated within the framework of the *semi-classical* three-step model [61, 62]. The semi-classical model described in this section gives an intuitive and insightful picture of strong field physics and is used in Chapter 3 for the analysis of LIED experiments on aligned molecules.

One of the earliest and most influential theoretical works on the ionization of atoms by an intense, low-frequency laser field was that of Keldysh in 1965 [63]. The Strong Field Approximation (SFA) introduced by Keldysh describes the ionization process in a *strong* laser field using, somewhat paradoxically, *perturbation theory*. This can be qualitatively understood in the following way.

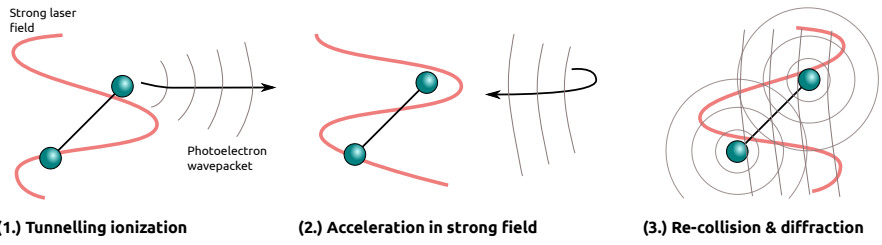

Figure 2.18: Three-step model of Laser Induced Electron Diffraction (LIED). After tunnelling ionization by the strong laser field (1), the photoelectron is accelerated by the oscillating electric field (2) and is finally driven back to the molecule where it scatters elastically (3). The multi-center nature of the molecule, i.e. molecular structure, leads to diffraction features in the final photoelectron spectrum.

The initial electronic state is strongly bound and localized around the atom so that the *laser field* can be treated as a perturbation. However, once the photoelectron has reached the continuum the laser field dominates its behaviour and the *atomic potential* can be seen as a perturbation. The process of dividing the full Hamiltonian into a dominant reference term and a small perturbative term is well-known from conventional perturbation theory and is called *Hamiltonian partitioning*, see e.g. [30, 26, 28]. The SFA, as initially developed by Keldysh, completely neglects the influence of the parent ion on the photoelectron once it is in the continuum, and can be seen as a solution to first order in perturbation theory. Keldysh's SFA is therefore not able to explain effects in which re-scattering plays a crucial role. Improved versions of the theory, i.e. SFA2, were introduced to effectively include further perturbation terms and account for re-scattering effects [64, 65]. The success of the SFA has culminated in Intense-field Many-body S-matrix Theory (IMST) that *formalizes* the process of Hamiltonian partitioning, which was implicit in the work of Keldysh, and provides a consistent and powerful formulation of strong field theory [66]. The interested reader is referred to Appendix A for a summary of the IMST, or to the excellent textbook by Joachain *et al.* [28], for a more in-depth discussion of strong field theory.

The SFA admits a very insightful and useful semi-classical interpretation, which was pointed out in the seminal work by Corkum [61]. Using the saddle-point approximation, it can be shown that the SFA perturbation integrals, which arise from a Quantum Mechanical treatment of strong-field ionization, can be interpreted in terms of the *classical* motion of the photoelectron in the laser field [67]. The semi-classical model proposed by Corkum makes use of this interpretation, treating the photoelectron motion in the continuum classically, and is particularly useful in modelling the effects arising from photoelectron re-scattering. The Quantitative Re-scattering Theory (QRT), which was proposed by C.D. Lin *et al.* [62], is based on the semi-classical model and is specifically developed to enable the extraction of (field-free) electron *scattering cross-sections* from the photoelectron spectrum of a strong-field ionized target. The QRT has been successfully used to interpret experimental results in some of the first works demonstrating the LIED technique [68, 69]. The rest of this section will be devoted to developing the semi-classical three-step model, which includes re-scattering effects, and applying the QRT procedure to extract electron scattering Differential Cross-Sections (DCS) from the photoelectron spectrum of a strong-field ionized molecule.

The first step in the semi-classical model is tunnelling ionization. Tunnelling ionization of an atom in a static electric field is a standard problem in Quantum Mechanics and is usually treated using the Wentzel-Kramers-Brillouin (WKB) approximation, see e.g. [29, 30]. Tunnelling in a low-frequency laser field can be seen as quasi-static, so that the adiabatic approximation can be applied to obtain a tunnelling rate that is a function of the instantaneous value of the oscillating electric field [70, 28]. The Ammosov-Delone-Krainov (ADK) adiabatic tunnelling ionization rate for an atom in a strong laser field is given by

$$\Gamma_{ADK}(t) \propto \frac{\kappa^2}{2}\left(\frac{3|\boldsymbol{\mathcal{E}}(t)|}{\pi\kappa^3}\right)^{1/2}\left(\frac{2\kappa^3}{|\boldsymbol{\mathcal{E}}(t)|}\right)^{2n^*-|m|-1}\exp\left[-\frac{2}{3}\frac{\kappa^3}{|\boldsymbol{\mathcal{E}}(t)|}\right] \tag{2.135}$$

In this equation $\kappa = (2I_p)^{1/2}$, where I_p is the ionization potential of the atom, and $\boldsymbol{\mathcal{E}}(t)$ is the electric field vector. The ADK expression was derived using quantum defect atomic orbitals as a description of the initial state of the tunnelling electron [71, 28]. A quantum defect orbital is an approximate description of the valence orbital of a multi-electron atom that is obtained by using an effective central-field potential to model the effect of the inner-shell electrons on the valence electron. In (2.135) the parameter $n^* = Z_c/\kappa$ is an effective principal quantum number, where Z_c is the effective charge parameter of the approximate quantum defect central field potential, and m is the magnetic quantum number of the quantum defect orbital. The ADK expression gives the ionization rate for photoelectrons with zero momentum after tunnelling. More general tunnelling rate expressions can be derived, which show that the probability of ionization with a non-zero momentum is exponentially suppressed [29]. The ADK theory of tunnelling ionization of an atom can be extended to molecular systems [72, 73]. The ionization rate of a *molecule* depends explicitly on the molecular orbital orientation with respect to the laser field.

In the second step of the semi-classical model, the photoelectron is treated as a classical particle that is driven exclusively by the electric field of the laser. From classical electrodynamics it is known that the momentum of an electron in an electric field at any instant in time, i.e. *kinetic momentum*, is given by [28, 67]

$$\boldsymbol{\pi}(t) = \boldsymbol{p} + \boldsymbol{A}(t) \tag{2.136}$$

where $\boldsymbol{A}(t)$ is the *vector potential*, which is in the dipole approximation given by

$$\boldsymbol{A}(t) = -\int^t \boldsymbol{\mathcal{E}}(\tau)\,\mathrm{d}\tau \tag{2.137}$$

The vector $\boldsymbol{p}$ in (2.136) is the *canonical momentum*, which is a *constant* of the motion and can be determined from the initial conditions. As mentioned above, from adiabatic tunnelling theory it follows that the ionization rate is largest for photoelectrons that have a momentum of zero at the time of ionization, i.e. $\boldsymbol{\pi}(t_0) = 0$. For these photoelectrons the canonical momentum is given by

$$\boldsymbol{p} = -\boldsymbol{A}(t_0) \tag{2.138}$$

If the vector potential returns to zero[10] as the laser field is switched off, it follows from (2.136) that the *final* momentum of the photoelectron is equal to the canonical momentum and that its kinetic energy is given by $E_f = \frac{1}{2}|\boldsymbol{A}(t_0)|^2$. For an electric field given by

$$\mathcal{E}(t) = \mathcal{E}_0 \cos\omega t \tag{2.139}$$

the vector potential (2.137) is given by

$$A(t) = -A_0 \sin\omega t \tag{2.140}$$

where $A_0 = \mathcal{E}_0/\omega$ is the vector potential amplitude. The maximum final kinetic energy that a photoelectron with an initial kinetic momentum of zero can attain in such a field is therefore

$$E_f^{max} = \frac{1}{2}A_0^2 \tag{2.141}$$

[10]This is true for a laser pulse duration which is long with respect to the period of the laser field and is switched on and off adiabatically.

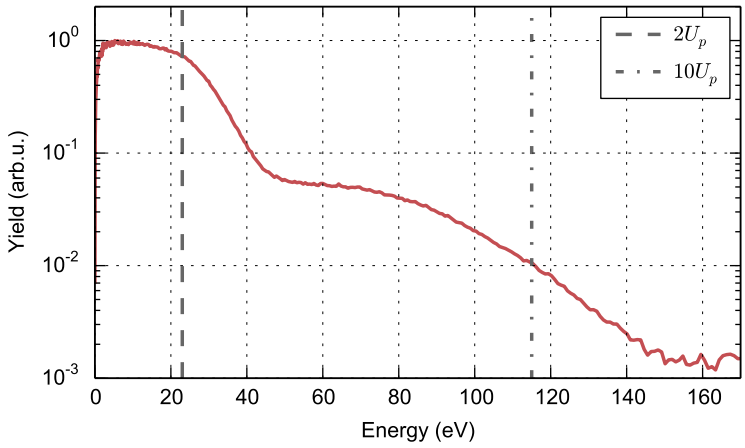

Figure 2.19: Photoelectron energy spectrum of unaligned CF_3I ionized by a 1300 nm wavelength probe pulse with an intensity of $7.0 \pm 0.6 \times 10^{13}\,\mathrm{W/cm^2}$ ($U_p = 11 \pm 1\,\mathrm{eV}$).

Using the definition of the ponderomotive potential $U_p = \frac{1}{4}A_0^2$, which is the cycle averaged kinetic energy of a free electron in an oscillating electric field, it is seen that $E_f^{max} = 2U_p$. This simple classical picture gives direct physical insight into experimentally observed photoelectron spectra. Fig. 2.19 shows an experimental photoelectron energy spectrum of *unaligned* CF_3I ionized by a 1300 nm wavelength probe pulse (see also Chapter 3). The photoelectron yield is rather constant up to a cut-off energy of $\approx$ 22 eV (dashed grey line), after which it drops off rapidly. Using the semi-classical picture outlined above, this cut-off energy can be interpreted as the maximum kinetic energy attainable by a classical photoelectron that is ionized with zero kinetic momentum, i.e. $2U_p$ [74].

The influence of the parent ion on the photoelectron motion has been neglected so far. Photoelectrons that are ionized at a time t_0 *before* the peak of the electric field never return to the exact location of the parent ion. Within the semi-classical approximation it is assumed that these photoelectrons do not interact with the parent ion after ionization, and are called *direct* electrons. A photoelectron created *after* the peak of the field does return to the parent ion and may re-scatter from it. The final step in the semi-classical model consists of an approximate treatment of re-scattering for those photoelectrons that return to the parent ion. For an electric field given by (2.139), and assuming that the initial position and velocity of the photoelectron at the time of ionization t_0 are zero, the position of the photoelectron at subsequent times can be obtained from the classical equations of motion and is given by

$$r(t) = \frac{A_0}{\omega}(\cos\omega t - \cos\omega t_0) + A_0(t - t_0)\sin\omega t_0 \qquad (2.142)$$

For a given time of ionization t_0 this equation can be evaluated numerically to obtain the time t_r at which the electron returns to its parent ion, i.e. $r(t_r) = 0$. Using (2.138), which gives the canonical momentum of the photoelectron

with zero kinetic momentum after ionization, and substituting into (2.136) an expression for the photoelectron momentum at the time of re-scattering t_r is obtained

$$\pi_r = -A_0(\sin\omega t_r - \sin\omega t_0) \tag{2.143}$$

At this point it is assumed that the photoelectron scatters *elastically* and instantaneously from the parent ion so that the direction of its momentum is changed by an angle θ_s. The momentum of the photoelectron immediately after re-scattering is given by

$$\boldsymbol{\pi_s} = \pi_r \begin{bmatrix} \cos\theta_s \\ \sin\theta_s \end{bmatrix} \tag{2.144}$$

which is a vector specified in terms of its components parallel and perpendicular to the electric field direction. After this point-like scattering event at the first return time, it is assumed that the photoelectron does *not* interact with the parent ion any further. Using (2.136), and assuming that the vector potential goes to zero at the end of the laser pulse, the *final* momentum at the detector is obtained

$$\boldsymbol{p_f} = \begin{bmatrix} A_0\sin\omega t_r + \pi_r\cos\theta_s \\ \pi_r\sin\theta_s \end{bmatrix} \tag{2.145}$$

The perpendicular component of the photoelectron momentum is not affected by the electric field so that the perpendicular component of $\boldsymbol{p_f}$ is identical to that of $\boldsymbol{\pi_s}$. The parallel component of $\boldsymbol{p_f}$ has an additional offset term of $A_0\sin\omega t_r$ that is due to the abrupt change of the propagation direction and subsequent propagation of the re-scattered photoelectron in the strong laser field. This offset can lead to a much larger final kinetic energy for a re-scattered photoelectron than can be achieved by direct photoelectrons. By numerically evaluating Equations (2.142)-(2.145) it can be shown that photoelectrons that have back-scattered, i.e. for which $\theta_s = 180°$, can reach a maximum kinetic energy of $\approx 10.01U_p$.

Again, the simple classical picture gives direct physical insight and can be used to explain the significant number of photoelectrons with kinetic energies well above $2U_p$ that can be observed in the experimental spectrum in Fig. 2.19. After a sharp drop in the photoelectron yield above the $2U_p$ cut-off, the yield plateaus in the energy range of 50 – 100 eV before dropping off more rapidly again. The cut-off energy at which the yield of these high-energy photoelectrons starts to drop rapidly corresponds to the $10U_p$ kinetic energy attainable by the re-scattered electrons in the semi-classical model. By estimating the position of the $2U_p$ and $10U_p$ cut-off energies it is possible to obtain an approximate laser field intensity from an experimental photoelectron spectrum. This technique was used to estimate the laser field intensity from the spectrum shown in Fig. 2.19 and yields $7.0 \pm 0.6 \times 10^{13}\,\mathrm{W/cm^2}$.

Figure 2.20 graphically illustrates the semi-classical model superposed on an experimental Photoelectron Angular Distribution (PAD) of unaligned CF_3I molecules (see also Chapter 3). For a fixed photoelectron re-scattering momentum $\boldsymbol{\pi_r}$, the momentum immediately after scattering $\boldsymbol{\pi_s}$ maps out a circle in momentum space as a function of the scattering angle θ_s that is centred around the origin. However, subsequent propagation of the scattered electron in the strong laser field leads to an *offset* of its momentum of $A_0\sin\omega t_r$ parallel to the laser field. The *final* photoelectron momentum $\boldsymbol{p_f}$ therefore lies on a circle of radius π_r with the appropriate offset.

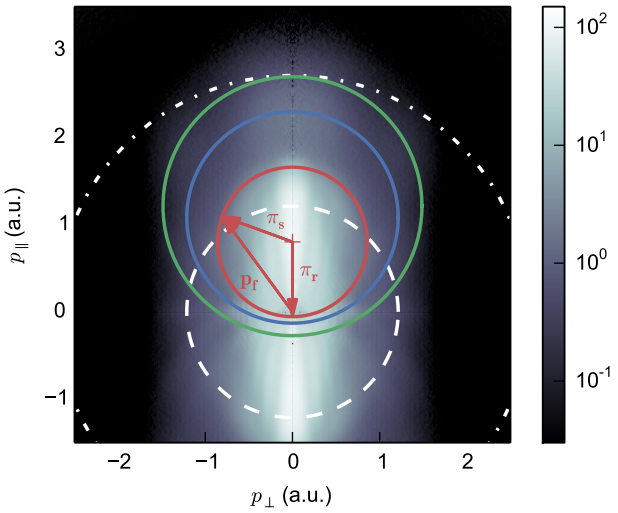

Figure 2.20: Scattered electrons with a fixed re-scattering momentum $\boldsymbol{\pi_r}$ have a final momentum $\boldsymbol{p_f}$ that lies on a circle with the radius π_r and an offset of $A_0 \sin\omega t_r$ parallel to the laser field. The angle between the vectors $\boldsymbol{\pi_r}$ and $\boldsymbol{\pi_s}$ is given by the scattering angle θ_s. The experimental Photoelectron Angular Distribution (PAD) is that of unaligned CF_3I ionized by a 1300 nm wavelength probe pulse with an intensity of $7.0 \pm 0.6 \times 10^{13}\,\mathrm{W/cm^2}$ (see Chapter 3 for experimental details). The coloured circles correspond to a scattering energy of (red) 10 eV, (blue) 20 eV and (green) 30 eV. White iso-energy circles are plotted at $2U_p$ (dashed circle) and $10U_p$ (dash-dotted circle) energies.

The semi-classical model introduced above is the cornerstone of the QRT procedure for extracting electron scattering cross-sections from strong-field ionized targets because it gives a *fixed* relation between the re-scattering momentum, scattering angle, and final momentum of the re-scattered photoelectrons [62]. According to the QRT, the electron scattering Differential Cross-Section (DCS) can be extracted from the PAD by plotting the photoelectron yield on a circle of fixed re-scattering energy as a function of the scattering angle. Figure 2.21 shows the electron scattering DCS extracted using the QRT procedure from two of the circular re-scattering cuts shown in Fig. 2.20 (red dots). The DCS for elastic electron scattering from the CF_3I molecule obtained from traditional electron beam experiments [75] (blue dots) is also plotted and shows a qualitative match with the QRT cross-sections.

In anticipation of the discussion in Chapter 3, the expected effects of molecular structure on the DCS shown in Fig. 2.21 are illustrated using simulated DCS curves (green lines). The simulation uses the IAM introduced in Sec. 2.5.1 in combination with atomic cross-sections obtained with the ELSEPA scattering code introduced in Sec. 2.4.1 [36]. It can be seen that the simulated *molecular* DCS (full green lines) and the 'atomic' DCS, which contains no molecular structure information, (dashed green lines) are very similar. Especially for large scattering angles, i.e. large momentum transfers, the curves are almost indistinguishable. Moreover, it is observed that strong oscillatory structure is clearly

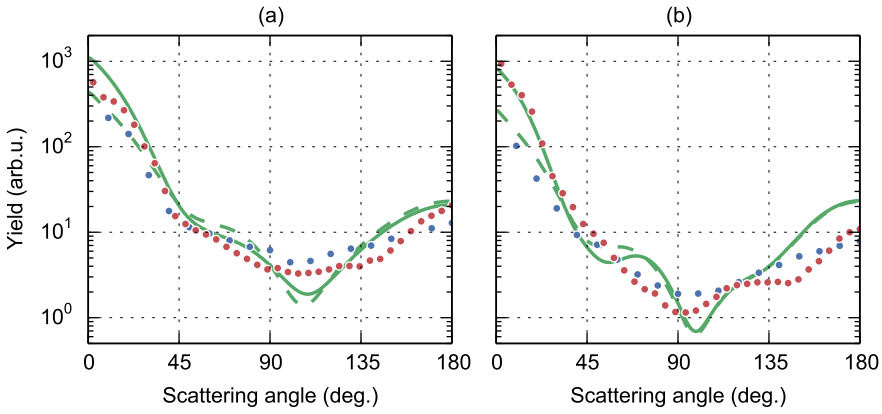

Figure 2.21: Electron scattering DCS for the CF_3I molecule as extracted from Fig. 2.20 (red dots) and from traditional electron beam experiments (blue dots) [75] for (a) 20 eV and (b) 30 eV scattering energy. The simulated molecular DCS calculated with the IAM and using atomic scattering amplitudes obtained from ELSEPA is also plotted (full green lines) together with the 'atomic' DCS, which is the *incoherent* sum of the C,F and I atomic DCS (dashed green lines).

visible in the 'atomic' DCS curves, which contain no molecular structure information. This means that it is in general not possible to directly extract molecular structure effects by simply looking at the oscillatory features within the DCS. In order to extract molecular structure information from the DCS as shown in Fig. 2.21, one must have highly accurate calculations of molecular cross-sections and be able to compare them to high fidelity experimental data with a noise level below the magnitude of the variations caused by molecular structure effects. Fortunately, in experiments with aligned molecules such difficulties can be very effectively alleviated by looking directly at the effect of changing molecular frame distributions on the DCS. Non-structural effects, such as 'atomic' scattering factors, can then be effectively subtracted from the experimental signal itself. This is the approach followed in Chapter 3 where experimental results from strong-field ionized and partially aligned molecules are presented.

There are two important points in the extraction procedure proposed within the QRT framework that must be mentioned here. First, the number of photoelectrons that has returned to the parent ion and experienced a hard re-collision[11] is small compared to the number of photoelectrons that have not returned to the parent ion, i.e. direct electrons. Consequently, the direct electrons, which do not contain LIED effects, constitute a major part of the total yield of photoelectrons in an experiment. However, from the semi-classical picture discussed above it is clear that re-scattered photoelectrons can reach much higher final kinetic energies than direct electrons. From the experimental spectrum in Fig. 2.19 it can be seen that direct photoelectrons dominate the total yield up to an energy of $\approx 4U_p$. The QRT picture is thus expected to be a valid

[11] A hard re-collision leads to a large momentum transfer, and thus to a higher spatial resolution in diffraction imaging (see Sec. 2.5.1).

description of the PAD in the kinetic energy range above $4U_p$. Second, for each final momentum $\boldsymbol{p_f}$ there are in fact *two* possible sets of solutions for the time of birth and re-collision (t_0, t_r). This means that there are also two distinct re-scattering momentum $\boldsymbol{\pi_r}$ solutions for each final momentum $\boldsymbol{p_f}$. Such an indeterminacy is of course unwanted in the case of LIED, where a one-to-one mapping between π_r and $\boldsymbol{p_f}$ is required in order to extract electron scattering cross-sections. Fortunately, the ionization time t_0 for one of set of the trajectories is closer to the peak of the laser electric field so that these normally dominate the photoelectron yield and scattering cross-sections can be extracted without ambiguity [76].

Chapter 3

Laser Induced Electron Diffraction in aligned molecules

3.1 Introduction

Laser Induced Electron Diffraction (LIED) is a new and promising technique for the realization of the long-standing goal of *imaging* structural dynamics in molecules at femtosecond time scales and with Ångström spatial resolution. It was theoretically proposed more than a decade ago[1] following the discovery that strong-field ionized atoms and molecules display a pronounced plateau in their photoelectron spectrum that could be ascribed to re-scattering of the photoelectrons driven by the laser field [1, 2, 3]. The basic theoretical concepts of LIED were introduced in Sec. 2.6 using a semi-classical model developed in some of the earliest theoretical publications on this subject [2, 3]. Sec. 2.6 also introduced the Quantitative Re-scattering Theory (QRT) proposed by Chen *et al.* [62] that has been used successfully in a number of experimental publications on LIED to date [77, 69, 78, 79, 80]. The QRT is also used as a basis for the description of the LIED experiments presented in this chapter and is applied to the simulation of experiments with *aligned* molecules using an approach similar to that found in the recent publication by Yu *et al.* [81].

Table 3.1 gives an overview of publications with experimental work related to LIED and some of their relevant experimental details. Though the work by Niikura *et al.* [1] did not provide direct evidence for LIED effects, it was the first experimental work that explored the use of re-scattered photoelectrons for ultra-fast imaging of the molecular structure. The first direct experimental evidence of LIED effects in the Photoelectron Angular Distribution (PAD) of N_2 and O_2 molecules was provided by Meckel *et al.* [68]. In this pioneering experiment the use of impulsive laser alignment [82, 83] played a crucial role. In Sec. 2.5.1 it

[1] The publication by Zuo *et al.* [60] in 1996 that introduced the term Laser Induced Electron Diffraction (LIED) describes a technique that would extract molecular structure from the interference of photoelectrons that are coherently emitted from the individual atomic centres within the molecule. This is conceptually different from what is understood by LIED today, which is a technique that crucially relies on diffraction by the *re-scattered* photoelectrons.

was shown that manipulating the molecular frame, through partial alignment of the molecules, can be used to extract the molecular structure factors from the electron scattering cross-section in a very direct way. Meckel *et al.* were able to identify LIED effects in the PAD of strong-field ionized N_2 and O_2 by looking at the *normalized difference*, i.e. the difference divided by the sum, of the PADs of aligned and anti-aligned molecules. Though most subsequent LIED experiments have employed aligned molecules in some way, the use of molecular alignment as a tool to directly extract molecular structure effects was only, unsuccessfully, employed in the work by Lee *et al.* [84]. All other experiments listed in Table 3.1 use the QRT to extract an electron scattering Differential Cross-Section (DCS) from the PAD of a strong-field ionized molecule. By applying the Independent Atom Model (IAM) and subtracting a simulated 'atomic' DCS from the experimental data the molecular structure was then recovered [77, 69, 78, 79, 80].

Table 3.1: Overview of publications with experimental work on LIED.

Ref.	Year	Molecule	λ (μm)	Aligned	Detection
Niikura *et al.* [1]	2002	H_2	0.8	-	H^+-TOF
Meckel *et al.* [68]	2008	O_2, N_2	0.8	Yes	COLTRIMS [85] ($e^- + O_2^+/N_2^+$)
Okunishi *et al.* [77]	2011	O_2, CO_2	0.8	Yes	e^--TOF
Blaga *et al.* [69]	2012	O_2, N_2	2.0/2.3	No	e^--TOF
Lee *et al.* [84]	2012	O_2, N_2, CO_2	0.8	Yes	VMI [86]
Xu *et al.* [78]	2014	O_2, N_2	2.0/2.3	Yes	e^--TOF
Pullen *et al.* [79]	2015	C_2H_2	3.1	Yes	COLTRIMS [85] ($e^- + C_2H_2^+$)
Ito *et al.* [80]	2016	C_6H_6	1.65	No	e^--TOF

The experiment by Blaga *et al.* [69] is a milestone experiment that demonstrated the advantages of performing LIED experiments using long wavelength probe pulses. The first LIED experiments were performed using probe pulses with a wavelength of 800 nm, which resulted in photoelectron re-collision energies in the 30 – 40 eV range. By using probe pulses of 2.0 and 2.3 µm wavelength Blaga *et al.* succeeded in increasing the re-collision energy of the photoelectrons to 100 – 200 eV, while keeping the laser intensity at a similar level as in the 800 nm experiments. The bond length retrieved by Blaga *et al.* for the O_2 target was 0.1 – 0.15 Å shorter than that of the O_2 neutral molecule, which is significant considering their estimated spatial resolution of 0.05 Å. This was interpreted

as a possible indication for structural dynamics after ionization. The O_2^+ bond length is 0.1 Å smaller than that of the neutral molecule so that the contraction of the molecule after ionization, and within the few femtoseconds it takes for the photoelectron to return and re-collide with the parent ion, would explain the observed discrepancy. The retrieved bond length for the N_2 target agreed with the neutral molecule geometry within the estimated experimental error. This is consistent with the interpretation of the O_2 results because the N_2^+ ion bond length differs by less than 0.025 Å from that of the neutral molecule. The success of Blaga *et al.* in increasing the spatial resolution and observing a possible hint of structural dynamics using LIED has led to the use of long wavelength laser pulses in most subsequent experiments.

The majority of LIED experiments performed to date used simple diatomic target molecules such as N_2 and O_2. Recent publications by Pullen *et al.* [79] on acetylene (C_2H_2) and by Ito *et al.* [80] on benzene (C_6H_6) represent the first attempts to apply the LIED technique to larger, more complex systems. The experiment by Pullen *et al.* was performed using a Cold Target Recoil Ion Momentum Spectroscopy (COLTRIMS) setup that is capable of detecting all electron and ion fragments, and their momenta, resulting from an individual ionization event [85]. When considering all detected electrons Pullen *et al.* were unable to derive the molecular structure from the DCS, but when considering only those electrons coinciding with the production of a singly charged molecular ion, i.e. $C_2H_2 \rightarrow e^- + C_2H_2^+$, they were able to observe LIED effects and extract the C–C *and* C–H bond lengths successfully. They therefore suggested that coincidence detection techniques are necessary in order to perform LIED experiments, at least with more complex molecules, because one must select those electrons that are coincident with the singly charged molecular ion in order to distinguish from those that are generated by other processes and result in experimental background. The first LIED experiments by Meckel *et al.* were indeed performed with a COLTRIMS setup and considered electrons that coincided with the O_2^+ and N_2^+ ion production, though Meckel *et al.* did not explicitly state that using such a detection scheme was necessary. On the other hand, the experiments by Blaga *et al.*, which were performed with an electron Time-Of-Flight (TOF) setup that can only detect the total electron yield, seemed to suggest that coincident detection is not a necessary requirement. More recently, Ito *et al.* [80] performed experiments on benzene using an electron TOF detector and were able to extract the C–H and C–C bond lengths by applying the same QRT procedure as Pullen *et al.*, though certain parts of the experimental data for backscattered photoelectrons were omitted because they deviated too much from the theoretical curves.

In this chapter a series of experiments are presented that investigate the effect of the *molecular frame* on the PAD of impulsively aligned and strong-field ionized CF_3I molecules using a Velocity Map Imaging Spectrometer (VMIS). It is shown that using the impulsive laser alignment technique enables taking *differential measurements* that bring out directly and clearly LIED effects in the PAD, even for a relatively *complex molecule* such as CF_3I and using a non-coincident detection setup such as the VMIS. The comparison of the experimental results at different laser intensities and at two different probe wavelengths, i.e. 800 and 1300 nm, shows that the LIED effect is robust and reproducible for a wide range of experimental conditions and at comparatively low re-collision energies. Moreover, the first results from Time-Dependent Density Functional

Theory (TDDFT) calculations performed by DeGiovannini *et al.* [87] indicate that the contributions from multiple molecular orbitals can also be identified in the experimental PADs due to the distinct dependence on the molecular frame of the individual orbitals.

Section 3.2 will give a short overview of the experimental setup and the data acquisition and processing methods employed in obtaining the experimental data. The experimental results are presented in Sec. 3.3. In Sec. 3.4 a semi-classical model based on the QRT description of the re-scattering process is applied in order to simulate the experiments on aligned CF_3I molecules and identify LIED effects. Besides the molecular-frame-dependent features in the high-energy range of the PAD, which are attributed to LIED effects using the semi-classical model, pronounced features in the low-energy range of the PAD are also observed. These low-energy features cannot be described by the semi-classical QRT model that is used to identify the LIED effects because it does not take direct electrons, i.e. electrons that have not re-scattered with the ion, into account. An attempt to use the Molecular Strong Field Theory (MSFT) developed by Milošević *et al.* [88, 89, 90, 91] to improve the theoretical description of the experiment at the low-energy range met with some difficulties. Section 3.5 presents the MSFT calculation results and analyses them by comparing them to experimental results. The first results from Time-Dependent Density Functional Theory (TDDFT) calculations are presented in Sec. 3.6 and show a good match with the experimental data at all photoelectron energies. The TDDFT calculations indicate that the contribution of not only the Highest Occupied Molecular Orbital (HOMO) but also of the lower lying HOMO-1 are significant and can be identified in the experimental results.

3.2 Experimental setup

3.2.1 Experimental apparatus

The experiment was performed using a pump-probe setup shown schematically in Fig. 3.1. A commercially available ultrafast Ti:Sapphire laser system providing 2 mJ, 30 fs laser pulses at a repetition rate of 1–1.5 kHz[2] was used. The Ti:Sapphire laser output was split into a pump and a probe beam that are used to align and ionize the CF_3I molecules, respectively. The pump-probe delay was introduced using a mechanical linear stage with a 10 cm range of motion and a 1 µm positioning resolution.

The CF_3I molecules were aligned through the use of the impulsive laser alignment technique [92, 83]. Impulsive laser alignment is achieved by using a short and intense laser pulse to give the molecule a strong rotational 'kick' through its induced dipole moment. This leads to the population of a rotational wavepacket that re-phases periodically, giving rise to *alignment revival* peaks at specific time-delays following the alignment pulse. The alignment laser pulse must be short with respect to the rotational period of the molecule, and should be as intense as possible without leading to multi-photon ionization[3]. To achieve

[2]The acquisition speed in these experiments was not limited by the repetition rate of the laser, but rather by the repetition rate of the pulsed molecular beam source.

[3]The wavelength of the alignment pulse must be such that single photon ionization is not possible.

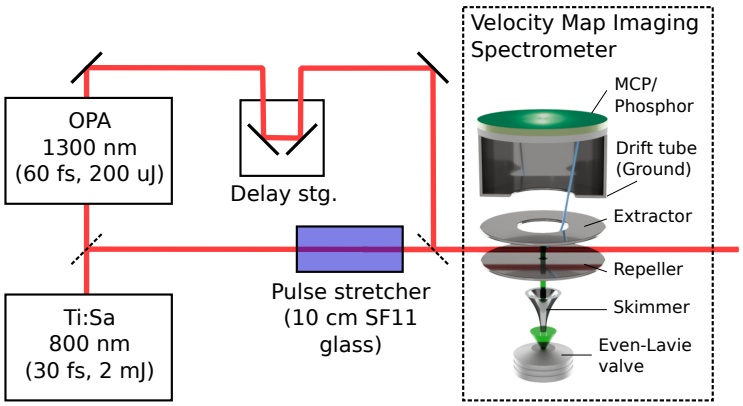

Figure 3.1: Schematic of the experimental pump-probe setup. The Optical Parametric Amplifier (OPA) is used for the 1300 nm experiments to down-convert the pump pulse wavelength.

high degrees of alignment while avoiding ionization of the CF_3I molecule, the pump pulse duration is stretched to 1.2 ps, which is short compared to the CF_3I rotational period of 327.4 ps, by propagation through a 10 cm long (SF11) glass block. The pump beam is then telescoped to an appropriate size so that its *focal size* is approximately twice as large as that of the probe beam. This increases the effective degree of alignment because the molecules that are ionized by the probe pulse have been illuminated more uniformly with the highest pump pulse intensities. Any residual ionization by the pump pulse observed with the VMIS was eliminated by reducing the size of the pump beam with an iris.

For experiments using a 1300 nm probe wavelength, the pump and probe pulse energies were both 1 mJ. A commercially available Optical Parametric Amplifier (OPA) was used to down-convert the wavelength with approximately 20% efficiency, resulting in probe pulse energies of $\sim$200 µJ. The probe intensity was adjusted using a $\lambda/2$-waveplate and polarizer in order to perform experiments at a range of probe intensities of $4 \times 10^{13} - 2 \times 10^{14}$ W/cm^2. The probe intensity was estimated from the experimental PADs by looking for the $2U_p$ and $10U_p$ cut-off energies in the photoelectron spectrum, as detailed in Sec. 2.6. The pump and probe pulses were re-combined collinearly using a dichroic mirror and focused into the VMIS with an uncoated UVFS plano-convex lens with a 200 mm focal length.

For experiments using an 800 nm probe wavelength, the pump and probe pulse energies were 1.4 and 0.6 mJ, respectively. The OPA was not required in this case. Because both the pump and the probe arms have the same wavelength, it was not possible to use a dichroic mirror to recombine the two arms collinearly. The two beams were steered such that they were as close as possible and parallel to each other before being focused with a lens into the VMIS. The foci of the two beams would then overlap at a small angle of $\sim$6° within the detector. The final focusing lens was a BK-7 plano-convex lens with a broadband anti-reflective coating and a 200 mm focal length.

The photoelectron and photoion momentum distributions were recorded using a Velocity Map Imaging Spectrometer (VMIS) [86]. The VMIS consists of

two electrodes, i.e. the repeller and the extractor, that are shaped such that they form an electrostatic lens that projects the full 3-D momentum distribution of the charged particles onto the 2-D detection plane. The detector consists of a Multi-Channel Plate (MCP), which acts as a charged particle amplifier, and a phosphor screen, which converts the electron current signal from the MCP into a light image that is digitized with a CCD camera. The detector image I is given by

$$I(p_x, p_y) = \int \rho(p_x, p_y, p_z)\, \mathrm{d}p_z \tag{3.1}$$

where ρ is the full 3-D momentum distribution as a function of the Cartesian momentum vector components p_x, p_y and p_z. That is, the momentum distribution is 'flattened' such that the momentum of the charged particles in the plane perpendicular to the optical axis of the VMIS, i.e. p_x and p_y, can be directly observed in the detector image, while the momentum parallel to this axis, i.e. p_z, cannot. If the full momentum distribution of the particles is cylindrically symmetric[4] *and* if the symmetry axis lies in the xy-plane, (3.1) is equivalent to the Abel projection. The full 3-D momentum distribution may then be obtained by applying an *Abel inversion*. The Abel inversion code used to recover the 3-D PADs in this thesis is based on the BASEX method introduced by Dribinski *et al.* [95].

The VMIS used in these experiments is specifically designed to image photoelectrons with very high kinetic energies of up to 1.5 keV. The imaged kinetic energy range can be varied by changing the voltages applied to the repeller and extractor electrodes. Using lower voltages reduces the imaged kinetic energy range and increases the image size. The ratio between the repeller and extractor voltages is rather constant, i.e. $V_{ext}/V_{rep} \approx 0.92$, and can be used to optimize the image focus. In order to convert from the image pixel units to absolute momentum units, the VMIS must be calibrated using known features from the recorded spectra. The PADs of strong-field ionized atoms or molecules show pronounced Above-Threshold Ionization (ATI) peaks, which are successive peaks that are due to the multi-photon ionization with an increasing number of absorbed photons . By measuring the distance between the observed ATI peaks in the image and setting this equal to the photon energy it is possible to obtain a calibration constant for the conversion from image pixel units to energy units.

A cold, dense sample of CF_3I molecules is produced by a supersonic molecular beam source [96]. The target molecules are seeded in helium with a ratio of 1:200 – 1:1000 and expanded into the vacuum at backing pressures of 6 – 9 bar. The supersonic expansion of the gas from the high pressure valve chamber into the vacuum results in collisional cooling of the CF_3I molecules [96]. The gas sample is introduced into the vacuum chamber by an Even-Lavie valve [97] operated at a repetition rate of 300 Hz and with a nozzle size of 100 µm. The valve is located in a separate vacuum compartment, i.e. source chamber, that is connected to the VMIS compartment, i.e. detector chamber, by a baffle equipped with a molecular beam skimmer. The expanding gas originating from the valve passes through the 1 mm diameter skimmer and forms a well-defined molecular beam that is intersected by the pump-probe laser beams at an interaction point

[4]Non-cylindrically symmetric momentum distributions may be recovered using tomographic re-construction, which requires obtaining the 2-D projections at different rotations with respect to the projection axis [93, 94].

within the VMIS. The source and detector chambers are pumped differentially by two 400 l/s turbomolecular pumps. This ensures that the detector chamber pressure is below the 10^{-6} mbar that is required for VMIS operation, while allowing for higher pressures of 10^{-4}–10^{-3} mbar in the source chamber containing the valve. The valve is mounted on a XYZ vacuum manipulator that is used to align the valve nozzle axis with the skimmer and to adjust its distance to the interaction point. The distance to the interaction point is adjusted such as to maximize the molecular beam density while maintaining the degree of molecular alignment and the low pressure in the detector chamber.

3.2.2 Data acquisition and processing

Molecular structure effects are very small compared to the overall signal in LIED experiments. As discussed in Sec. 2.6, the photoelectron spectrum is in fact dominated by direct electrons that do *not* re-scatter from the molecular ion after ionization and thus form a background contribution. Experiments on *unaligned* molecules make use of the fact that there are regions of the photoelectron spectrum where re-scattered photoelectrons are dominant. However, even in spectra containing only scattered electrons, molecular structure effects are very small compared to the 'atomic' background that does not contain molecular structure information, as was shown in Sec. 2.5.1. In experiments on unaligned molecules, the atomic background needs to be known very precisely in order to extract molecular structure effects from the data. Using impulsive laser alignment of the molecules presents the unique opportunity to enhance molecular contributions within the PAD by looking at the normalized difference of the momentum distributions for aligned and anti-aligned molecules (see also Sec. 2.5.1). Normalized difference images are constructed directly from the experimental data as follows

$$I_\delta = \frac{I_A - I_B}{I_A + I_B} \tag{3.2}$$

where I_A and I_B are the momentum distributions at the alignment and anti-alignment revival peaks, respectively. The normalized difference images convey in a direct way the dependence of the photoelectron spectrum on the molecular frame and are used in the following sections to extract LIED effects from the raw photoelectron spectra.

Long-term stability of the experimental setup is another key factor in performing LIED experiments. The normalized difference images are background subtracted in the sense that in principle they represent the molecular-frame dependent signal only, which eliminates some important background contributions from the spectra. However, long-term drifts can still lead to systematic errors in the difference images if the acquisition of the individual momentum maps of which it consists takes place on a similar time scale. In order to suppress effects of the long-term drifts in laser power and beam pointing, molecular beam density, etc. the acquisition is performed repetitively. Individual momentum maps for each pump-probe delay, e.g. I_A and I_B, are acquired with a relatively short averaging period of 30 s. This averaging time is long enough to average out short-term variations, but is short with respect to the long term drifts in the system, which take place on the order of tens of minutes. The acquisition of the full pump-probe delay sequence is then repeated up to 60 times, resulting in a total acquisition time of 2 to 3 hours.

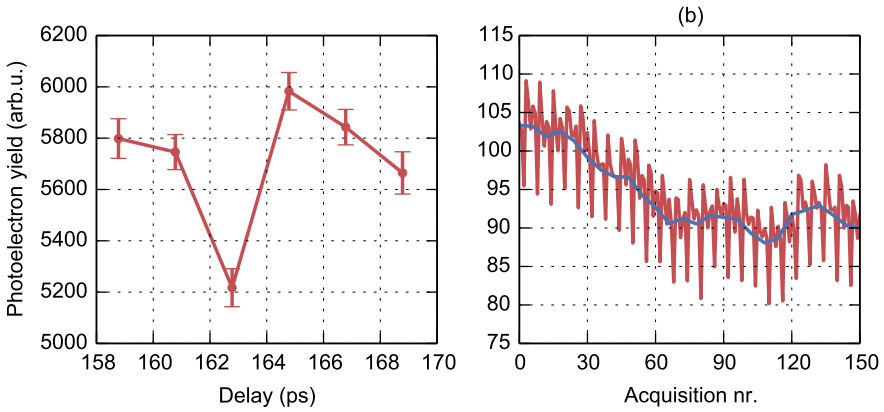

Figure 3.2: Example of the repetitive sequence scanning method. (a) The total average intensity per pump-probe delay point around the alignment revival period. (b) Average intensity per individual acquisition within the repetitive sequence (red line). The long-term drift component (blue line) is calculated by averaging over all 6 pump-probe delay points for each sequence.

Figure 3.2 shows an example of an experimental sequence obtained with the repetitive acquisition scheme. This acquisition sequence consists of 6 pump-probe delay points where the middle two points coincide with the alignment and anti-alignment revival peaks respectively. The total photoelectron yield per delay point is plotted in Fig. 3.2(a). Each delay point consists of 60 *individual* acquisitions with a total of 360 acquisitions for the full sequence. Figure 3.2(b) shows the photoelectrons yield for some of the individual acquisitions (red line). Long-term system drift causes an overall signal level shift (blue line) that is clearly distinguishable from the intensity variations caused by the alignment revivals. The repetitive acquisition scheme also enables statistical analysis of the data illustrated in Fig. 3.2(a) in which the standard deviation of the average intensity, after subtraction of the long-term drift component, is plotted.

3.3 Experimental results

3.3.1 Alignment characterization

The 1.2 ps pump (alignment) pulse gives the CF_3I molecule a strong rotational 'kick' through its induced dipole moment, and populates a rotational wavepacket which re-phases periodically [92]. This leads to *alignment peaks* at which the C–I molecular axis is aligned parallel to the pump polarization, and anti-alignment peaks at which the C–I molecular axis is perpendicular to the pump polarization. The molecules are not oriented, so that they point up and down with equal probability, and are free to rotate along the C–I axis. Probing the molecules during alignment/anti-alignment revival peaks also ensures that they are ionized under field-free conditions and avoids the influence of the alignment field on the photoelectron spectra.

The degree of alignment was experimentally characterized by imaging the

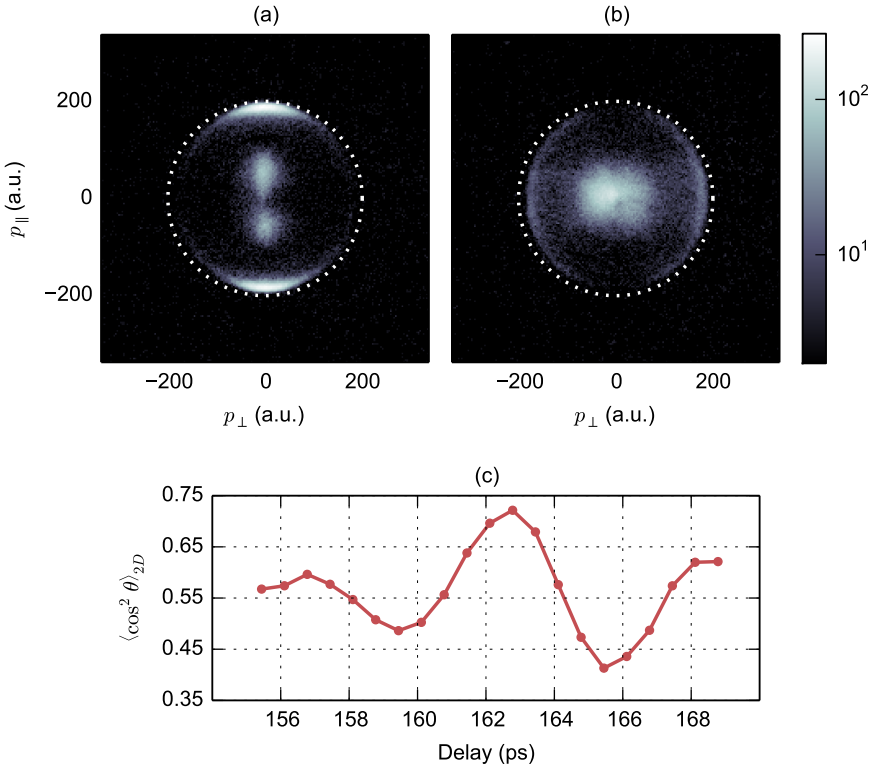

Figure 3.3: I^+ 2-D momentum maps at the (a) alignment and (b) anti-alignment revival peaks, and (c) the degree of alignment $\langle\cos^2\theta\rangle_{2D}$ as a function of pump-probe delay. The probe wavelength and intensity were 800 nm and $7.5 \pm 0.8 \times 10^{13}$ W/cm^2. The alignment pulse polarization is along the $p_\parallel$ axis, and the probe polarization is *perpendicular* to the image plane. The white iso-energy circle at 2.37 eV indicates the expected kinetic energy release resulting from the the Coulomb explosion of the I^+/CF_3^+ pair from the equilibrium I–C distance in the molecule of 2.14 Å.

I^+ momentum distributions as a function of the pump-probe delay. The I^+ 2-D momentum maps at the alignment and anti-alignment revival peak delay times are shown in Fig. 3.3(a) and (b), respectively. The polarization of the *probe* pulse is here *perpendicular* to the VMIS image. This means that the I^+ 2-D momentum map obtained with the VMIS cannot be Abel-inverted, because the symmetry axis of the full 3-D momentum distribution, which is parallel to the probe polarization, is not in the xy-plane of the spectrometer. However, this arrangement of the probe polarization results in a 2-D view of the I^+ momentum distribution that is circularly symmetric in the absence of the *alignment* pulse, which is polarized along the $p_\parallel$ axis. The anisotropy in the 2-D momentum images shown in Fig. 3.3(a) and (b) is caused by the change in the molecular axis distribution that results from the application of the alignment pulse, and may be used to quantify the degree of molecular alignment [22]. The sharp feature in the I^+ distribution around 2.37 eV (dotted circle) matches the I^+

kinetic energy release expected from the Coulomb explosion of the I^+/CF_3^+ pair from the equilibrium I–C distance of 2.14 Å. The degree of alignment is quantified by calculating the expectation value $\langle \cos^2\theta \rangle_{2D}$ of the 2-D momentum map for a small range of momenta around the Coulomb explosion channel and is shown in Fig. 3.3(c) as a function of the pump-probe delay.

3.3.2 Photoelectron spectra

In order to bring out molecular frame effects in the Photoelectron Angular Distribution (PAD) these distributions are recorded at the alignment and anti-alignment revival peaks. The experimental PADs taken at the alignment and anti-alignment peaks that were observed in the I^+ momentum maps shown in Fig. 3.3, are shown in Fig. 3.4(a) and (b), respectively. Whereas the difference between these two PADs is relatively hard to observe directly from these images, the normalized difference image of these two PADs, shown in Fig. 3.4(c), displays clear modulations that are related to the change in the molecular alignment distribution. The PADs taken at the alignment and anti-alignment peaks for an experiment using a 1300 nm probe wavelength are shown in Fig. 3.5(a) and (b). The difference between these two PADs is even harder to observe than was the case for the 800 nm probe wavelength experiment, but the normalized difference image, shown in Fig. 3.5(c), again shows clear modulations.

Using a semi-classical picture of molecular strong-field ionization, it was shown in Sec. 2.6 that photoelectrons that have *not* interacted with the parent molecule, i.e. direct electrons, may reach final kinetic energies that are much lower than that attainable by the photoelectrons that *have* re-collided with the parent ion. It was shown that the total photoelectron yield is dominated by the direct electrons up to an energy of $\approx 4U_p$, where U_p is the ponderomotive potential of the laser field. Re-scattered photoelectrons dominate the photoelectron yield above the $4U_p$ energy, and may reach, according to the semi-classical picture, final energies of up to $10U_p$. The normalized difference images may therefore roughly be divided in a low ($< 4U_p$) and a high energy region (4–$10U_p$) that are indicated in Figs. 3.4(c) and 3.5(c) by the dashed and dash-dotted circles, respectively. In the low-energy region ($< 4U_p$) direct *and* re-scattered photoelectrons both contribute to the modulations observed in the normalized difference images. Factors such as molecular orbital shape [68] and photoelectron holographic interference [98], which is due to the interference between the direct and the re-scattered photoelectrons, may significantly contribute to the observed modulations in this energy range. This complicates the interpretation of the experimental data in terms of the LIED effect. However, in the high-momentum region ($4 - 10U_p$), where re-scattered photoelectron contributions dominate, a pronounced variation of the electron signal along the polarization axis ($p_\parallel$) can be seen in both the 800 and the 1300 nm data. Along this axis the contribution of photoelectrons that have experienced a hard re-collision, i.e. $\theta_s \approx 180°$, with the parent ion is dominant and should therefore be very suitable for diffraction imaging [76].

At both the 800 and 1300 nm probe pulse wavelengths, the experiments were performed for several intensities in the range of $4 \times 10^{13} - 2 \times 10^{14}\,\mathrm{W/cm^2}$. The probe intensities were estimated from the experimental data by estimating the position of the $2U_p$ and $10U_p$ cut-off energies in the photoelectron energy spectrum, as detailed in Sec. 2.6. Figures 3.6 and 3.7 show the normalized

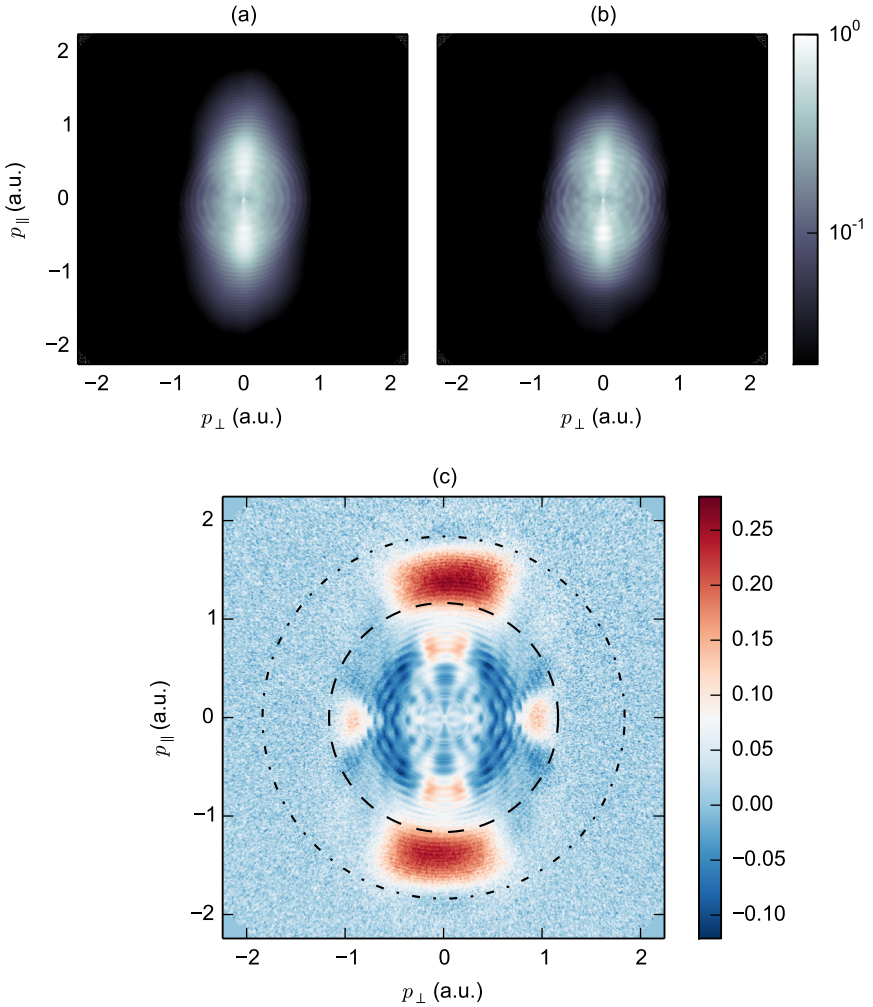

Figure 3.4: Photoelectron Angular Distributions (PADs) at the (a) alignment and (b) anti-alignment revival peak, and (c) their normalized difference. The probe wavelength and intensity were 800 nm and $7.5 \pm 0.8 \times 10^{13}\,\mathrm{W/cm^2}$, respectively. Both the probe and the alignment pulse are polarized parallel to the $p_\parallel$ axis. The iso-energy circles plotted in (c) indicate the $4U_p$ (dashed circle) and $10U_p$ (dash-dotted circle) energies.

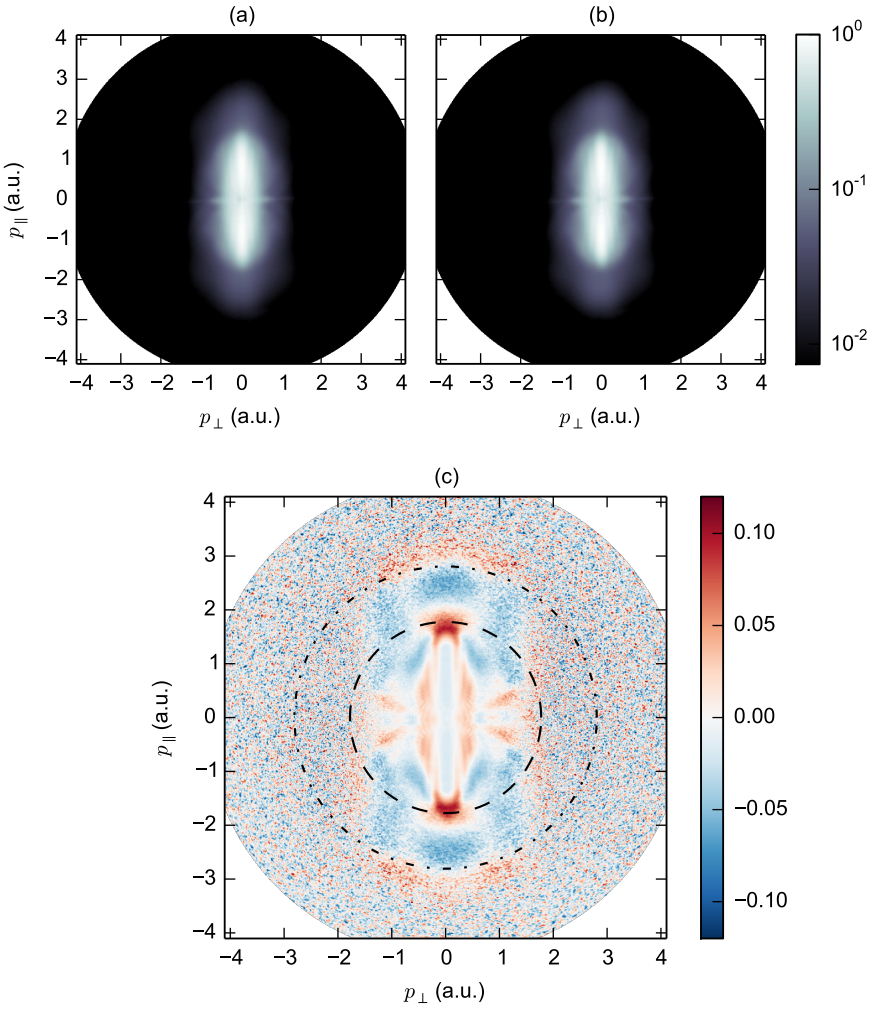

Figure 3.5: Photoelectron Angular Distributions (PADs) at the (a) alignment and (b) anti-alignment revival peak, and (c) their normalized difference. The probe wavelength and intensity were 1300 nm and $7.0 \pm 0.6 \times 10^{13}\,\mathrm{W/cm^2}$, respectively. Both the probe and the alignment pulse are polarized parallel to the $p_\parallel$ axis. The iso-energy circles plotted in (c) indicate the $4U_p$ (dashed circle) and $10U_p$ (dash-dotted circle) energies.

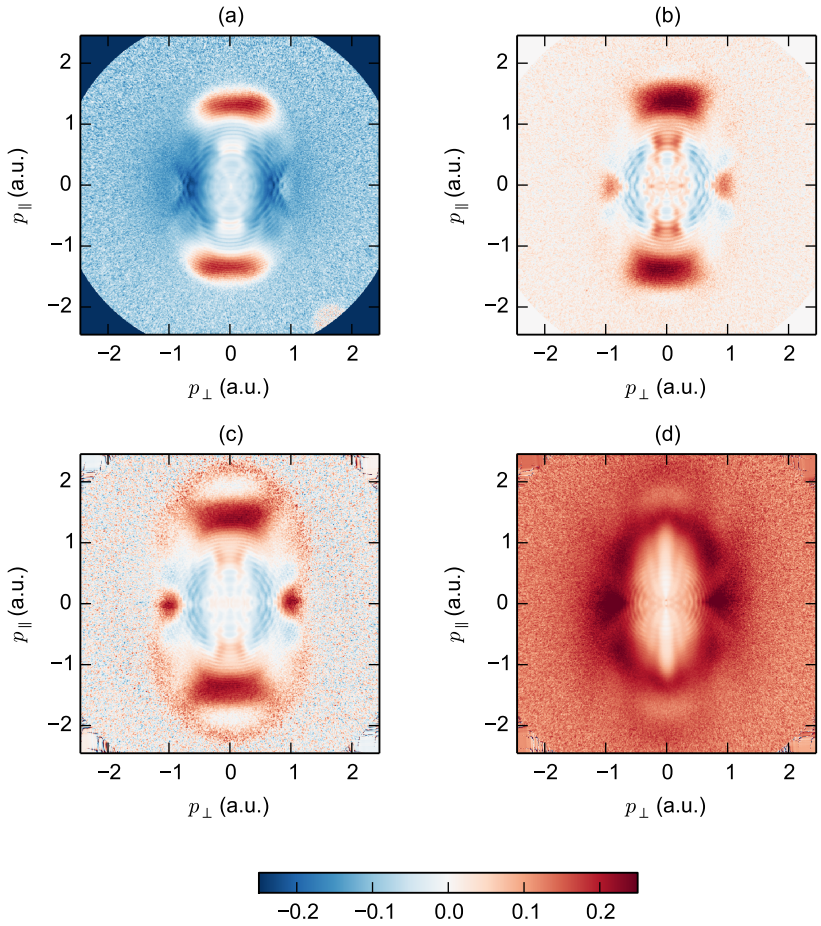

Figure 3.6: Normalized difference images at 800 nm probe wavelength for four different probe intensities: (a) $3.7 \pm 0.4 \times 10^{13}$, (b) $7.5 \pm 0.8 \times 10^{13}$, (c) $9.6 \pm 1.1 \times 10^{13}$ and (d) $2.1 \pm 0.3 \times 10^{14}$ W/cm^2.

difference images for different intensities recorded using the 800 and 1300 nm probe wavelengths, respectively. The normalized difference images at probe intensities below $\sim 1 \times 10^{14}$ W/cm^2 show a relatively similar picture in both the 800 and the 1300 nm experiments. In the 800 nm case, the normalized difference images in Figs. 3.4(a), (b) and (c) show a clear positive contribution along the $p_\parallel$ axis for momenta > 1 a.u. In 3.4(c) a dip in the signal for momenta > 1.8 a.u. that follows this positive contribution can also be seen. In the 1300 nm case, the low probe intensity image shows a level shift with respect to the mid-intensity one. That is, the signal in the low-intensity image is mostly around zero or below, whereas in the mid-intensity image there are much stronger positive contributions. However, in both images there is a relative enhancement in signal along the $p_\parallel$ axis for momenta > 1 a.u., followed by a *dip* in the signal for momenta > 2 a.u. These signal variations are robust and do not depend strongly on the probe intensity, which should be the case for structural effects such as

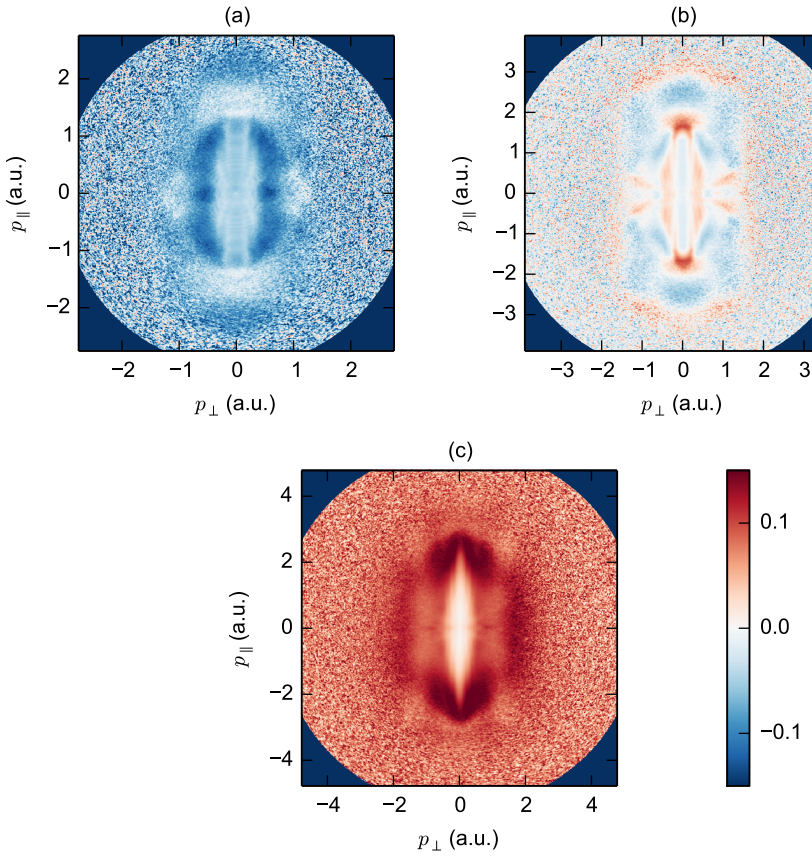

Figure 3.7: Normalized difference images at 1300 nm probe wavelength for three different probe intensities: (a) $4.9 \pm 0.5 \times 10^{13}$, (b) $7.0 \pm 0.6 \times 10^{13}$ and (c) $1.9 \pm 0.3 \times 10^{14}$ W/cm^2.

diffraction. In the next section a semi-classical model will be used to show that diffraction effects should indeed result in modulations such as those observed in the experimental data.

At high probe intensities, the normalized difference images Figs. 3.6(d) and 3.7(c) become *qualitatively* different from the lower intensity images. The modulations that were visible in the lower intensity normalized difference images, which are attributed to LIED effects, are almost completely washed out. Figure 3.8 shows the photoelectron energy spectra corresponding to the normalized difference images shown in Fig. 3.7. In the energy spectra for the two lowest probe intensities, shown in Figs. 3.8(a) and (b), a clear re-collision plateau with a $10U_p$ cut-off can be identified. The modulations in the normalized difference images that are attributed to LIED effects are indeed located in the energy range of the re-collision plateau. In the energy spectrum for the highest probe intensity, shown in Fig. 3.8(c), only the $2U_p$ cut-off for direct electrons is clearly visible. The $10U_p$ cut-off could not be identified, even though the VMIS settings were such that it should have been possible to measure up to this energy range.

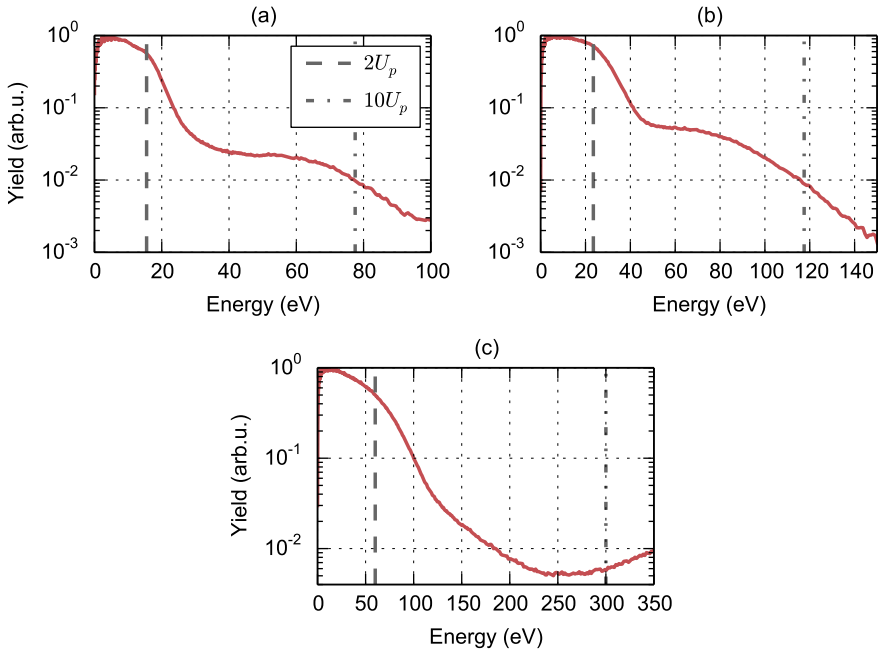

Figure 3.8: Photoelectron energy spectrum at 1300 nm probe wavelength for three different probe intensities: (a) $4.9 \pm 0.5 \times 10^{13}$, (b) $7.0 \pm 0.6 \times 10^{13}$ and (c) $1.9 \pm 0.3 \times 10^{14}$ W/cm^2.

The normalized difference image corresponding to this spectrum, i.e. Fig. 3.7(c), does not show significant modulations in the energy range in which the partially visible re-collision plateau should be located.

3.4 Semi-classical model calculations

To understand the high-momentum features observed in the photoelectron spectra and make the connection to LIED effects a semi-classical model can be used which is based on theory from [3, 62, 76]. The principles of the semi-classical model were introduced in Sec. 2.6. In Sec. 3.4.1 the concrete form of the semi-classical QRT model used to simulate the LIED experiments will be first outlined. In this model the re-collision step is distinct from the field-driven photoelectron dynamics and was modelled using two different approaches. The first simulations, presented in Sec. 3.4.2, use the Plane Wave Born Approximation (PWBA) in combination with the IAM to obtain molecular scattering amplitudes (see also Sec. 2.4.2). This model shows a rather large disagreement with the experimental data when all the atoms in the molecule are included in the calculation. Interestingly, removing the fluorine atoms from the molecule resulted in a reasonable quantitative match with the experimental data. One possible cause for this discrepancy comes from the *atomic* scattering amplitudes that are calculated using the PWBA, which becomes increasingly inaccurate for lower scattering energies. The results of simulations using atomic scattering

amplitudes obtained from the partial wave calculations with the ELSEPA code [36] are presented in Sec. 3.4.3. These calculations indeed show that the fluorine atom contributions are much smaller than indicated by the PWBA model, and lead to a more accurate model of the experiment.

3.4.1 Model summary

In this section a semi-classical (QRT) model is described that will be used to calculate *difference* spectra for aligned and anti-aligned molecules, which can be directly compared to the experimental difference images. In Sec. 2.6 it was shown that using the semi-classical model it is possible to obtain for each re-scattered photoelectron with final momentum $\boldsymbol{p_f}$ the momentum at the time of re-scattering π_r and the angle at which it has scattered from the parent ion. This is done by solving Eqs. (2.142)–(2.145), which describe the classical motion of the re-scattered photoelectron in the strong laser field. The photoelectron re-scattering momentum and angle are subsequently used as an input in the calculation of the electron scattering Differential Cross-Section (DCS). The molecular DCS is calculated using the IAM treated in Sec. 2.5.1, which gives the molecular electron scattering cross-sections as a coherent superposition of scattered wave contributions from each atom separately. As mentioned in Sec. 2.6, for each final momentum $\boldsymbol{p_f}$ there are in fact *two* distinct solutions of the classical equations of motion, which lead to different re-scattering momenta. In the current model the contribution from both solutions is included by using the ADK tunnelling rate, given by (2.135), as a weighting factor when summing the DCSs for each distinct solution in order to obtain the total DCS value. Because the ionization time for one of the contributions is closer to the peak of the laser electric field it was found that this dominates most of the features observed in the simulated difference images.

The final step in the model is the averaging of the molecular DCS over the molecular-frame distribution in the alignment and anti-alignment case, and the construction of the simulated normalized difference images as defined by (3.2).

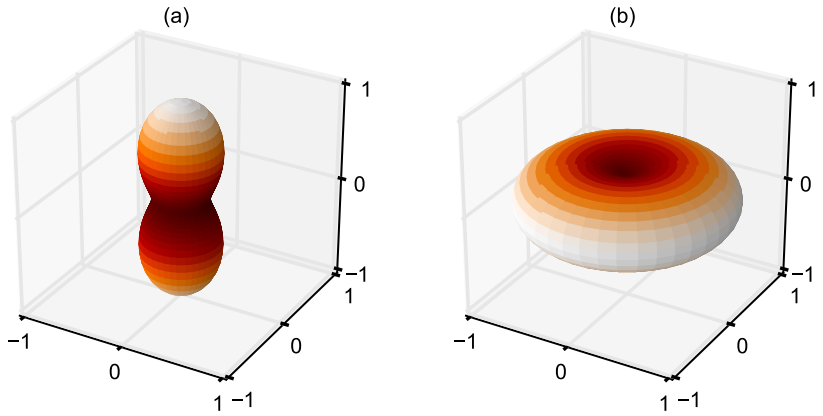

Figure 3.9: An illustration of the molecular-frame distribution given by (3.3) for (a) aligned and (b) anti-aligned molecules.

The alignment distribution is assumed to be given by [99]

$$\rho_{align}(\theta) = \exp\left(-\frac{1}{2}\frac{\sin^2\theta}{\sigma^2}\right) \tag{3.3}$$

where θ is the angle between the C–I axis and the alignment pulse polarization, and σ is the parameter specifying the degree of alignment. The *anti*-alignment distribution are obtained from (3.3) by replacing the $\sin^2\theta$ factor in the exponential by $\cos^2\theta$ [99]. The alignment and anti-alignment distributions obtained from (3.3) are illustrated in Fig. 3.9. The averaging over this distribution is accomplished in the model by uniformly sampling the molecular axis distribution at 4800 different orientations.

3.4.2 Plane Wave Born Approximation scattering

The result of simulations corresponding to the 800 nm probe experimental data from Fig. 3.4 are shown in Fig. 3.10. The simulation in this section uses atomic form factors given as crystallographic reference data [38] for the use in conventional high-energy electron diffraction. These form factors are calculated using the Plane Wave Born Approximation (PWBA) introduced in Sec. 2.4.2. A simulation using the equilibrium geometry of the CF_3I molecule is shown in Fig. 3.10(a). As expected, in the region below $4U_p$ (dashed line) the simulation is qualitatively quite different from the experimental data due to the dominant influence of the direct photoelectrons. For momenta above 1.0 a.u. the simulation becomes *qualitatively* similar to the experimental data, showing a clear maximum around 1.4 a.u. along the polarization axis $p_\parallel$. However, in the experimental data the corresponding maximum is shifted to somewhat higher momenta, which can be clearly seen in the plot of the signal along the $p_\parallel$ axis for the experiment and the full molecule simulation shown in Fig. 3.10(c). Looking at the signal modulation in the *simulation*, it is seen to complete a full oscillation between approximately 0.5 and 1.6 a.u. This modulation period can be explained by the fact that the simulation contains a strong contribution from the I–F scatterer pairs within the molecule. A simple calculation of the oscillation period expected from the diffraction due to the I–F pair gives $2\pi/r_{IF} = 1.15$ a.u., where $r_{IF} = 2.89$ Å. Figure 3.10(b) shows a simulation in which all fluorine atoms are removed from the molecule. The modulation period that is expected from the r_{CI} distance of 2.15 Å is 1.55 a.u. This indeed explains the observed shift of the simulated maximum from 1.4 to more than 1.7 a.u. (blue line) in Fig. 3.10(c). Unfortunately, the C–I only simulation shows a shift of the maximum which is too strong, resulting in significant mismatch with the experimental curve for momenta between 1.1 and 1.5 a.u. In the next section it will be shown that the difference between the experiment and simulation can be explained by a reduced cross-section of the fluorine atoms at low scattering energy, which results in an intermediate shift of the simulation curve.

PWBA-IAM simulations for the 1300 nm probe wavelength experimental data from Fig. 3.5(c) have also been performed and are shown in Fig. 3.11. The full molecule simulation in Fig. 3.11(a) shows a very clear deviation from the experimental data, indicating a local minimum around 1.9 a.u. that is absent from the experiment. The contribution from this minimum could partially be seen in the 800 nm probe simulations, where it was already causing a clear

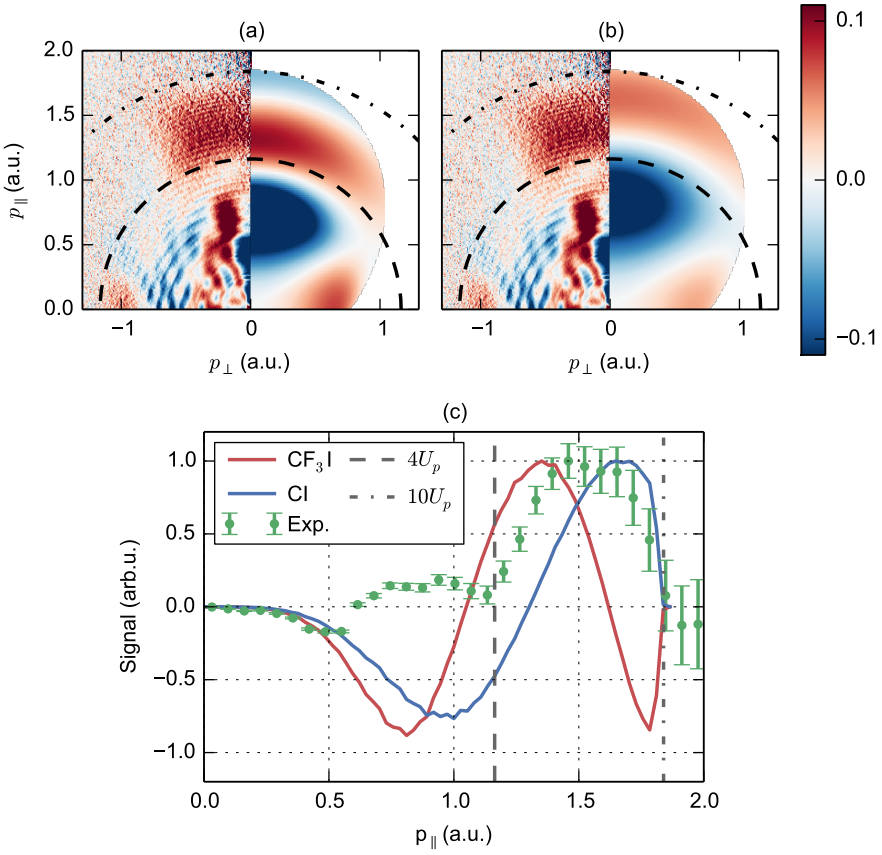

Figure 3.10: Comparison between the experiment at 800 nm probe wavelength with an intensity of $7.5 \pm 0.8 \times 10^{13}\,\mathrm{W/cm^2}$ and the PWBA-IAM model: (a) CF_3I molecule simulation, (b) C–I fragment only simulation, and (c) signal variation along the polarization axis $p_\parallel$ for the experiment (green dots) and the two simulations (red and blue lines, CF_3I and C–I simulations respectively). The experimental normalized difference image, see Fig. 3.4(c), is inverted using the BASEX method [95] and is plotted on the left half of Figs. (a) and (b). The $4U_p$ and $10U_p$ energies are indicated in all figures by the dashed and dash-dotted circles/lines, respectively. The signal variation along the $p_\parallel$ axis is obtained by angular integration of the images over an opening angle of 20°.

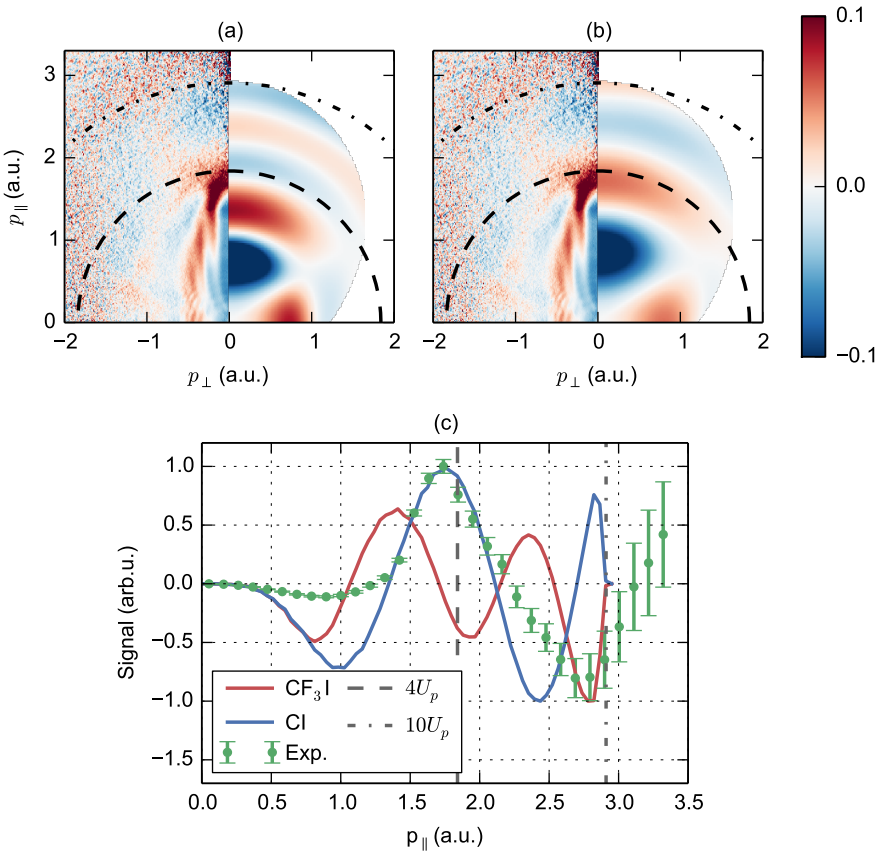

Figure 3.11: Comparison between the experiment at 1300 nm probe wavelength with an intensity of $7.0 \pm 0.6 \times 10^{13}$ W/cm^2 and the PWBA-IAM model. The experimental normalized difference image is from Fig. 3.5(c). See Fig. 3.10 for further plot description.

deviation from the experimental data at momenta above 1.5 a.u. On the other hand, the simulation with the C–I fragment only, shown in Fig. 3.11(b), matches quite well with the experimental data and again indicates that the discrepancy between simulation and experiment is linked to fluorine atom effects.

3.4.3 Partial wave scattering

By looking directly at the effect of the changing molecular frame distribution on the PAD, non-structural effects can be effectively suppressed from the experimental signal. Nevertheless, non-structural effects are not fully eliminated and, as will be shown here, can have an important influence on the features observed in the normalized difference momentum maps. The PWBA atomic form factors used in the simulations in the previous section are based on the perturbative Born approach and are in principle not very suitable for low energy electron scattering, as explained in Sec. 2.3. An inaccuracy in the atomic

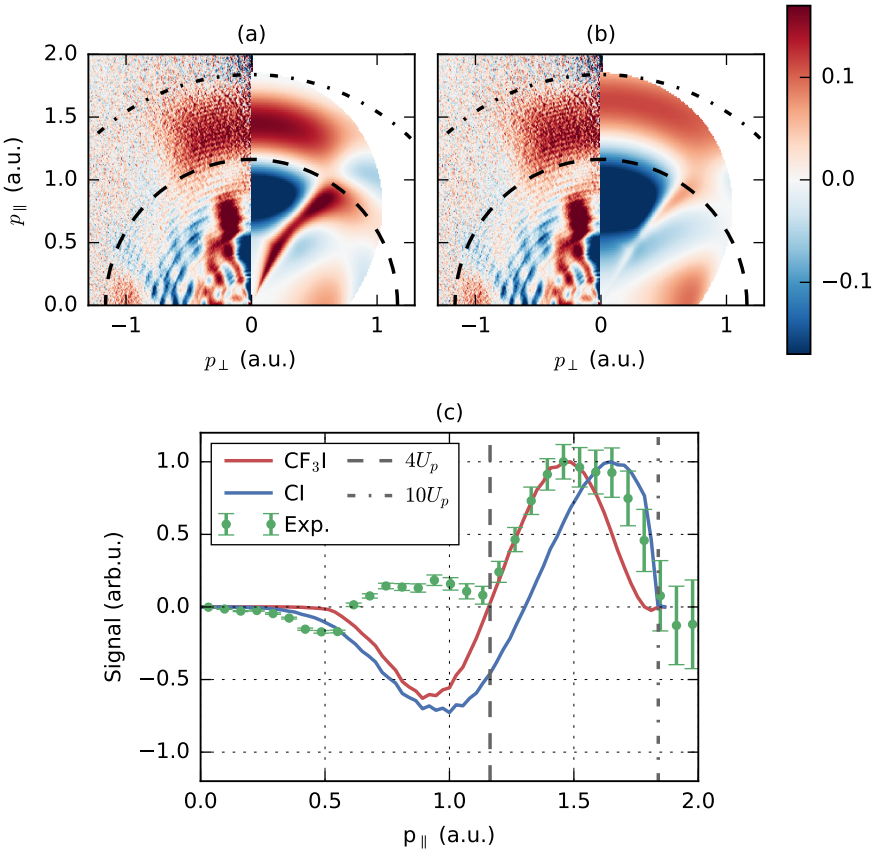

Figure 3.12: Comparison between the experiment at 800 nm probe wavelength with an intensity of $7.5 \pm 0.8 \times 10^{13}$ W/cm^2 and the *ELSEPA-IAM* model: (a) CF_3I molecule simulation, (b) C–I fragment only simulation, and (c) signal variation along the polarization axis $p_\parallel$ for the experiment (green dots) and the two simulations (red and blue lines, CF_3I and C–I simulations respectively). The experimental normalized difference image, i.e. Fig. 3.4(c), is inverted using the BASEX method [95] and plotted on the left half of Figs. (a) and (b). The signal variation along the polarization axis is calculated by integration of the normalized images over an angle of 20°.

form factors may well explain the discrepancy between simulations of the experiment in Figs. 3.10 and 3.11. To explore this possibility, the QRT simulation was performed using scattering amplitudes calculated with the elastic electron-atom scattering code ELSEPA developed by Salvat *et al.* [36]. This software package uses a partial wave expansion to calculate scattering amplitudes in the static-exchange approximation and incorporates approximate exchange and correlation-polarization potentials. The resulting simulations and the comparison with experimental data are shown in Figs. 3.12 and 3.13.

The ELSEPA-IAM simulation for the 800 nm probe wavelength experiment is shown in Fig. 3.12 and indeed shows an improved agreement with the exper-

imental data as compared to the PWBA-IAM simulations. The full molecule simulations show a very good match in the momentum range between 1.1 and 1.5 a.u. in Fig. 3.12(c). The C–I fragment only simulation is very similar to the PWBA simulation and shows a relatively large deviation from the experiment in the lower momentum range. It is interesting that the ELSEPA simulation seems to reproduce some of the *angular* features observed in the experimental difference map, such as the box-like shape of the experimental maximum 1.4 a.u. This is an example where residual non-structural contributions affect the features observed in the normalized difference momentum maps.

The ELSEPA-IAM simulation for the 1300 nm probe wavelength experiment is shown in Fig. 3.13. The full molecule simulation in Fig. 3.13(a) now shows significant deviation from the experimental image in the 4–10U_p energy range . Nevertheless, the deviation from the experiment is much less pronounced than in the full molecule PWBA calculations. At the position of the very strong local minimum in the PWBA calculations around $p_{\parallel}$ =1.9 a.u., the full molecule

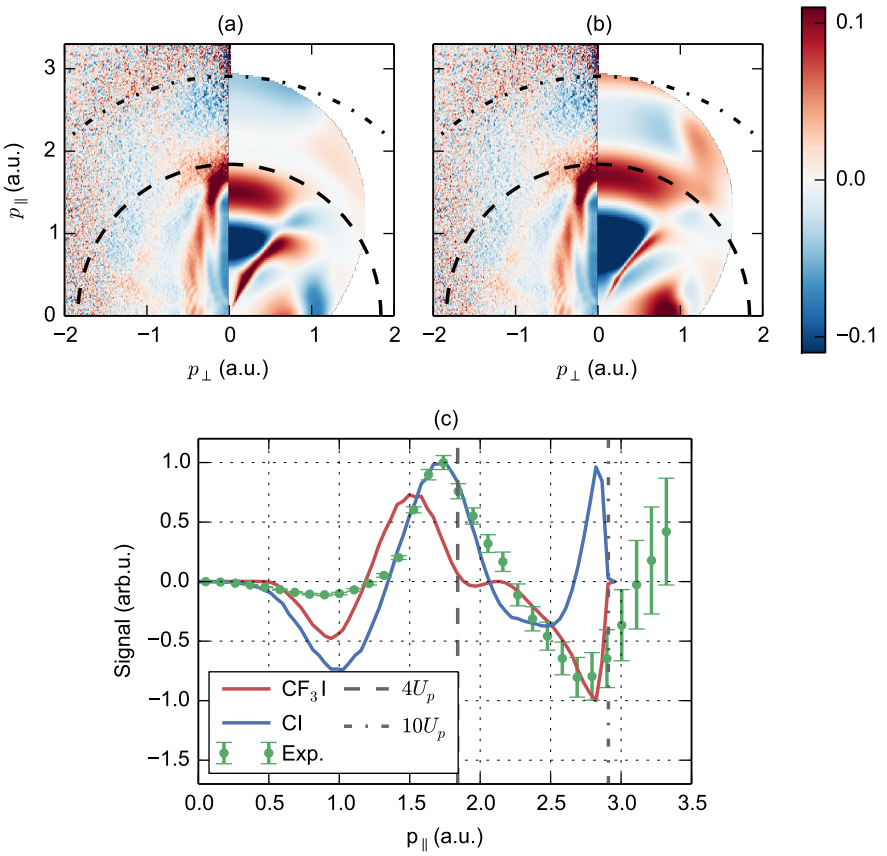

Figure 3.13: Comparison between the experiment at 1300 nm probe wavelength with an intensity of $7.0 \pm 0.6 \times 10^{13}\,\mathrm{W/cm^2}$ and the *ELSEPA-IAM* model. The experimental normalized difference image is from Fig. 3.5(c). See Fig. 3.12 for further plot description.

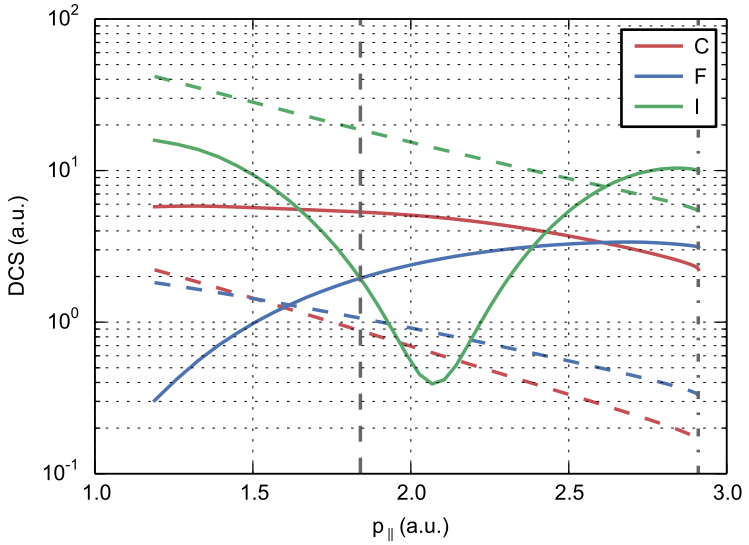

Figure 3.14: ELSEPA (full lines) and PWBA (dashed coloured lines) elastic scattering Differential Cross-Section (DCS) for the C, F and I *atoms* along the polarization axis $p_{\parallel}$ corresponding to the 1300 nm simulation shown in Fig. 3.13(c). The $4U_p$ (dashed grey line) and $10U_p$ (dash-dotted grey line) are also plotted.

ELSEPA simulation indicates a plateau around zero for the momentum range of $p_{\parallel}$ =1.8–2.3 a.u. For higher longitudinal momenta the ELSEPA simulation now shows a minimum that matches well with the experimental data. Again, the fluorine atoms can be removed from the molecule and the results are shown in Figs. 3.13(b) and 3.13(c) (blue line). The simulation with the C–I fragment only shows a better fit with the experiment close to the $4U_p$ energy, where the full molecule simulation shows a plateau that deviates significantly from the experiment. The plateau in the full molecule model is therefore assigned to residual fluorine atom effects.

In order to understand the difference between the PWBA and ELSEPA simulations in more detail it is necessary to look at the behaviour of the *atomic* scattering cross-sections. These are plotted in Fig. 3.14 for the 4–$10U_p$ photoelectron momentum range corresponding to Fig. 3.13(c). The PWBA atomic scattering cross-sections (dashed coloured lines) show a very monotonic decrease and have a similar ratio over the entire range, with the iodine having an approximately ten times larger cross-section than carbon or fluorine. On the other hand, the ELSEPA simulations show a very different picture, where the cross-section ratios are exactly opposite for a rather large range of photoelectron momenta around 2 a.u. This is the region where the I–F related minimum from the 1300 nm PWBA simulations is seen to be suppressed in the ELSEPA-IAM simulation, becoming a plateau rather than a full-fledged minimum. It is therefore concluded that this effect is caused by the reduced magnitudes of the iodine and fluorine cross-sections, which leads to the situation where the molecular structure interference factors for the I–F pairs (see also Sec. 2.5.1) are much less

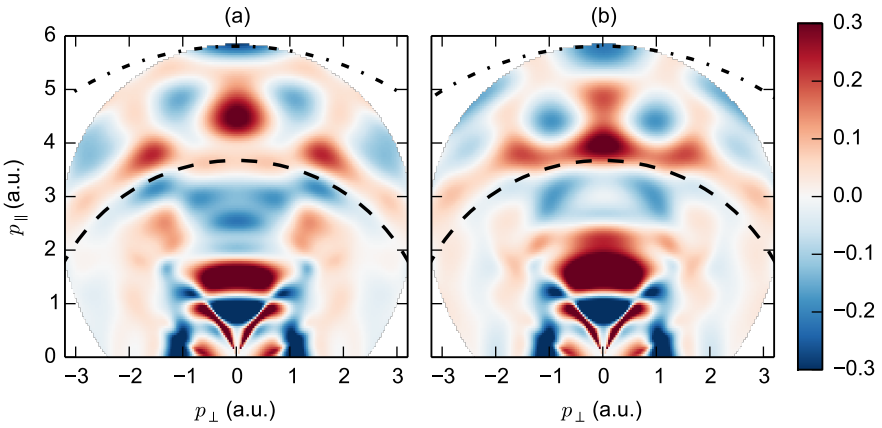

Figure 3.15: Simulated normalized difference maps for experiments with 2300 nm probe wavelength and 9.3×10^{13} W/cm^2 intensity with aligned, $\langle \cos^2 \theta \rangle_{3D} \approx 0.9$, CF_3I molecules: (a) equilibrium molecular geometry and (b) molecular geometry with the angle $\angle ICF$ of 100° instead of the equilibrium value of 110°.

strong with respect to the interference factors containing carbon. The difference between the 800 nm PWBA and ELSEPA simulations are similarly explained by the reduced magnitude of the cross-section of the fluorine atom as compared to the carbon.

In conclusion, comparison with experimental results indicates that the ELSEPA-IAM model is a step in the right direction in interpreting the experimental data. To improve the match with experiment, a more sophisticated model is required which should go beyond the IAM. This may for example be accomplished by using the EPolyScat package to compute low energy electron scattering cross-sections for the molecular ion as a whole [35]. Another source of inaccuracy is the QRT approach which uses a classical photoelectron propagation model. More accurately modelling the strong field process, and including direct photoelectrons and their interference with the re-scattered photoelectrons, is expected to significantly improve the simulations in the regions below the $4U_p$ threshold.

Before continuing with strong field theory calculations, it is interesting to discuss in a more general way how molecular structure manifests itself in normalized difference maps and use the current model to simulate possible future experiments with highly aligned molecules. All the simulations presented so far have one striking feature in common, which is the manifestation of structural effects as oscillations in the difference image along the polarization axis $p_\parallel$. From the classical picture of photoelectron re-scattering illustrated in Fig. 2.20 it can be seen that the photoelectrons on this axis have been scattered by a fixed angle of 180° and have a varying re-scattering *energy*, i.e. de Broglie wavelength. Of course, using full momentum map detectors, such as the VMIS, one simultaneously obtains the angular *and* energy distribution of the photoelectrons gaining access to even more information. In the current experiment, molecular structure effects were strongest along a single scattering angle. However, it is expected that future experiments with a high degree of molecular alignment and high

re-collision energy will benefit greatly from the availability of the full momentum distribution. This is illustrated in Fig. 3.15, which simulates an experiment using a probe with a 2300 nm wavelength and a $9.3 \times 10^{13}\,\mathrm{W/cm^2}$ intensity on aligned CF_3I molecules with a degree of alignment of $\langle \cos^2\theta \rangle_{2D}$=0.94. Due to the long probe wavelength, the photoelectron re-collision energy in this simulation is up to 145 eV, which is much larger than the maximum re-collision energy of 35 eV that was reached in the 1300 nm experiment at $7.0 \pm 0.6 \times 10^{13}\,\mathrm{W/cm^2}$ presented above. The normalized difference map for the molecules at equilibrium geometry (a) and for molecules with a slightly smaller angle $\angle ICF$ (b) changes in a significant way in the radial as well as the angular direction. Using all the information contained in the full momentum distribution, it would be possible to perform a 3-D reconstruction of a relatively complex molecule in a similar fashion as recently demonstrated in Ultrafast Electron Diffraction experiments on aligned molecules [23, 24].

3.5 Molecular Strong Field Theory

A more accurate model of the strong field process that drives LIED and which goes beyond the semi-classical QRT model is required in order to understand the photoelectron spectrum in the region below the $4U_p$ threshold. In this region, the experimental normalized difference images reveal a particularly rich pattern of features. Factors such as molecular orbital shape [68] and photoelectron holographic interference [98], which is due to the interference between the direct and the re-scattered photoelectrons, may significantly contribute to the observed modulations in this energy range. This section will present some first results of Molecular Strong Field Theory (MSFT) simulations of the current LIED experiments on aligned CF_3I molecules. The MSFT used in these calculations was initially developed by Milošević *et al.* for the case of diatomic molecules [88, 89] and was recently generalized to poly-atomic molecules by Hasović *et al.* [90, 91]. A short and general introduction to the theory will be given first in Sec. 3.5.1 in order to establish the main features and approximations of the theory. The interested reader is referred to the original works for a detailed exposition of the theoretical method [88, 89, 90, 91]. Numerical results and the comparison with experiments are presented in Sec. 3.5.2.

3.5.1 Theory summary

The simple semi-classical model that was introduced in Sec. 2.6 and used in the previous section follows from the more general Strong Field Theory (SFT). At the foundation of Strong Field Theory (SFT) is the process of *Hamiltonian partitioning*. Hamiltonian partitioning is well-known from conventional perturbation theory where the full system Hamiltonian can be divided in two terms: a dominant reference term, which is often exactly solvable, and a small perturbation term, see e.g. [30, 26, 28]. The crucial difference between conventional perturbation theory and the SFT is the application of *different* Hamiltonian partitioning schemes for the initial, intermediate and final states, such that the SFT perturbation series includes the relevant interactions in its *leading* terms [66]. The interested reader is referred to Appendix A for a summary of the Intense-field Many-body S-matrix Theory (IMST), which provides a consistent

and powerful formulation of the SFT based on a *formalized* process of Hamiltonian partitioning, for a more in-depth discussion of this topic.

To represent the process of the ionization of an electron by a strong laser field, which includes the re-scattering with the remaining ionic core as an intermediate step, it is necessary to adopt *three* Hamiltonian partitioning schemes. In the initial partitioning scheme the field-free target Hamiltonian H_T, which corresponds to an electron bound by the ionic core, is taken as the reference and the laser field V_L as the perturbation. In the intermediate *and* final partitioning schemes the laser-electron Hamiltonian H_L, which corresponds to a single electron in a classical laser field, is taken as the reference, and the field-free target Hamiltonian V_T, i.e. the ionic core potential, is taken as the perturbation. Using the IMST approach it is possible to obtain an expression for the *evolution operator* of the photoelectron. An evolution operator describes the temporal behaviour of a system and is defined as follows

$$|\psi(t)\rangle = U(t,t')\,|\psi(t')\rangle \tag{3.4}$$

That is, the electronic wavefunction at time t is given by the application of the evolution operator on the wavefunction at time t', which may be specified as an initial condition. The IMST evolution operator for the ionization of an electron by a strong laser field that includes re-scattering with the ionic core is given by

$$\begin{aligned} U(t,t') = U_i(t,t') &- \frac{\mathrm{i}}{\hbar}\int_{t'}^{t} U_L(t,\tau_0)V_L(\tau_0)U_T(\tau_0,t')\,\mathrm{d}\tau_0 \\ &- \left(\frac{\mathrm{i}}{\hbar}\right)^2 \int_{t'}^{t}\int_{\tau_0}^{t} U_L(t,\tau_1)V_T(\tau_1)U_L(\tau_1,\tau_0)V_L(\tau_0)U_T(\tau_0,t')\,\mathrm{d}\tau_0\,\mathrm{d}\tau_1 \\ &- \left(\frac{\mathrm{i}}{\hbar}\right)^3 \int_{t'}^{t}\int_{\tau_0}^{t}\int_{\tau_0}^{\tau_1} U_L(t,\tau_2)V_T(\tau_2)U(\tau_2,\tau_1)V_T(\tau_1)U_L(\tau_1,\tau_0) \\ &\qquad \times V_L(\tau_0)U_T(\tau_0,t')\,\mathrm{d}\tau_0\,\mathrm{d}\tau_1\,\mathrm{d}\tau_2 \end{aligned} \tag{3.5}$$

where U_T and U_L are the evolution operators corresponding to the field-free target and the laser-electron Hamiltonians, H_T and H_L, respectively.

The first term in the IMST expression of the full evolution operator (3.5) is simply the evolution operator of the initial electronic (target) state and represents the part of the system that is not affected by the laser. The second term in this equation represents a transition at time τ_0 from the initial target state, through an interaction with the laser field perturbation V_L, to a final continuum state governed by the laser-electron Hamiltonian H_L. This term describes the *direct photoelectrons* that do not interact with the ionic core after being ionized. In the third term, the initial state interacts with the laser at time τ_0, leading to a transition to an *intermediate* continuum state governed by H_L. The intermediate state evolves freely from τ_0 to τ_1, at which time a transition takes place from the intermediate to the *final* continuum state through an interaction with the perturbation V_T, i.e. the ionic core. After the re-scattering interaction at τ_1, the final state evolves freely again according to U_L. The third term represents the *re-scattered photoelectrons* and leads to a description of the LIED effect in molecules. The final term in (3.5) represents all higher order processes, which includes, for example, further interactions of the photoelectron with the

parent ion. The evolution operator given by the integral equation (3.5) is an exact solution of the Time-Dependent Schrödinger Equation describing the system consisting of a single active (photo)electron, the ionic core potential and the strong laser field. An approximate solution for the evolution operator is readily obtained by neglecting the last term in (3.5), which leads to the *second order* Strong Field Approximation (SFA2) [64, 65]. The Molecular Strong Field Theory (MSFT) is a SFA2 theory applied to the case of molecules.

Having established the broader theoretical context in which the MSFT can be placed, the concrete form of the calculations will be roughly outlined. The initial state of the molecular system is assumed to be a single orbital, i.e. the Highest Occupied Molecular Orbital (HOMO), and is modelled by a Linear Combination of Atomic Orbitals (LCAO) centred on each atom within the molecule. The molecular wavefunction is expressed as the sum

$$\psi_i(\boldsymbol{r}) = \sum_{j=1}^{N} \sum_{k} c_{jk} \phi_k(\boldsymbol{r} - \boldsymbol{R_j}) \tag{3.6}$$

where j runs over the N atoms within the molecule centred at $\boldsymbol{R_j}$, and k runs over the set of atomic orbitals ϕ_k with LCAO coefficients c_{jk}. The transition of the active electron from the HOMO into a continuum state takes place through the dipole operator so that

$$V_L(t) = \boldsymbol{E}(t) \cdot \boldsymbol{r} \tag{3.7}$$

In the intermediate state, the ionized photoelectron is assumed to be solely driven by the strong laser field. It is therefore represented by the non-relativistic solution to the Schrödinger equation for an electron in a classical electro-magnetic field, i.e. the Volkov wavefunction. In the length gauge and dipole approximation this is given by

$$\chi(\boldsymbol{r}, t) = \exp\left[\mathrm{i}\boldsymbol{\pi}(t) \cdot \boldsymbol{r} - \frac{1}{2}\int^{t} \boldsymbol{\pi}(\tau)^2 \,\mathrm{d}\tau\right] \tag{3.8}$$

where $\boldsymbol{\pi}(t) = \boldsymbol{p} + \boldsymbol{A}(t)$ is the *kinetic momentum* of the electron in the field and $\boldsymbol{p}$ is the *canonical momentum*, which is a constant of the motion. The vector potential $\boldsymbol{A}(t)$ is, in the dipole approximation, given by

$$\boldsymbol{A}(t) = -\int^{t} \boldsymbol{E}(\tau) \,\mathrm{d}\tau \tag{3.9}$$

where $\boldsymbol{E}(t)$ is the electric field component of the laser. From (3.8) it can be seen that the Volkov wavefunctions are *plane waves* with an instantaneous, time-dependent momentum $\boldsymbol{\pi}(t)$ and a *phase factor*. The Volkov phase is accumulated during the laser driven motion of the electron and is given by an integral over its instantaneous value of kinetic energy $\frac{1}{2}\boldsymbol{\pi}(t)^2$. Using the explicit form of the Volkov wavefunction (3.8), the Volkov *evolution operator* is given in its *spectral representation* by

$$U_L(t, t') = \int |\chi_{\boldsymbol{p}}(t)\rangle \langle \chi_{\boldsymbol{p}}(t')| \,\mathrm{d}\boldsymbol{p} \tag{3.10}$$

Substituting (3.6), (3.7) and (3.10) into (3.5), and neglecting the final term in accordance with the SFA2, gives the expression for the photoelectron wavefunction in the MSFT. To obtain the *transition amplitude* from the initial molecular

state into a final Volkov state with canonical momentum $\boldsymbol{p_f}$, the full wavefunction must be projected onto $\left|\chi_{\boldsymbol{p_f}}(t)\right\rangle$ which finally results in the basic MSFT expression

$$T_{fi} = -\frac{\mathrm{i}}{\hbar}\int_{t'}^{t} \left\langle \chi_{\boldsymbol{p_f}}(\tau_0)\right| \boldsymbol{E}(\tau_0)\cdot\boldsymbol{r}\left|\psi_i(\tau_0)\right\rangle \mathrm{d}\tau_0 \\ - \left(\frac{\mathrm{i}}{\hbar}\right)^2 \int_{t'}^{t}\int_{\tau_0}^{t}\int \left\langle \chi_{\boldsymbol{p_f}}(\tau_1)\right| V_T(\tau_1)\left|\chi_{\boldsymbol{p_m}}(\tau_1)\right\rangle \\ \times \left\langle \chi_{\boldsymbol{p_m}}(\tau_0)\right| \boldsymbol{E}(\tau_0)\cdot\boldsymbol{r}\left|\psi_i(\tau_0)\right\rangle \,\mathrm{d}\tau_0\,\mathrm{d}\tau_1\,\mathrm{d}\boldsymbol{p_m} \quad (3.11)$$

The first term in (3.11) represents *direct photoelectrons* which do not interact with the ionic core after ionization and is a generalization of Keldysh's SFA to molecules[5]. The atomic orbitals ϕ_k are modelled using a Gaussian basis set so that the dipole transition matrix elements $\langle\chi_{\boldsymbol{p}}(\tau_0)|\,\boldsymbol{E}(\tau_0)\cdot\boldsymbol{r}\,|\psi_i(\tau_0)\rangle$ can be calculated analytically [90]. The second term in (3.11) represents *re-scattered photoelectrons* which are ionized into an intermediate Volkov state with canonical momentum $\boldsymbol{p_m}$ before scattering off the static potential of the molecular ion V_T and ending up in the final Volkov state $\boldsymbol{p_f}$. At the moment of re-scattering τ_1, the Volkov wavefunctions are plane waves with momentum $\boldsymbol{\pi}(\tau_1)$. Consequently, scattering of the intermediate Volkov state from the target molecule and the transition into the final Volkov state described by the matrix element $\left\langle \chi_{\boldsymbol{p_f}}(\tau_1)\right| V_T(\tau_1)\left|\chi_{\boldsymbol{p_m}}(\tau_1)\right\rangle$ is equivalent to the Plane Wave Born Approximation (PWBA). The PWBA was introduced in Chapter 2 and was also used in the semi-classical LIED model presented in Sec. 3.4.2. The molecular re-scattering matrix element is calculated in the MSFT code using parametrized analytical model potentials for each atom, in combination with the IAM [101, 102]. The integration over τ_0 and τ_1 is performed numerically, while the integration over $\boldsymbol{p_m}$ is performed using the saddle-point approximation [90, 91]. Similarly to the semi-classical models presented in the previous section, the final step in the calculation is the averaging of the PAD over the molecular axis distribution in the alignment and anti-alignment case, and the construction of the simulated normalized difference images. The averaging over this distribution is accomplished by uniformly sampling the molecular axis distribution at 300 different orientations.

3.5.2 Calculation results

The comparison between the MSFT simulation and experimental PADs for three different intensities is shown in Fig. 3.16. The simulated PADs show a pronounced positive lobe in a large part of the spectrum. However, this feature does not match any of the maxima observed in the experimental spectra. It shows a certain similarity in shape with a strong positive feature in the experimental images that is located within the $4U_p$ circle in the momentum range $p_\parallel$=0–0.8 and $p_\perp$=0–0.4 a.u. However the simulated peak is located at much higher longitudinal and transverse momenta for all three probe intensities. At

[5]The straight-forward application of atomic SFA to molecules leads to the appearance of spurious phase factors from the application of the dipole operator on the spatially displaced atomic centres within the molecule [100]. This difficulty is addressed by MSFT through the use of a *dressed* molecular state (see [88] for details).

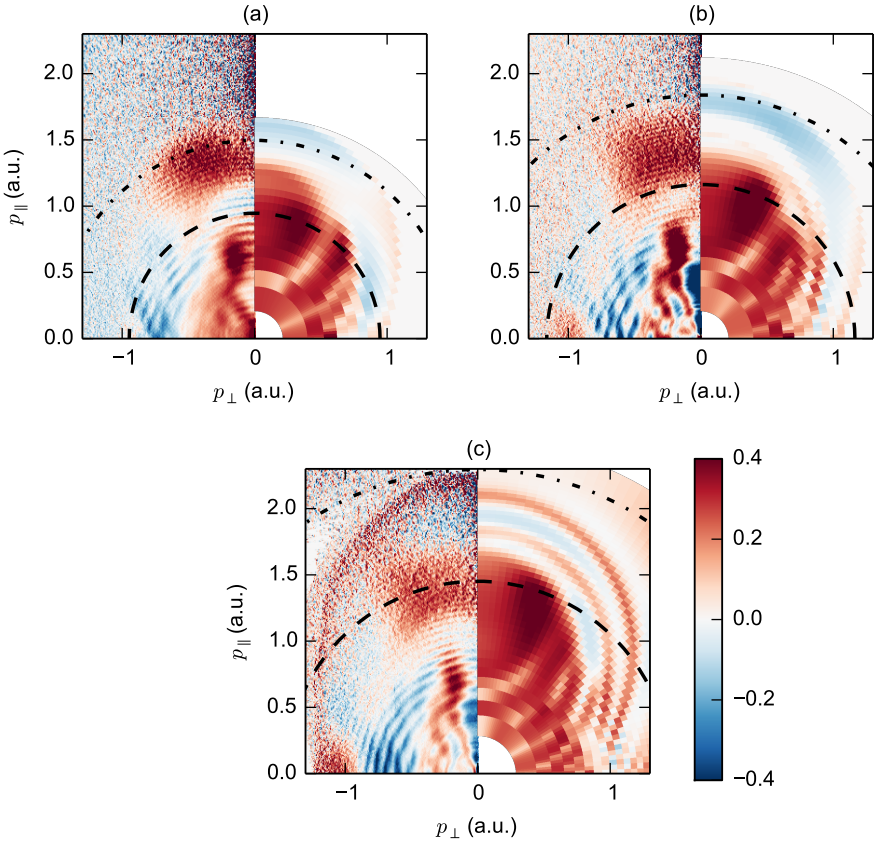

Figure 3.16: Comparison between the experiment at 800 nm probe wavelength (left half) and the MSFT simulation (right half) for three simulated probe intensities: (a) $5.1 \times 10^{13}\,\mathrm{W/cm^2}$, (b) $7.7 \times 10^{13}\,\mathrm{W/cm^2}$ and $1.2 \times 10^{14}\,\mathrm{W/cm^2}$. Each simulation is compared to the experiment with the closest probe intensity, which are (a) $3.7 \pm 0.4 \times 10^{13}$, (b) $7.5 \pm 0.8 \times 10^{13}$ and (c) $9.6 \pm 1.1 \times 10^{13}\,\mathrm{W/cm^2}$. The $4U_p$ (dashed) and $10U_p$ (dash-dotted) isoenergy circles for the simulated probe intensity are indicated.

the same time, the positive feature with longitudinal momentum between 1.1 and 1.8 a.u. in the experimental spectra, that was identified as a diffraction feature by the semi-classical models, is at much higher momenta than the positive feature in the simulations. Finally, the experimental image in Fig. 3.16(c) clearly indicates a negative feature along the polarization axis for momenta above 1.8 a.u. At the position of this minimum in the experimental image, the simulation shows a strongly oscillatory feature instead.

A comparison of the signal variation in the experiment and simulation along the polarization axis is plotted in Fig. 3.17. The *experimental* peak located between 1.1 and 1.8 a.u. is very robust against changes to the the probe intensity. The rising edge of this peak is seen to remain at virtually the same position for all three probe intensities. The falling edge of this peak is also at an almost

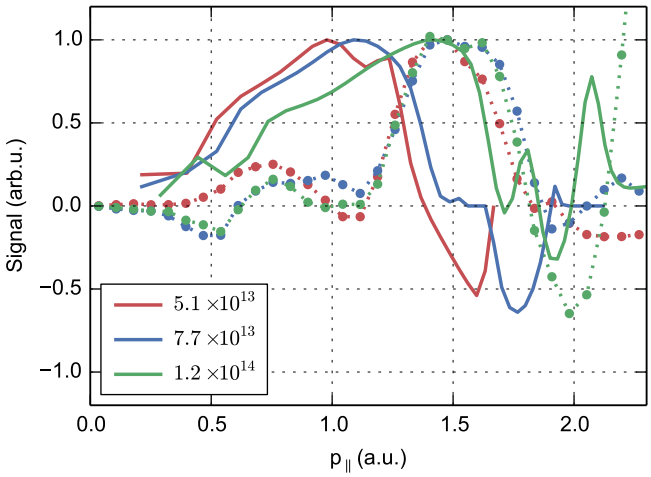

Figure 3.17: Signal variation along the polarization axis for the three experimental (dots, connected by dotted lines as guide to the eye) and simulated (solid lines) PADs shown in Fig. 3.16.

identical position for the two highest probe intensity experiments (green and blue dots). This behaviour is consistent with the idea that diffraction peaks are a molecular structure feature that should not be affected strongly by the intensity of the probing laser field. In the lowest probe intensity experiment (red dots), the falling edge is seen to be shifted to lower momenta with respect to the higher intensity experiments. However, it can be seen in Fig. 3.16(a) that the $10U_p$ cut-off in this experiment is below the position of the falling edge observed in the higher probe intensity experiments. This indicates that the observed position of the falling edge in the lowest probe intensity experiment is determined by the photoelectron cut-off, rather than by diffraction effects. The position of the positive peak in the *simulations* shows a pronounced dependence on the probe intensity, as can be seen from the plots in Fig. 3.17 (solid lines). Such a strong probe intensity dependence suggests that the simulated maximum may not be attributed to LIED effects, which are expected to be relatively robust against changes in the probe intensity.

The MSFT simulation has also been performed for the experiment at 1300 nm probe wavelength and is shown in Fig. 3.18. The simulation again indicates a pronounced positive lobe, which now coincides with the experimental maximum along the polarization axis at 1.7 a.u. However, the experimental *minimum* at higher momenta is not reproduced by the simulation. The simulation shows a strong oscillatory feature similar to that observed in the 800 nm wavelength simulation in Fig. 3.16(c). In order to check whether the positive lobe in the simulated PAD may be linked to molecular structure, MSFT simulations of the photoelectron spectrum along the polarization axis were performed at two additional probe intensities. The result is shown in Fig. 3.19. The experimental maximum (blue dots) and the simulated maximum (blue solid line) coincide at $8.7 \times 10^{13}\,\mathrm{W/cm^2}$ probe intensity. For a somewhat lower intensity of $6.3 \times 10^{13}\,\mathrm{W/cm^2}$ (red solid line) and a higher intensity of $1.2 \times 10^{14}\,\mathrm{W/cm^2}$

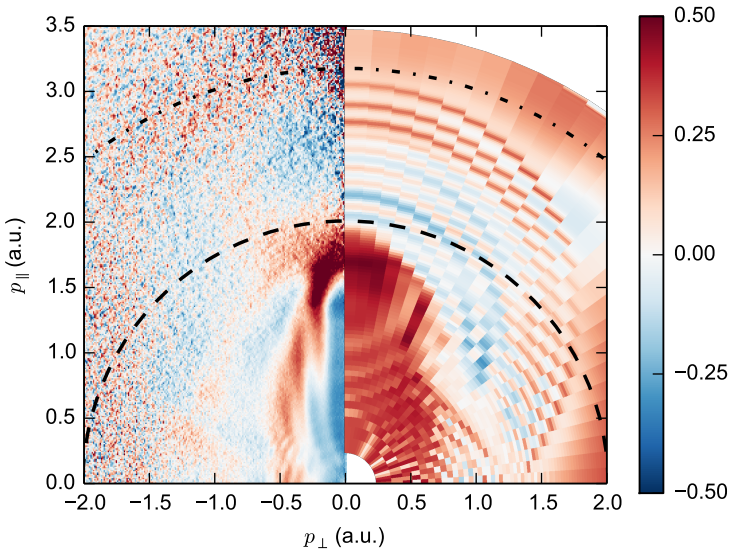

Figure 3.18: Comparison between the experiment at 1300 nm probe wavelength and $7.0 \pm 0.6 \times 10^{13}\,\mathrm{W/cm^2}$ intensity (left half) and the MSFT simulation at $8.7 \times 10^{13}\,\mathrm{W/cm^2}$ (right half). The $4U_p$ (dashed) and $10U_p$ (dash-dotted) iso-energy circles are also indicated.

(green solid line), the simulated maximum shifts by a significant amount. All three simulated curves also show strong oscillatory behaviour at high momenta and do not show a clear minimum, as is present in the experiment.

Neither the pronounced intensity dependence nor the strong oscillatory behaviour of the simulation are at the moment understood. One possible cause for the lack of diffraction information in the simulated spectra is the fact that the electron scattering process is not necessarily elastic in the current MSFT model [103, 104]. That is, when evaluating the scattering matrix element $\langle \chi_{\boldsymbol{p_f}}(\tau_1) | V_T(\tau_1) | \chi_{\boldsymbol{p_m}}(\tau_1) \rangle$ in (3.11), the magnitude of the kinetic momentum in the intermediate and final state at the time of re-scattering τ_1, i.e. $\pi_m = |\boldsymbol{p_m} + \boldsymbol{A}(\tau_1)|$ and $\pi_f = |\boldsymbol{p_f} + \boldsymbol{A}(\tau_1)|$, are not necessarily equal. This means that photoelectrons with a range of intermediate state momenta can contribute to a single final state with the canonical momentum $\boldsymbol{p_f}$. This can affect the visibility of diffraction features because they depend on the value of the momentum transfer (see Sec. 2.5.1) that is given by $\boldsymbol{\pi_f} - \boldsymbol{\pi_m}$. Implementing the MSFT model such that the integral over the re-scattering time τ_1 is performed using the saddle-point approximation would effectively enforce the elastic scattering condition.

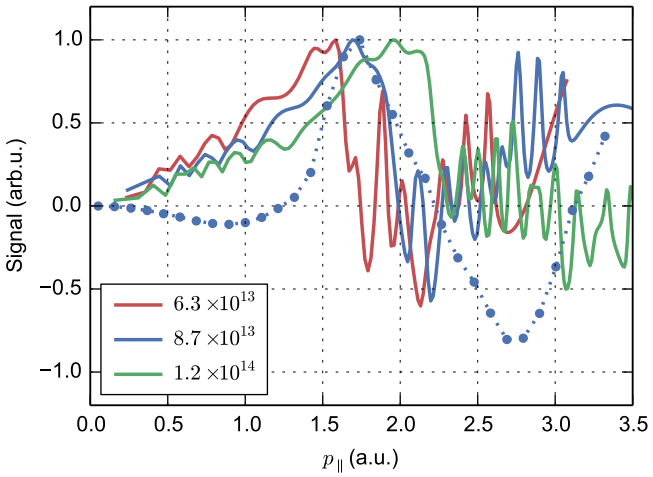

Figure 3.19: Signal variation along the polarization axis for the experimental PAD at 1300 nm probe wavelength and $7.0 \pm 0.6 \times 10^{13}\,\mathrm{W/cm^2}$ intensity (blue dots, connected by dotted lines as guide to the eye) and MSFT simulations (solid lines) at 1300 nm probe wavelength and three different probe intensities.

3.6 Time-Dependent Density Functional Theory

The first experiment demonstrating the LIED technique showed that the shape of the molecular orbital had a distinct influence on the normalized difference between PADs of aligned and anti-aligned molecules in the energy range where direct photoelectrons are dominant [68]. In more recent experiments, Pullen *et al.* [79] suggested that photoelectrons resulting from processes that do not lead to the creation of a ground state molecular ion, e.g. ionization from lower lying molecular orbitals, would result in experimental background masking the LIED effect. To investigate the role of multiple electronic ionization channels in the current LIED experiments on aligned CF_3I molecules, ab-initio calculations based on the Time-Dependent Density Functional Theory code developed by DeGiovannini *et al.* [87] have been performed. The first attempts at these calculations had limited success due to the large amount of computing resources required to obtain numerically converged simulation results. The TDDFT code of DeGiovannini *et al.* was very recently improved so that the photoelectron momentum distributions can be obtained using the time-dependent surface flux method (t-SURFF) [105], which enabled a significant reduction in the required simulation resources. This section will present some first simulation results obtained with the improved TDDFT code.

The dynamics of the photoelectrons originating from the ten Highest Occupied Molecular Orbitals (HOMOs) of CF_3I were simulated. The two highest orbitals, i.e. HOMO and HOMO-1, were found to contribute significantly to the simulated normalized difference images. The TDDFT calculation yields a 3-D PAD for a fixed orientation of the molecule with respect to the alignment pulse polarization. The averaging over the molecular frame distribution for aligned and anti-aligned molecules is done using the same distributions as in the semi-

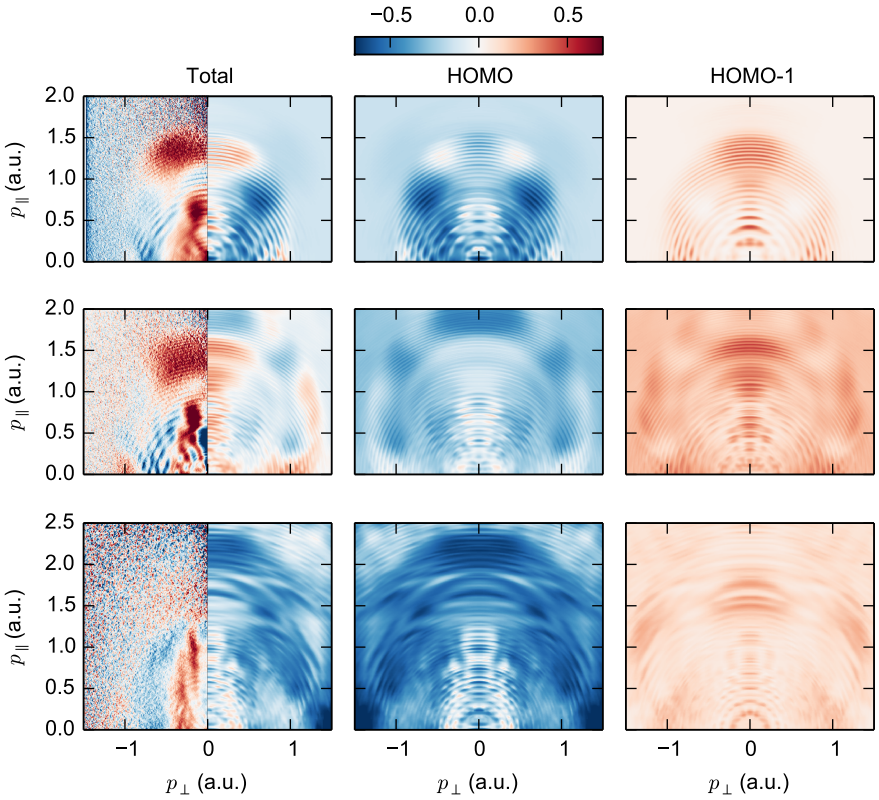

Figure 3.20: TDDFT simulation results for three different combinations of probe pulse intensity and wavelength: (top row) I=3.4 × 10^{13} W/cm^2 and λ=800 nm, (middle row) I=7.7 × 10^{13} W/cm^2 and λ=800 nm, and (bottom row) I= 4.7 × 10^{13} W/cm^2 and λ=1300 nm. The experimental images with the corresponding probe pulse properties are plotted on the left half of the figures in the first column. The second and third columns show the individual contributions from the HOMO and HOMO-1 orbitals to the total simulated image that is plotted on the right half of the figures in the first column.

classical model (see Fig. 3.9). The averaging is accomplished by performing the TDDFT calculation for three different angles between the C–I axis and the alignment pulse polarization, and constructing a weighted average of the simulated PADs using the molecular-frame distribution given by (3.3). The 3-D PADs are then rotationally averaged around the alignment pulse polarization axis, as the molecule can rotate freely around this axis. Finally, the normalized difference images are constructed from the simulated PADs of the aligned and anti-aligned molecules.

The results of the TDDFT simulations for three different combinations of probe pulse intensity and wavelength, which correspond to the experimentally available data, are shown in Fig. 3.20. The contributions of the HOMO *and* the HOMO-1 were found to significantly contribute to the observable features in the total normalized difference images and are shown in the middle and right

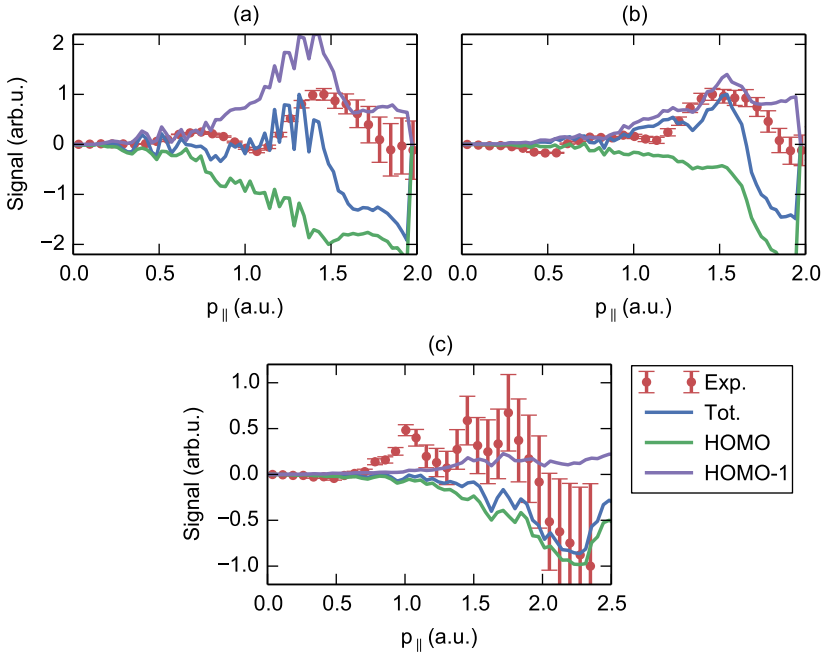

Figure 3.21: Signal variation along the polarization axis for the three TDDFT simulations (solid lines) shown in Fig. 3.20 with a probe pulse intensity and wavelength of: (a) I=3.4 × 10^{13} W/cm^2 and λ=800 nm, (b) I=7.7 × 10^{13} W/cm^2 and λ=800 nm, and (c) I= 4.7 × 10^{13} W/cm^2 and λ=1300 nm. The experimental signal variation corresponding to the experimental images plotted on the left half of the plots in the first column of Fig. 3.20 are also plotted (red dots with errorbars).

columns in Fig. 3.20. It is striking that the HOMO contribution is almost entirely negative in value for all three experimental conditions, whereas the HOMO-1 contribution is almost exclusively positive. This may be understood by the fact that the HOMO orbital has a nodal plane that is parallel to the C–I axis, so that the tunnelling ionization from this orbital is suppressed when the molecules are aligned, and enhanced when they are anti-aligned. The HOMO-1 on the other hand has a nodal plane perpendicular to the C–I axis, which leads to the opposite behaviour.

The features that were assigned to LIED effects using the semi-classical models can also be identified in the TDDFT simulations. In the total normalized difference images for the two simulations using an 800 nm probe wavelength (top and center left plots in Fig. 3.20) there is a positive feature along the polarization axis for longitudinal momenta $p_{\parallel} > 1.1$ a.u. This can also be seen in Fig. 3.21, which shows the signal variation along the $p_{\parallel}$ axis for the simulated and experimental normalized difference images corresponding to the three cases shown in Fig. 3.20. This positive feature is attributed to LIED effects by the semi-classical model calculations that were shown in Sec. 3.4. Looking at the individual contributions of the HOMO and the HOMO-1 to the total normalized

difference image, it is observed that this positive feature is mainly due to a strong contribution from the HOMO-1. In the total normalized difference image for the simulation using a 1300 nm probe wavelength (bottom left plot in Fig. 3.20) there is no clear positive contribution. This disagrees somewhat with the experiment, which does show a weak positive feature for longitudinal momenta of $p_{\parallel}$ =1.4–1.9 a.u., see also Fig. 3.21(c). However, there is a rather strong negative feature in the simulated image for $p_{\parallel} > 1.9$ a.u. that does match well with the experiment. This negative feature is attributed to LIED effects by the semi-classical model. Looking at the individual orbital contributions for this simulation it is observed that the negative feature is mainly due to a strong contribution from the HOMO.

It is concluded that though the TDDFT simulations show a certain similarity to the semi-classical model results, they also clearly illustrate the limitations of the semi-classical model and the importance of molecular orbital effects in the experiments. It is expected that the TDDFT calculations will be used in conjunction with the current experimental results to improve on our understanding of strong-field ionization processes in molecules, and develop extended semi-classical LIED models that can accurately represent molecular orbital effects and multiple ionization channels.

3.7 Conclusion

The experiments presented here demonstrate a very powerful combination: Laser Induced Electron Diffraction (LIED) and molecular alignment. It was shown that even for a relatively complex molecule such as CF_3I and for low photoelectron re-collision energies, it is possible to extract structural information from complex photoelectron spectra resulting from the ionization in a strong laser field. Molecular alignment is an essential ingredient as it enables the effective extraction of diffractions effects, which would have been very challenging otherwise.

A semi-classical model, in which the strong field motion of the photoelectron is treated classically and re-scattering and diffraction off the molecule is modelled quantum mechanically, reproduces experimental features in the high energy range of the spectrum. It was shown that oscillations along the polarization axis in the experimental PADs, can be interpreted as diffraction features. Scattering of the photoelectron with the molecule was modelled using the Independent Atom Model (IAM), with atomic elastic scattering cross-sections obtained by two different methods. Plane Wave Born Approximation (PWBA) atomic cross-sections showed significant deviations from the experimental data. More accurate atomic cross-sections, obtained using the ELSEPA package [36], lead to an improved match with the experiment and provided an explanation for the deviations seen with the PWBA model. It is expected that the use of better electron-molecule scattering cross-sections will further improve the accuracy of the semi-classical model.

In order to understand the photoelectron spectrum in the region close to or below the $4U_p$ cut-off energy, an accurate model of the *strong field* process going beyond the semi-classical approach is required. In this region, the experimental normalized difference images reveal a particularly rich pattern of features which may be linked to effects such as molecular orbital imprinting [68] and

photoelectron holographic interference [98]. The first simulations of the current LIED experiments on CF_3I molecules using the Molecular Strong Field Theory (MSFT) developed by Milošević *et al.* [88, 89, 90, 91] were presented. The simulated spectra show important deviations from the experimental data and the semi-classical models, so that it is currently not possible to compare the results. Nevertheless, the MSFT remains an attractive possibility to model and *interpret* strong field related features and influences in these photoelectron spectra.

The results from ab-initio Time-Dependent Density Functional Theory (TDDFT) calculations performed by DeGiovannini *et al.* are promising and show a relatively good match with the experimental data at all photoelectron energies. The TDDFT calculations indicate that the contribution of not only the Highest Occupied Molecular Orbital (HOMO) but also of the lower lying HOMO-1 are significant and can be identified in the experimental results. This clearly illustrates the importance of molecular orbital effects in these experiments and is expected to lead to the development of extended semi-classical LIED models that can accurately represent molecular orbital effects and multiple ionization channels.

Future experiments combining alignment and the imaging of ultrafast structural dynamics of molecules during photoinduced reactions (e.g. dissociation) are being pursued. Introducing molecular *orientation* as well as improving the degree of alignment may lead to a powerful technique capable of full 3-D reconstruction of molecules undergoing ultrafast motion on their natural time and space scales.

Chapter 4

Velocity map imaging of electron impact ionization – search for coherent emission

4.1 Introduction

When a molecule is ionized its structure becomes imprinted on the *ejected* electron. This was first discovered almost a century ago through the study of the X-ray absorption fine-structure, i.e. the oscillatory structure of the X-ray absorption cross-section in the energy region following an ionization threshold. Kronig showed in 1932 that the absorption fine-structure could be explained by the *diffraction* of the ejected electron within the molecular frame [106]. The diffraction effect described by Kronig forms the basis for techniques such as Extended Absorption Fine-Structure (EXAFS) spectroscopy, see e.g. [107], and photoelectron diffraction, see e.g. [21], that have been used extensively for material structure studies over the past decades. In 1966, Cohen and Fano [46] identified another molecular structure effect in the photoabsorption spectra of of O_2 and N_2. They showed that the *coherent emission* of a photoelectron from distinct atomic centres within the molecule leads to an interference effect that causes oscillations in the photoabsorption spectrum.

In Sec. 2.5.2 it was shown that electrons that are produced by *impact ionization* using a charged particle, e.g. an electron or an ion, may carry molecular structure information in similar ways as the photoelectrons. Impact Ionized Coherent Electron Emission (IICEE) is a generalization of the Cohen-Fano effect and leads to the interference between electrons that are ejected from two distinct atomic centres within a molecule [4]. A second mechanism that can give rise to molecular interference effects is Impact Ionized Secondary Electron Diffraction (IISED), which is a generalization of the photoelectron diffraction effect. That is, an impact ionized electron that is ejected from one of the atomic centres within the molecule can scatter elastically from *another* atomic center, which leads to interferences between the scattered and *non*-scattered electrons (see also Fig. 2.15).

Table 4.1: Overview of publications with experimental work on molecular structure effects in impact ionized electrons.

Ref.	Year	Projectile	Molecule	Detection
Stolterfoht *et al.* [47]	2001	Kr^{34+}	H_2	e^--TOF
Stolterfoht *et al.* [48]	2004	Kr^{33+}	H_2	e^--TOF
Hossain *et al.* [108]	2005	H^+	H_2	e^--TOF
Tanis *et al.* [53]	2006	Kr^{34+}	H_2	e^--TOF
Milne-Brownlie *et al.* [50]	2006	e^-	H_2	(e^-,$2e^-$)
Chatterjee *et al.* [109]	2008	e^-	H_2	e^--TOF
Baran *et al.* [49]	2008	H^+	N_2	e^--TOF
Hargreaves *et al.* [52]	2009	e^-	N_2	(e^-,$2e^-$)
Nandi *et al.* [110]	2012	C^{6+}	O_2	e^--TOF

Table 4.1 shows an overview of some of the most important experimental results with regard to the effect of the molecular structure on impact ionized (secondary) electrons produced using ion or electron impact. The first experimental demonstration of the IICEE effect in 2001 resulted from experiments with heavy *ion* impact, i.e. Kr^{34+}, on H_2 and Helium [47]. Stolterfoht *et al.* [47] obtained secondary electron energy spectra of H_2 and Helium at several fixed angles with respect to the incoming Kr^{34+} projectile using an electron electron Time-Of-Flight (e^--TOF) detector. They showed that IICEE interference effects could be observed in the ejected electron spectrum of H_2 as an oscillation around an effective 'atomic' term, which consists of twice the theoretical cross-section of a Hydrogen atom. No such oscillation was visible in the ejected electron spectrum of Helium after subtraction of its theoretical cross-section from the experimental data.

The pioneering experiment demonstrating the IICEE effect in 2001, was followed in 2004 and 2005 by two further experiments from the same group that claimed to show first experimental indications for the IISED effect [48, 108]. Stolterfoht *et al.* and Hossain *et al.* observed that superposed on the oscillation in the secondary electron spectrum of H_2 that was attributed to IICEE effects, there was another, smaller oscillatory component. This additional oscillatory component had a frequency that was double that of the IICEE oscillation and

was attributed to the interference between the secondary electrons that have scattered from the neighbouring atom and those that have not, i.e. IISED. However, additional measurements and a detailed analysis of all the experimental data by Tanis *et al.* [53] did not find conclusive evidence for the higher-frequency oscillations observed in the former experiments. Furthermore, ab-initio theoretical calculations did not reproduce the double frequency oscillatory component attributed to IISED, so that the interpretation of these results is still a matter of debate [4].

The first experiment using *electron* impact ionization to demonstrate coherent emission effects followed soon after the ion impact experiments in 2006 [50]. Milne-Brownlie *et al.* used an (e^-,$2e^-$) spectrometer, capable of detecting the momentum of all the outgoing electrons resulting from an individual ionization event [42], to measure the Triply Differential Cross-Section (TDCS) of Helium and H_2. The experimental TDCS was compared to Molecular 3-body Distorted Wave (M3DW) calculations [111] that indicated that the shape of the H_2 TDCS is slightly modified by the coherent emission interference effect. Chatterjee *et al.* [109] also looked for IICEE effects in electron impact ionization of H_2, but using an electron TOF detector. Compared to the experiments by Milne-Brownlie *et al.*, the experiment by Chatterjee *et al.* obtained incomplete information on the scattering process, because the scattered (primary) electron direction and energy is not observed. Nevertheless, they observed oscillations in the secondary electron spectrum that were attributed to IICEE effects using a similar analysis as Stolterfoht *et al.* in the ion impact experiments. This indicates that IICEE effects remain visible in the secondary electron energy spectrum of electron impact ionized H_2, even after averaging over the primary electron momentum.

The majority of experiments looking for molecular effects in impact ionized electrons used the H_2 molecule due to its simplicity with regard to theory. The experiments by Baran *et al.* [49], Hargreaves *et al.* [52], and Nandi *et al.* [110] undertook the next step in complexity by studying the impact ionization of N_2 and O_2 molecules. Baran *et al.* and Nandi *et al.* performed *ion* impact ionization experiments in combination with an electron TOF detector. In both cases it was found that there is a strong suppression of IICEE effects in these molecules compared to H_2. Baran *et al.* did observe some oscillations in the ejected electron spectra of N_2 after the subtraction of the 'atomic' contribution, but found that they did not match the theoretical predictions for the IICEE effect. Moreover, when comparing the experimental data to the theoretical predictions for the IICEE effect, it appeared that the experimentally observed oscillations had a higher frequency. It was concluded that the IICEE effect was suppressed due to the partial cancellation of the coherent emission effect from orbitals with *gerade* and *ungerade* symmetry. The experimentally observed oscillations were instead attributed to IISED effects, though no quantitative comparison with theory was provided. Nandi *et al.* observed no apparent oscillations in the secondary electron spectra of O_2. The comparison of the experimental data with IICEE calculations showed a qualitative match with the experiment, from which it was concluded that the cancellation of the contributions from orbitals with different symmetries was responsible for the lack of IICEE interferences. Finally, Hargreaves *et al.* performed *electron* impact ionization experiments on N_2. Using the (e^-,$2e^-$) detection scheme they studied the TDCS for the impact ionization of specific molecular orbitals. Comparing the experimental TDCS to the theoretical atomic Nitrogen TDCS, they identified IICEE effects in the experimental

data for the individual orbitals.

The effect of the molecular structure on the secondary electrons, that was demonstrated in the experiments described above, could in principle be used to image the molecular structure during a *dynamical* process. Photoelectron diffraction has in particular seen renewed interest with the recent development of intense, ultrafast X-ray sources, as a prospective candidate for direct imaging of nuclear motion with femtosecond temporal and Ångström spatial resolution [17, 18, 19]. However, the hard X-ray source required for successful implementation of ultrafast photoelectron diffraction means that such experiments must be performed at large user facilities, with the associated drawbacks of experimental complexity and restricted beam-time availability. This offers the interesting prospect of using *table-top* Ultrafast Electron Diffraction (UED) sources, which are readily available and can even be obtained commercially [20], to generate energetic secondary electrons that may be used for ultrafast molecular structure imaging.

This chapter presents some first results from the combination of a table-top UED source with a Velocity Map Imaging Spectrometer (VMIS) that is applied to the study of secondary electron emission. The VMIS is capable of obtaining the full momentum distribution of the secondary electrons generated by electron impact ionization, and can provide more complete spectral information compared to the electron TOF detectors used in some of the earlier experiments introduced above. By comparing the spectra of Helium and of H_2 to theoretical calculations, it is shown that hints of IICEE effects due to the molecular structure of H_2 may be visible in the experimental data. Because molecular structure effects are seen to be very weak, it is shown using theoretical calculations how such effects can be brought out more clearly in the secondary electron spectrum by *aligning* the molecules.

Section 4.2.1 gives a short summary of the experimental setup and its main specifications. Some of the more challenging aspects of the experiments presented here were the low signal levels and the large amount of background signal, which are treated in Sec. 4.2.2 and Fig. 4.2.3, respectively. The experimental secondary electron spectra of the atoms Helium and Xenon, and the molecules H_2 and N_2 are presented in Sec. 4.3, together with a qualitative discussion of the spectra based on the theory of electron impact ionization. In Sec. 4.4 Distorted Wave Born Approximation (DWBA) calculations are used to get to a quantitative understanding of the spectra of Helium and H_2. The Helium case is used as a benchmark and shows a good match between theory and experiment. Using the DWBA theory, together with the Independent Atom Model (IAM) to treat the two-center emission effect in H_2, it is shown that molecular structure effects are possibly visible in the shape of the secondary electron spectrum. Finally, in Sec. 4.5 the DWBA model is used to simulate secondary electron spectra of *aligned* H_2, showing that, analogously to the LIED experiments presented in Chapter 3, fixing or restricting the molecular frame in space can bring out the structural effects in a much clearer way.

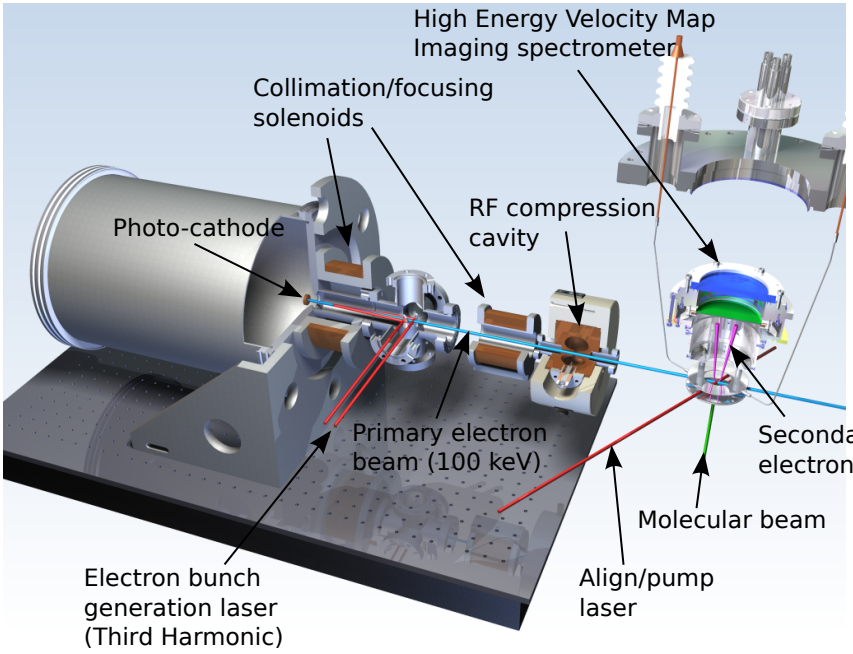

Figure 4.1: Illustration of the experimental setup consisting of a table-top Ultrafast Electron Diffraction source and a high-energy Velocity Map Imaging Spectrometer (VMIS).

4.2 Experimental setup

4.2.1 Experimental apparatus

The experimental setup is based on a commercially available electron source developed for Ultrafast Electron Diffraction (UED) [20, 112]. The setup consists of a 100 keV electrostatic field accelerator and a microwave cavity for the temporal compression of the electron bunches. The microwave cavity is essentially a temporal lens which produces a time-dependent electric field such that the fast electrons, which are at the front of an expanding electron bunch, are decelerated, while the slower electrons, at the back of the bunch, are accelerated. A detailed description of the electron source design and its characterization can be found in [113].

A summary of the design specifications for this version of the electron source is shown in Table 4.2. This electron source was designed to accommodate tighter focusing of the electron beam, as required for the operation of the source in combination with a Velocity Map Imaging Spectrometer (VMIS). The estimated pulse duration and focal size are based on an initial simulation report for this version of the electron source with the General Particle Tracer (GPT) code [114, 115]. It must be remarked that the total temporal resolution of the electron source setup is affected by synchronization *jitter* between the laser and the compression cavity, which was not included in the aforementioned GPT simulation. Based on publications using a similar microwave cavity compressor, the

jitter contributions can be as large as 200 fs [116, 117].

Table 4.2: Ultrafast electron source specifications [115].

Specification	Value
Electron energy	100 kV
Repetition rate (max.)	30 kHz
Bunch charge	40 fC ($\sim 10^5$ e^-)
Pulse duration[1]	50 fs
Focal size	50 µm

Due to experimental limitations, i.e. low signal levels, the electron source was not operated in a time-resolved manner in the current experiments. In order to get the highest possible signal level a bunch charge of ∼4000 fC was used, which is two orders of magnitude larger than the nominal specified bunch charge of 40 fC. Moreover, to maximize the cross-section, which is inversely proportional to the the primary electron beam energy, the electron source was operated at a lower acceleration voltage of 30 kV.

The accelerator is a simple solid Copper photo-cathode biased at the acceleration voltage and pumped by the third harmonic (266 nm) of the main laser system. The ultrafast laser system is an 800 nm, 1 kHz repetition rate system with a total of 3 mJ pulse energy and 30 fs pulse duration. The third harmonic pulses were produced by 10% – 30% of the main laser output using a Type-I BBO crystal for Second Harmonic Generation (SHG) and a Type-II BBO for Sum Frequency Generation (SFG). The quantum efficiency of the photo-cathode was measured to be approximately 10 pC/µJ, which is close to the value of 5 pC/µJ provided by [113].

The main feature of this setup is the unique combination of an ultrafast electron source with a high-energy VMIS capable of measuring up to 1.5 keV secondary electrons produced by the initial fast electron beam. A more detailed description of the VMIS can be found in Sec. 3.2.1. One main concern with this combination is the effect of the VMIS electric fields on the primary electron beam propagation. Two sets of electrostatic beam deflectors were integrated with the VMIS in order to guide the incoming electron beam through the spectrometer (see Fig. 4.2). A set of deflectors consists of an in-plane deflector and an out-of-plane deflector, which are mounted vertically and horizontally, respectively, inside the VMIS vacuum chamber. Each beam deflector consists of a pair of 1.5 cm wide aluminium parallel plates that are separated by 1 cm dielectric spacers. One set of deflectors at the VMIS entrance is used to intersect the incoming electron beam with a molecular beam at the interaction point within the spectrometer. The second set of deflectors at the VMIS exit ensures that the outgoing beam does not hit the spectrometer chamber walls and is directed onto a Faraday cup assembly attached behind the spectrometer to measure the primary beam current.

The molecular beam is produced by an Even-Lavie valve [97] operated at a repetition rate of 750 Hz, with an opening time of 26 µs, and with a nozzle

[1] Excludes the contribution from synchronization jitter.

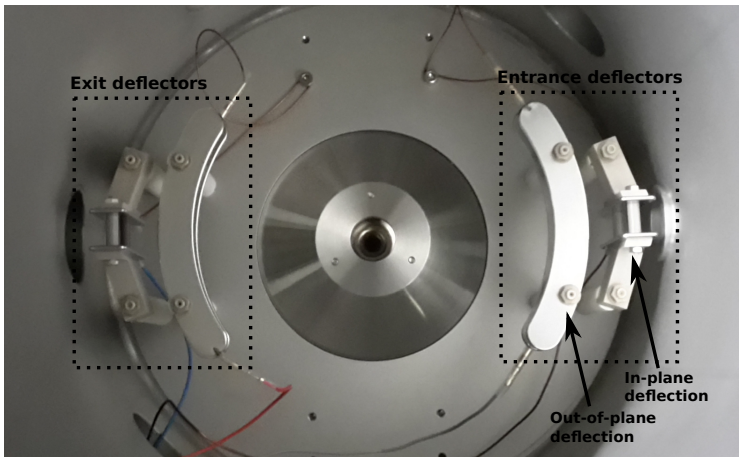

Figure 4.2: Photograph of the electrostatic beam deflectors within the VMIS vacuum chamber that are used to steer the electron beam through the spectrometer. The VMIS, which was removed in order to take this picture, is located between the two deflector sets.

size of 100 µm. Pure samples of the target molecule at backing pressures of 3 – 4 bar were used. The molecular beam is passed through a 1 mm diameter skimmer before entering the detector chamber. The total distance between the valve nozzle and the interaction region was kept as small as possible, i.e. ∼15 cm, to maximize the target density at the interaction point.

4.2.2 Signal level estimates

One of the challenging aspects of the presented experiments was the relatively low signal level. The two main factors required to estimate the signal level in these experiments are the molecular beam density and the total electron impact ionization cross-section. The molecular beam density can be estimated using the idealized continuum model for supersonic expansion from circular nozzles given by Morse [96]. The density of the molecular beam ρ after some distance d is in this semi-empirical model given by the following equations

$$\begin{aligned} \frac{\rho}{\rho_0} &= W^{-1/(\gamma-1)} \\ W &= 1 + \frac{1}{2}(\gamma-1)M^2 \\ M &= \beta - \frac{1}{2}\frac{(\gamma+1)}{(\gamma-1)\beta} \\ \beta &= A\left(\frac{x-x_0}{D}\right)^{\gamma-1} \end{aligned} \tag{4.1}$$

In these equations ρ_0 is the molecular density of the gas in the reservoir, D is the nozzle diameter, γ is the heat capacity ratio[2], and x_0 and A are fitting parameters. Using the experimental parameters provided in the previous section, and the fitting parameters provided by Morse [96], the molecular beam density at the interaction point in the current experiments is estimated to be $4.8 \times 10^{12}\,\mathrm{cm}^{-3}$ for the atomic and $3.7 \times 10^{12}\,\mathrm{cm}^{-3}$ for the diatomic gases.

The total ionization cross-section can be estimated using Lotz's empirical formula [118] for the high-energy electron impact ionization of atoms given by

$$\sigma = \sum_{i}^{N} a_i q_i \frac{\log(E/P_i)}{E P_i} \tag{4.2}$$

In this equation E is the primary (projectile) electron energy and the sum runs over the N electron shells of the atom where q_i is the number of electrons in the shell, P_i is the ionization energy, and a_i is an empirical fitting parameter (see also [119, 120]). The molecular cross-section is assumed to be given by the sum of the cross-sections of the constituent atoms. The cross-sections for the atoms and molecules used in the current experiments at primary electron energies of 30 and 100 keV are shown in Table 4.3.

Table 4.3: Total electron impact ionization cross-sections for the atoms and molecules used in the current experiments.

	Cross-section ($10^{-18}\,\mathrm{cm}^{-2}$)	
Species	30 keV	100 keV
Helium	0.77	0.27
Xenon	7.2	2.5
H_2	1.5	0.5
N_2	5.2	1.8

Using the molecular beam density ρ and the cross-sections σ obtained using (4.1) and (4.2), respectively, the total number of ionization events per second, i.e. signal level, can be calculated and is given by

$$R = N_e\, f_{exp}\, d_{int}\, \rho\, \sigma \tag{4.3}$$

where N_e is the number of electrons per bunch, f_{exp} is the repetition rate of the experiment, and d_{int} is the interaction region length. The interaction region length is given by the molecular beam diameter, while the experimental repetition rate is limited by the opening frequency of the pulsed molecular valve.

[2]The heat capacity ratio for an ideal gas is $\frac{5}{3}$ for a mono-atomic gas and $\frac{7}{5}$ for a diatomic gas at room temperature.

Table 4.4: Calculated signal level for the current experimental conditions.

Species	Signal ($10^4\,s^{-1}$)
Helium	0.69
Xenon	6.5
H_2	1.0
N_2	2.7

Assuming that it is necessary to record a momentum map with a resolution of 500 by 500 pixels and with a total number of 100 events per pixel, the acquisition time per momentum map for the signal levels listed in Table 4.4 is calculated to be between 6 and 60 minutes. The calculated acquisition times are lower than the acquisition times used during the experiments, which were between 20 minutes and 2 hours. This discrepancy is not understood and may be due to an overestimation of some of the experimental parameters, or due to sub-optimal experimental conditions. Another factor that must be kept in mind is that for the study of molecular structure effects it is necessary to observe the momentum map at relatively high momenta, i.e. > 1 a.u. As will be shown in Sec. 4.3, the cross-section drops off very quickly as the kinetic energy of the ejected electron increases. As a result, the effective signal level for the momentum range of interest is at least one order of magnitude lower than the total number calculated above.

4.2.3 Data acquisition and processing

Another challenging aspect of the current experiments was the large amount of background signal in the images. The two main background contributions to the spectrum were found to be (primary) electron beam scattering from *surfaces* and from *residual gas*.

When the primary electron beam scatters from a surface it produces large amounts of secondary electrons. Due to the large electron beam currents employed in these experiments, space-charge effects were very pronounced. The electron beam could get very hard to control and a diffuse cloud surrounding the main beam produced rather strong background contributions due to surface scattering. Moreover, though the primary electrons are dumped into a Faraday cup at a rather large distance of >50 cm from the interaction region, the secondary electrons generated by this process were also visible in the VMIS images.

The second strong background contribution was found to be the ionization of the residual sample gas in the VMIS chamber. In order to maximize the signal level the molecular valve was operated at a high repetition rate and was placed very close to the skimmer separating the molecular source chamber from the spectrometer. Unfortunately, this also results in a rather high background gas load in the spectrometer chamber because of the continuous leaking of gas from the source chamber. Due to the strongly ionizing character of the primary electrons, and the much longer propagation length over which the primary electrons can ionize the background gas, this results in a significant signal from

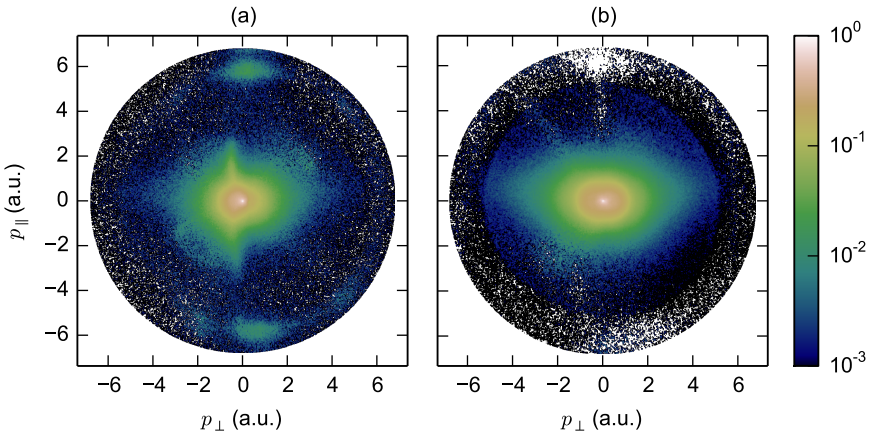

Figure 4.3: N_2 secondary electron spectrum with background subtraction by (a) turning the valve on and off and (b) delaying the valve timing by 200 µs.

the interaction of the primary electron beam with the residual gas in the spectrometer chamber. Trying to subtract background contributions by *switching off* the molecular beam is effective in the case of the previously described surface scattering contributions, because these contributions remain visible after the molecular beam has been switched off. However, once the molecular beam is off, the background gas load in the VMIS chamber, and the corresponding contribution in the acquired background image, is also eliminated. This results in a strong presence of the background gas load contributions in spectra where the background image is acquired with the molecular valve switched off, as illustrated in Fig. 4.3(a).

The experimental data is therefore acquired in a specific way so as to enable both the subtraction of background gas load and surface scattering contributions from the spectrum. This is done by introducing a *delay* between the electron bunches and the molecular beam pulses when acquiring the background image, such that the molecular beam pulse arrives 200 µs after the electron bunches. The background image then contains both the surface *and* background gas contributions. Subtracting this background spectrum from the spectrum at optimum overlap between the electron and molecular beams produces relatively clean secondary electron spectra, as illustrated in Fig. 4.3(b). Furthermore, to avoid the effect of long-term system drift the background data was acquired in a repetitive fashion, which was also discussed in Sec. 3.2.2 in the context of the LIED experiments.

4.3 Experimental results

In order to understand the main features of a secondary electron spectrum, the VMI spectra of atomic targets as well as that of simple homo-nuclear diatomic molecules have been obtained. Moreover, several experimental studies on Impact Ionized Coherent Electron Emission (IICEE) made use of the comparison between the spectrum of Helium and H_2 in order to demonstrate the effect of

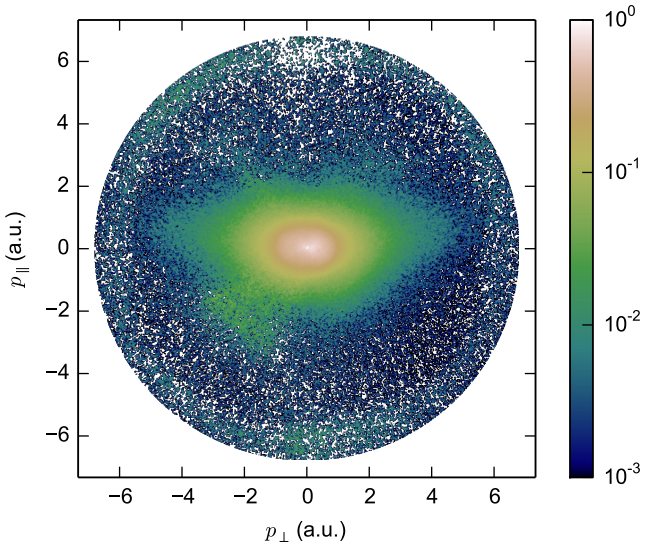

Figure 4.4: Helium; electron impact ionized secondary electron VMI spectrum. The incoming electron beam energy is 30 keV and its propagation direction is along the $p_\parallel$ axis in the positive direction, i.e. from bottom to top. The VMIS repeller and extractor voltages were 8.0 and 7.44 kV, respectively.

molecular structure on the spectrum [47, 50, 51, 121]. This approach will be followed in Sec. 4.4, where it will be shown that the Helium spectrum can be reproduced rather well with a Distorted Wave Born Approximation (DWBA) model. In the case of H_2 it will be shown that there may be some small two-center interference effect that is visible as a slight narrowing of the spectrum.

The secondary electron spectrum of Helium is shown in Fig. 4.4 . The incoming electron beam propagation axis is along $p_\parallel$, with the propagation direction in the positive direction, i.e. from page bottom to top. The conversion from image pixel units to absolute momentum units was performed using the VMIS energy calibration constants obtained from the LIED experiments presented in the previous chapter. The *shape* of the spectra can be qualitatively understood by considering the momentum distribution of the target electrons and the kinematics of the ionization process. As discussed in Sec. 2.4.2, electron impact ionization can be divided into two main kinematic arrangements (see also Figs. 2.7, 2.8 and 2.9). The first kinematic arrangement leads to 'dipole like' emission in which the emitted electron resembles a p-wave. This type of emission is dominant for ejection momenta comparable in magnitude to the width of the momentum distribution of the ejected electron before ionization; which is also inversely proportional to its *ionization energy*. As can be seen in Fig. 4.4 for the case of Helium the secondary electron spectrum at momenta below $\sim$2 a.u. is indeed dominated by dipole-like emission perpendicular to the incoming electron beam axis $p_\parallel$. The second kinematic arrangement is one in which the outgoing electron momentum is significantly larger than the bound electron momentum distribution. Secondary electrons with a large outgoing momentum are produced through a relatively hard, classical-like, interaction of the bound

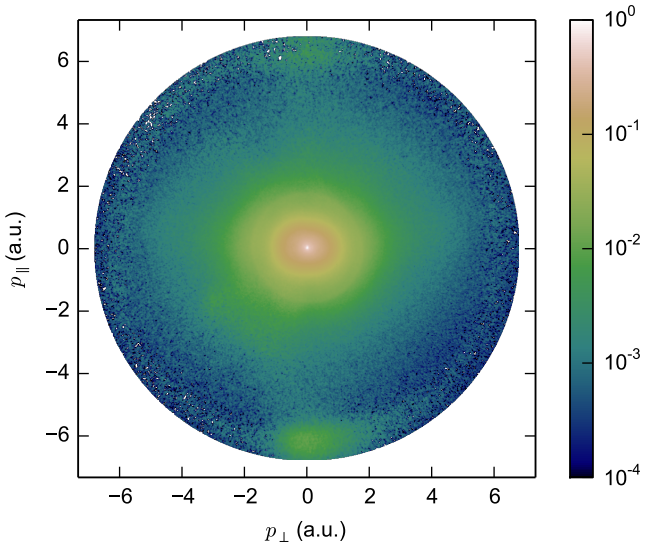

Figure 4.5: Xenon; electron impact ionized secondary electron VMI spectrum (see Fig. 4.4 for experimental details).

electron with the fast projectile. The secondary electron spectrum is then dominated by a single binary[3] peak, i.e. the Bethe-ridge. The binary peak is centred around the angle at which an electron with zero initial momentum would be scattered after interaction with the incoming projectile, and has a width determined by the momentum distribution of the bound state. In these experiments the primary beam has such a large initial momentum that an electron with zero initial momentum is ejected almost perpendicular to the primary beam, but with a small forward angle. This can indeed be observed in the Helium spectrum in Fig. 4.4. As the momentum distribution of the bound electron has a fixed width, determined by its ionization energy, it can also be seen in Fig. 4.4 that the binary peak is angularly more defined for higher outgoing momentum values.

The secondary electron spectrum of Xenon is shown in Fig. 4.5 and is seen to be rather uniform when compared to Helium. This implies that the secondary electrons are ejected through interactions involving orbitals with a very broad momentum distribution, i.e. high ionization energy. On the other hand, the ionization energy of the valence electrons of Xenon is only 12.1 eV, so that using the kinematic arguments above would lead to the conclusion that secondary electrons ejected from the valence shell should show a *narrower* distribution as compared to that of Helium. The secondary electron spectrum of Xenon in Fig. 4.5 therefore shows a strong contribution from electrons in lower lying shells, which have a very broad momentum distribution. Referring to the electron impact ionization theory outlined in Sec. 2.4.2, the contribution of lower lying shells can be due to direct ejection of electrons from those shells *or* due to

[3]The name binary peak refers to the fact that this feature arises from a kinematic arrangement where the projectile-electron interaction dominates, and the projectile-nucleus interaction can be neglected (see Sec. 2.4.2).

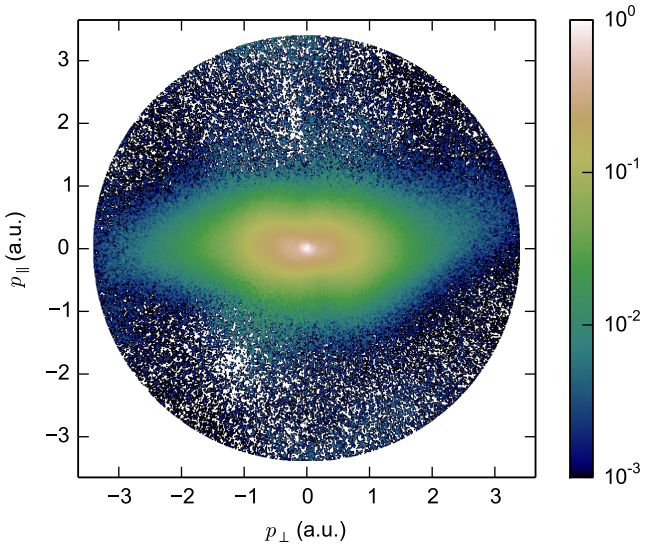

Figure 4.6: H_2; electron impact ionized secondary electron VMI spectrum. The VMIS repeller and extractor voltages were 2.0 and 1.86 kV, respectively.

indirect interaction of the projectile with lower lying electrons, which then leads to the ejection of electrons from higher shells.

The secondary electron spectra from the two *molecular* targets, H_2 and N_2, are shown in Figs. 4.6 and 4.7. The spectrum of H_2 shows the strongest anisotropy, i.e. narrowness of the spectrum, of all the target species used. This can of course be understood by the fact that it has a single binding orbital with an ionization energy of only 13.6 eV, and thus a correspondingly narrow bound electron momentum distribution. It is therefore also narrower than the Helium spectrum from Fig. 4.4, as the binding energy of Helium electrons is almost twice as large as that of Hydrogen. The spectrum of N_2 is relatively broad and reflects the presence of strongly bound electrons with wide momentum distributions besides its relatively loosely bound valence electrons, analogously to the case of Xenon.

Unfortunately, due to the low imaging voltages, the H_2 spectrum also displays some distortion, i.e. asymmetry around the $p_\parallel$ axis, which is likely due to stray electric and magnetic fields. The hydrogen spectrum was recorded at relatively low VMI voltages because its momentum distribution decays rather fast with outgoing momentum magnitude. This is of course a consequence of the narrow momentum distribution of its single molecular orbital. The N_2 spectrum was recorded at much higher VMI voltages and is consequently much more symmetric around the $p_\parallel$ axis. Due to imperfect background subtraction some artefacts can nevertheless also be seen in the N_2 spectrum, especially along the electron beam propagation axis $p_\parallel$. The N_2 spectrum shows a sharp circular feature at 5.2 a.u., which is indicated by the dotted white semi-circle. The position of this feature matches well with the N_2 K-shell Auger peak observed by Baran *et al.* [49].

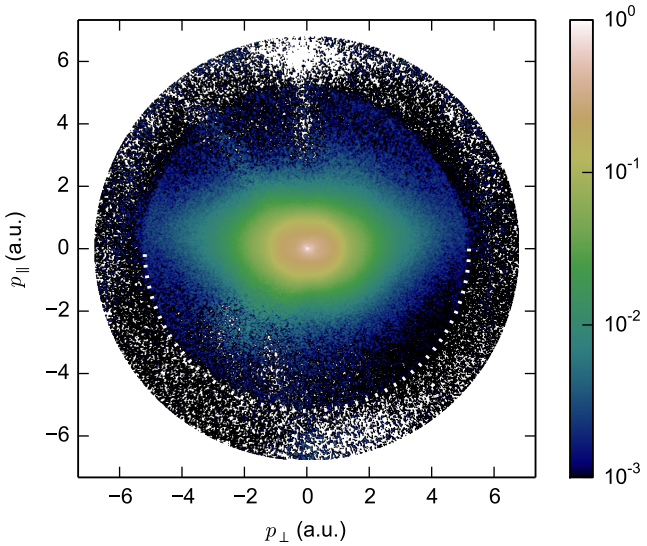

Figure 4.7: N_2; electron impact ionized secondary electron VMI spectrum (see Fig. 4.4 for experimental details). The dotted white semi-circle has a radius of 5.2 a.u.

4.4 Distorted Wave Born Approximation calculations

In this section a model based on the First Born Approximation will be used to calculate the ionization spectra of the Helium atom and H_2. The Helium atom ionization spectra may be considered as a benchmark case and it will be shown that the model spectra are indeed in good agreement with the experimental results. A comparison between the H_2 calculations, using a similar model, and the experimental data indicate that molecular two center interference effects may be visible as a slight narrowing of the secondary electron spectral shape.

In Sec. 2.4.2 an introduction was given to the theory of atomic and molecular impact ionization. The Distorted Wave Born Approximation (DWBA) was introduced and expressions for the ionization of atomic Hydrogen were given [29]. The main feature of this treatment was the use of the *Coulomb wavefunction* $\psi_c(\boldsymbol{k_e}, \boldsymbol{r_2})$ for the ejected electron to take the effect of the ionic potential into account. This is especially important for the spectrum at low ejection momenta. The treatment of the Helium atom follows roughly the same lines as that of the Hydrogen atom and its DWBA scattering amplitude is given by the following integral

$$f_{He}^{DWBA} = -\frac{1}{2\pi}\int \exp(\mathrm{i}\boldsymbol{q}\cdot\boldsymbol{r_0})\psi_c(\boldsymbol{k_e},\boldsymbol{r_2})\varphi_e^*(\boldsymbol{r_1})\times \left(-\frac{2}{r_0}+\frac{1}{r_{01}}+\frac{1}{r_{02}}\right)\phi_i(\boldsymbol{r_1})\ \mathrm{d}^3\boldsymbol{r_{0\ldots2}} \quad (4.4)$$

where $\boldsymbol{r_0}$, $\boldsymbol{r_1}$ and $\boldsymbol{r_2}$ are the coordinates of the projectile, remaining bound

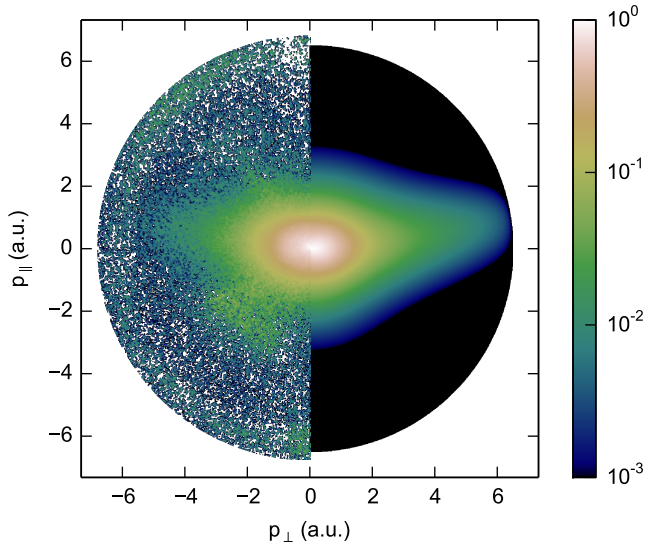

Figure 4.8: Comparison between the experimental (left half) and simulated (right half) secondary electron spectrum of Helium.

and ejected electron respectively, k_e is the ejected electron momentum, and $\boldsymbol{q} = \boldsymbol{k_i} - \boldsymbol{k_s}$, where $\boldsymbol{k_i}$ and $\boldsymbol{k_s}$ are the incoming and scattered electron momenta. These integrals, involving the Coulomb wavefunction, can actually be evaluated analytically and expressions are given in [122]. Care must be taken to include the projectile-nucleus term $2/r_0$, which leads to dipole like emission and is especially important for the spectrum at low momenta.

The simulated VMI spectrum of secondary electrons from Helium is shown in Fig. 4.8. The VMI spectrum is obtained by averaging the differential cross-section, calculated using (4.4), over the scattering angle of the projectile electron. The kinetic energy of the projectile is fixed by energy conservation. In order to compare the simulation with the raw VMI spectrum, the simulated spectrum was *Abel projected*. The advantage of this approach is that experimental data regions with very low signal levels are not contaminated by any additional noise introduced by *Abel inversion* procedures. To compare the simulated and experimental spectra in a more quantitative way, the signal along the $p_\parallel$ axis, i.e. the electron beam propagation axis, is considered in Fig. 4.9. The plotted signal is from a cut along the $p_\parallel$ axis that is integrated in the $p_\perp$ axis direction for momenta in the range of -0.2 to 0.2 a.u. Fig. 4.10 shows the *relative difference* between the simulated spectrum and experimental data, i.e. $(\sigma_{exp} - \sigma_{sim})/\sigma_{sim}$. For momenta of up to 2 a.u. the relative difference tends toward zero, indicating a good match between theory and experiment. At momenta above ∼2 a.u. the experimental data starts going below the noise level, which is visible as an increase in the standard deviation and a stronger deviation of the experimental data from the simulated curve.

For H_2, a model of electron impact ionization introduced by Stia *et al.* [58] is used. This gives the molecular ionization cross-section as a product of the atomic Hydrogen cross-section σ_A and an oscillatory two-center interference

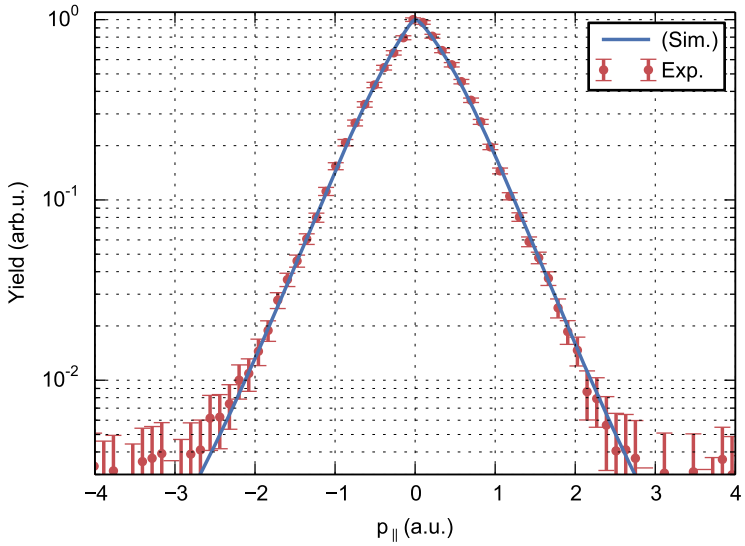

Figure 4.9: Comparison between the DWBA simulation (blue line) and the experiment (red dots) of the Helium secondary electron spectrum along the $p_{\parallel}$ axis. The plotted curves are obtained from a cut of the spectrum along the $p_{\parallel}$ axis that is integrated along the $p_{\perp}$ axis direction from -0.2 to 0.2 a.u. The simulated spectrum is normalized and then scaled with a fixed pre-factor to take the low-energy peak in the experimental data into account.

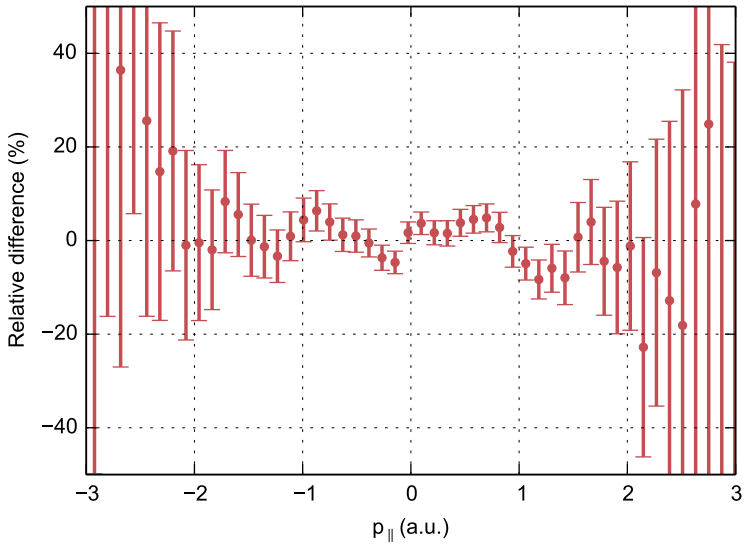

Figure 4.10: The relative difference between the experimental data and simulated curve, i.e. $(\sigma_{exp} - \sigma_{sim})/\sigma_{sim}$, shown in Fig. 4.9.

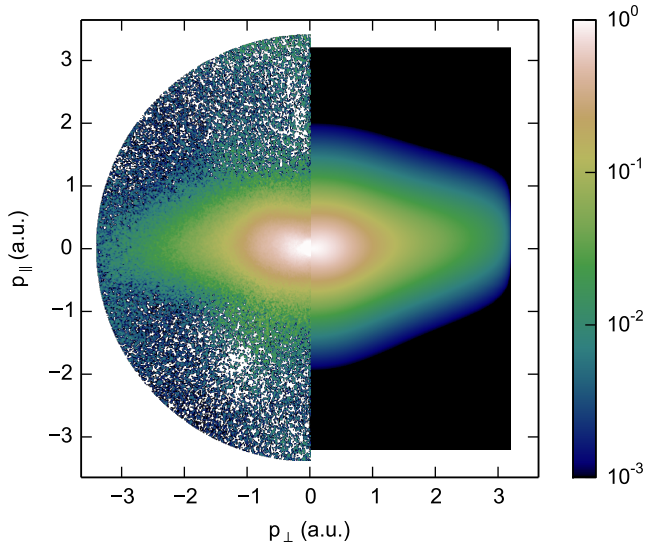

Figure 4.11: Comparison between the experimental (left half) and simulated (right half) secondary electron spectrum of H_2.

term

$$\frac{\mathrm{d}\sigma_M}{\mathrm{d}k_e\,\mathrm{d}\Omega_e\,\mathrm{d}\Omega_s} = \sigma_A(\boldsymbol{k_i}, \boldsymbol{k_s}, \boldsymbol{k_e})\big[2 + 2\cos(\boldsymbol{\Delta}\cdot\boldsymbol{R})\big] \tag{4.5}$$

In this equation $\boldsymbol{\Delta} = \boldsymbol{k_i} - \boldsymbol{k_s} - \boldsymbol{k_e}$, where $\boldsymbol{k_i}$,$\boldsymbol{k_s}$, and $\boldsymbol{k_e}$ are the incoming, scattered and ejected electron momenta, respectively, and $\boldsymbol{R}$ is the molecular axis vector. In Sec. 2.5 it was shown that this formulation is in fact an Independent Atom Model (IAM) applied to the case of IICEE. The electron impact ionization cross-section of atomic Hydrogen is calculated using analytical DWBA expressions [29]. Fig. 4.11 shows the resulting simulated VMI spectrum of secondary electrons from H_2. The VMI spectrum is obtained by averaging the differential cross-section given by (4.5) over the scattering angle of the projectile electron *and* the molecular axis orientation.

In order to look for two-centre interference effects in the spectrum, a comparison between the experimental and simulated VMI spectrum along the $p_\parallel$ axis of atomic Hydrogen and H_2 is shown in Fig. 4.12. Firstly, an intense low-energy peak, which is not represented by the DWBA model, can again be seen in the experimental spectrum. Secondly, the experimental data does not provide an *absolute* cross-section and only the shape of the simulated spectra can be compared to the experiment. This is an important difference from some of the previous experiments which use the fact that the absolute cross-section of H_2 can be significantly larger than that of two separate Hydrogen atoms for certain outgoing momenta [109]. In Fig. 4.12 the two simulated curves are therefore normalized to each other and scaled with a single pre-factor to take care of the low-energy peak.

The exact mechanism responsible for the low-energy peak is currently not known and a more comprehensive theoretical model seems to be necessary to quantitatively reproduce the data at the lowest energies. The DWBA model is a

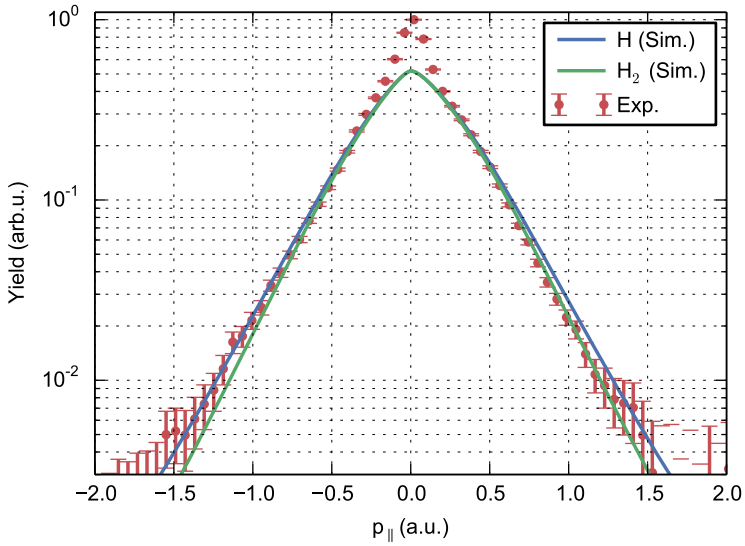

Figure 4.12: Comparison of the DWBA-IAM simulation of the secondary electron VMI spectrum of atomic Hydrogen (blue line) and H_2 (green line) and the experiment (red dots). The plotted curves are obtained from a cut of the spectrum along the $p_{\parallel}$ axis that is integrated along the $p_{\perp}$ axis direction from -0.2 to 0.2 a.u. The simulated spectra are normalized and then scaled with a fixed pre-factor to take the low-energy peak in the experimental data into account.

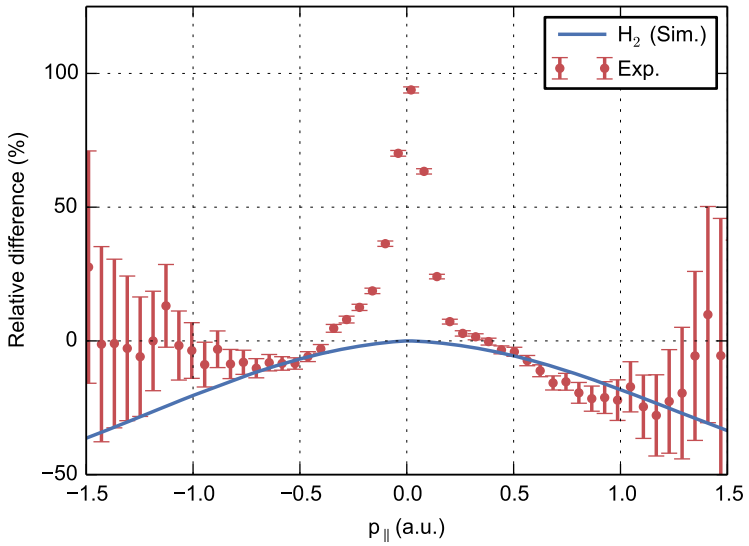

Figure 4.13: The relative difference between the atomic Hydrogen simulation and both the H_2 simulation (blue line) as well as the experimental data (red dots) that are shown in Fig. 4.12.

perturbative model based on the Born series, which assumes that the ionization proceeds through a single interaction of the incoming projectile with *one* of the bound electrons, followed by its immediate ejection. As mentioned previously, the DWBA model also takes the effect of the ionic Coulomb potential on the ejected electron into account. It would seem that the low-energy peak originates from other types of interactions that are not represented in this model. One possibility, which is not included in the DWBA model, is that the ejected electron is not ionized immediately, but is first excited into an intermediate state before it is finally ejected. Finally, it is noted that the spectra of N_2 *and* of Xenon display a similar low-energy peak (see Figs. 4.5 and 4.7), so that the mechanism behind this phenomenon does not necessarily require the presence of molecular structure.

From the simulated curves in Fig. 4.12 it can be seen that a two-center interference effect in the H_2 spectrum should manifests itself as a slight narrowing of the distribution as compared to atomic Hydrogen. The experimental spectrum indeed seems to be slightly more narrow than the atomic Hydrogen simulation would suggest. To show this effect more clearly, the relative difference between the atomic Hydrogen simulation and both the H_2 simulation and the experimental data is shown in Fig. 4.13. The relative difference between the atomic Hydrogen simulation and the experimental data is consistently below zero for momentum magnitudes between 0.5 and 1 a.u. The H_2 simulation suggests that this difference could be explained by coherent emission interference effects.

The simulated and experimental spectra of Helium and H_2 along the along the $p_\perp$ axis, i.e. *perpendicular* to the electron beam propagation axis, are considered in Figs. 4.14 and 4.15. As before, the simulated curves are multiplied with a fixed pre-factor and matched to the experimental data. The simulations are matched to the experiments in the same momentum range as was done for the spectra along the $p_\parallel$ axis, i.e. 1–2 a.u. and 0.5–1 a.u. for Helium and H_2,

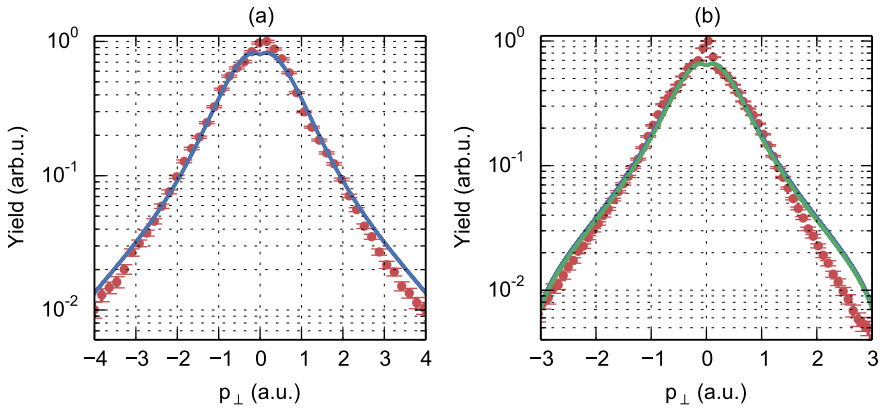

Figure 4.14: Comparison between the DWBA simulations (lines) and the experiments (red dots) of the (a) Helium and (b) H_2 secondary electron spectrum along the $p_\perp$ axis. The plotted curves are obtained from a cut of the spectrum along the $p_\perp$ axis that is integrated along the $p_\parallel$ axis direction from -0.2 to 0.2 a.u.

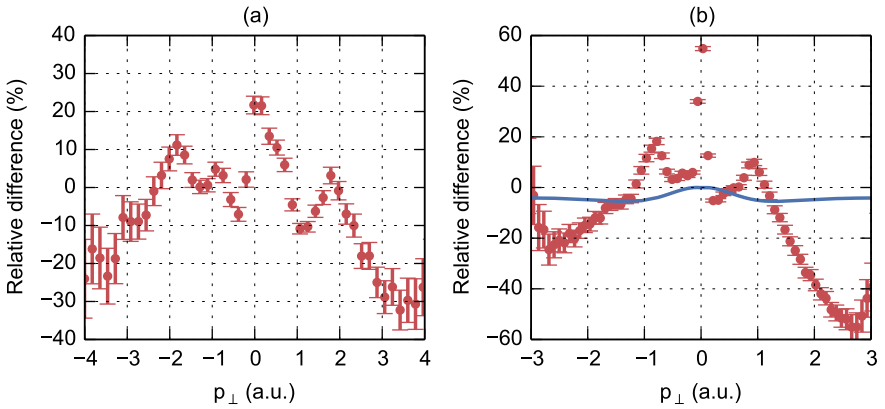

Figure 4.15: The relative difference between the experimental data and simulated curve for (a) Helium and (b) atomic Hydrogen for the corresponding plots shown in Fig. 4.14. The relative difference between the atomic Hydrogen and H_2 simulations is shown in (b) as the blue line.

respectively. It is clear that the discrepancy between the simulations and experiments is in this case larger than observed when looking along the $p_{\parallel}$ axis. The Helium simulation matches the data relatively well up to a momentum of ∼2.5 a.u., after which it lies significantly above the experimental data (see Figs. 4.14(a) and 4.15(a)). In the case of H_2 a similar situation is observed, where the simulations are significantly above the experimental curve for momenta above ∼1.5 a.u. (see Figs. 4.14(b) and 4.15(b)). The agreement between the simulations and experiments for the intermediate momentum range, i.e. 1–2 a.u. and 0.5–1 a.u. for Helium and H_2 respectively, is better, though not as good as was the case when considering the spectrum along the $p_{\parallel}$ axis. In particular, the experimental curve for H_2 shows a local peak in the momentum range of 0.5–1 a.u. that is not reproduced by the simulation. The deviation of the H_2 experimental data with respect to the simulation is also much larger than the expected effect of molecular structure (see Fig. 4.15(b), blue line), so that it is not possible to draw any conclusion with regard to the presence of IICEE effects. Comparing the simulated molecular curves in Fig. 4.15(b) and Fig. 4.13, it can be seen that the expected molecular effects are much smaller when considering the signal along the $p_{\perp}$ axis, rather than the $p_{\parallel}$ axis. Simulations with aligned molecules, which are presented in the following section, indeed indicate that IICEE effects should be most pronounced in the spectral region along the $p_{\parallel}$ axis.

The reason for the lack of agreement between the simulation and experiment in the spectrum along the $p_{\perp}$ axis is not clear. It is possible that the discrepancies are due to a physical effect that is not represented by the DWBA model, as is the case for the low-energy peak. However, the first Born approximation is expected to be more accurate for the high energy range considered here, and is used extensively in the field of (e,2e)-spectroscopy under similar conditions [42]. Another possible explanation for the observed discrepancy between the simulation and experiment at high momenta is VMIS imaging distortion. Radial distortions in the recorded image could in principle lead to the 'compression'

of the recorded spectra at high momenta and result in an effective shift of the experimental curves at these momenta. The experimental data in both cases displays a left/right asymmetry, which is especially pronounced in the case of H_2, that indeed indicates the presence of some imaging distortions in the experiments (see also Figs. 4.4 and 4.6). However, the level of radial imaging distortions required to explain the observed deviation is rather severe. A more detailed characterization of the VMIS at the relevant experimental conditions would be required for future experiments to exclude the possibility of such experimental errors.

As may be clear from the above discussions, the two-center interference effect is rather subtle in these experiments and a firm assignment is made difficult by several factors. Firstly, the low-energy peak is not represented by the DWBA model and this could introduce important systematic deviations in the comparison between simulation and experiment. Secondly, the experimental apparatus may also introduce systematic errors. For example, local variations in efficiency of the large-area detector, or background 'leakage', which is due to imperfect subtraction of the background contributions discussed in Sec. 4.2.3, could cause local signal modulations that are visible in the experimental spectra. VMIS imaging distortions are another possible source of error in the experimental spectra. However, the two-center interference effect should become more apparent as the momentum of the ejected electron increases. Unfortunately, the signal level also decreases exponentially with increasing ejection momentum. When considering the spectrum along the $p_{\|}$ axis, which is where the strongest molecular effect is expected, the current experimental signal-to-noise ratio (SNR) of 2 orders of magnitude is not sufficient to see above ≈1.3 a.u. of momentum. Increasing the SNR to above 3 orders of magnitude, as well as making sure that background load and other systematic error contributions are decreased to a minimum, should enable future experiments with this setup that are capable of clearly observing IICEE effects in H_2.

4.5 IICEE with aligned molecules

For unaligned molecules the molecular structure interference effects become very small due to averaging over *two* degrees of freedom, namely the molecular orientation and the scattering angle of the fast incoming electron (see also Sec. 2.5.2). Fixing, or restricting, the molecular frame orientation in space can help to overcome this restriction and bring out structural effects in a much clearer way. Fig. 4.16 shows a comparison between the secondary electron spectrum of unaligned H_2 and that of H_2 molecules that are aligned parallel to the primary beam propagation direction $p_{\|}$. Two-center interference effects can be clearly observed as a nodal plane in the secondary electron spectrum. The location of the nodal plane can be estimated by considering the molecular structure term $[2 + 2\cos(\boldsymbol{\Delta} \cdot \boldsymbol{R})]$ from (4.5). This term is zero when $\boldsymbol{\Delta} \cdot \boldsymbol{R} = (2n + 1)\pi$, where $n = 0, 1, \ldots$ When the ejected electron momentum is small with respect to that of the projectile, the momentum of the projectile before and after scattering is almost equal so that $\boldsymbol{\Delta} \approx -\boldsymbol{k_e}$. The position of the first nodal plane in Fig. 4.16 is therefore approximately at $k_e = \pi/R$, which is 2.2 a.u. for the H_2 bond length $R = 0.74$ Å.

The effect of rotating the molecular frame with respect to the primary elec-

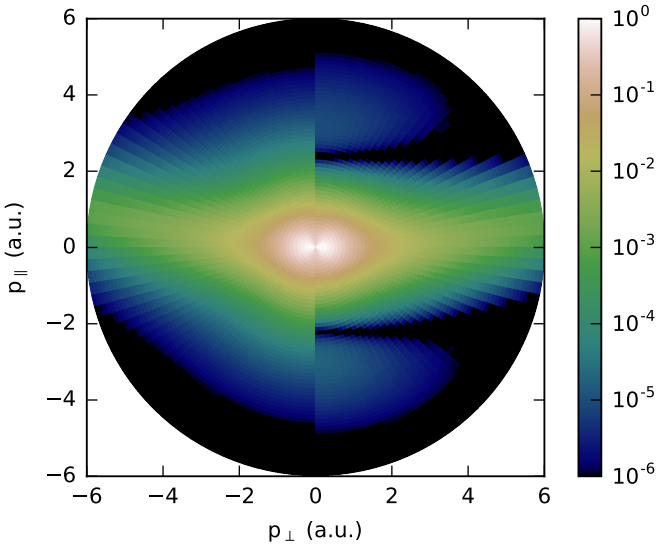

Figure 4.16: Comparison of the simulated secondary electron spectrum of *unaligned* H_2 (left half) and of H_2 *perfectly aligned* along the primary electron beam axis (right half).

tron beam propagation axis $p_{\parallel}$ is shown in Fig. 4.17. As one would expect from traditional diffraction imaging, the nodal planes rotate together with the molecular frame. However, unlike in conventional electron diffraction, the nodal planes are suppressed in modulation strength as the rotation angle approaches 90°. Such an effect has also been described in previous theoretical studies of IICEE effects in ion impact ionization of H_2 [4, 123]. The effect was explained as an increased sensitivity of the molecular interference factor in (4.5) to averaging over the projectile scattering angle for the perpendicular orientation of the molecule. Nevertheless, in experimental studies the perpendicular arrangement of the molecular frame could be interesting because the overall signal level is much higher at the position of the partially suppressed nodal plane at 2 a.u. In the parallel molecular frame arrangement this node is located in a region where the total signal level has decreased by more than 4 orders of magnitude, which may lead to more stringent SNR requirements.

It is interesting to investigate the visibility of molecular interference effects as a function of the *degree of alignment* of the molecular frame. Achieving high degrees of alignment is experimentally very challenging and often comes at the expense of achievable signal level. Fig. 4.18 shows a simulated spectrum of partially aligned H_2 with a degree of alignment of $\langle \cos^2 \theta \rangle = 0.7$. This is a moderate level of alignment which can be achieved for example with the impulsive laser alignment technique using moderate laser pulse energies. Fig. 4.18(a) shows that interference effects are in fact already visible in the raw spectra. Using a normalized difference image, such as employed very successfully in LIED experiments in Chapter 3, shows the pronounced effect of alignment on the spectrum. Further simulations indicate that molecular alignment effects should lead to variations in electron yield of up to 10% at degrees of alignment

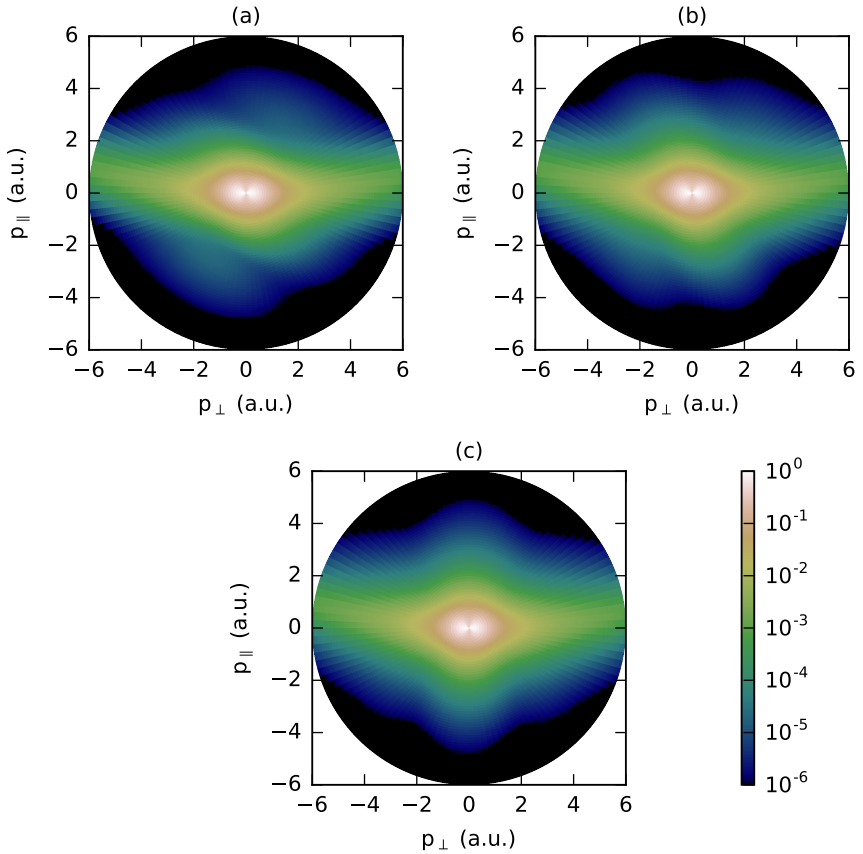

Figure 4.17: Simulated secondary electron spectrum of *perfectly aligned* H_2 rotated in-plane at an angle with respect to the primary electron beam propagation direction of (a) 30°, (b) 60° and (c) 90°.

as low as $\langle \cos^2 \theta \rangle = 0.5$. This is indeed encouraging and it is expected that the application of molecular alignment techniques to IICEE experiments will lead to a powerful approach enabling clear and unambiguous extraction of molecular effects from secondary electron spectra of impact ionized molecules.

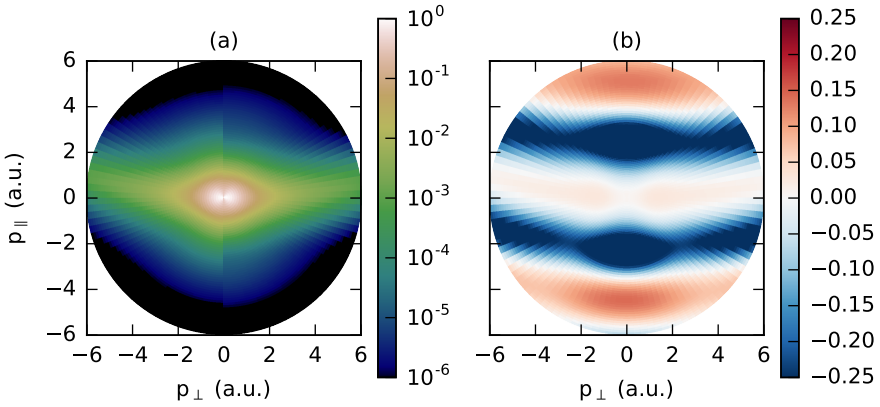

Figure 4.18: Simulated secondary electron spectrum of (a; left half) un-aligned and (a; right half) *partially* aligned H_2 with a degree-of-alignment of $\langle \cos^2 \theta \rangle = 0.7$ and (b) normalized difference image between the aligned and un-aligned H_2 spectra.

4.6 Conclusion

This work demonstrates the combination of a table-top ultrafast electron source and a VMIS that can be used to study electron impact ionization processes in molecules. This setup is specifically interesting in combination with the IICEE technique and can potentially be used for studies of structural dynamics in gas-phase systems. Spectra of atomic and molecular targets were acquired, demonstrating the capability of the experimental setup to image the momentum distribution of impact ionized secondary electrons.

In order to identify possible IICEE effects in the spectrum of H_2, a DWBA model was applied. The Helium spectrum along the $p_{\parallel}$ axis could be reproduced very well by the DWBA model, after accounting for the low-energy peak. In the case of H_2, DWBA calculations show that a two-center molecular interference effect should manifest itself as a slight narrowing of the secondary electron distribution as compared to atomic Hydrogen. This narrowing of the spectrum was possibly also visible in the experimental data along the $p_{\parallel}$ axis, though sources of systematic error in the experiment, and shortcomings of the DWBA model in reproducing the low-energy peak, make an unambiguous assignment difficult. The match between the Helium and H_2 simulations and experiments along the $p_{\perp}$ axis was not as good as that for the $p_{\parallel}$ axis. Due to the lack of agreement between simulation and experiment in this case, and the relatively small effect of the molecular structure, no IICEE effects could be observed.

The IICEE effects are expected to be more pronounced for higher ejected electron momenta, but due to a sharp decrease of the experimental signal it was not possible to observe the ejected electron spectrum at such high momenta. Increasing the signal-to-noise ratio in the experiment, as well as making sure that background load and other systematic error contributions are decreased to a minimum, should enable future experiments with this setup that are capable of clearly observing IICEE effects in H_2.

Fixing, or restricting, the molecular frame orientation in space can help to overcome systematic errors in the experiment *and* ease the comparison with theory. Simulations with perfectly aligned and partially aligned H_2 were used to illustrate the effect of alignment on the secondary electron spectrum. It is demonstrated that using the alignment effect leads to a powerful experimental approach that will enable clear and unambiguous extraction of molecular effects from secondary electron spectra of impact ionized molecules.

Chapter 5

Conclusion and outlook

This thesis investigated two different techniques that can potentially be used for the direct imaging of ultrafast structural dynamics of molecules at the femtosecond time scale and with Ångström spatial resolution. Conventional ultrafast diffraction and imaging techniques use *elastically* scattered energetic particles, i.e. X-rays or electrons, to probe the molecular structure. The two techniques studied in this thesis make use of *inelastic* processes to produce *ionized* (secondary) electrons, that are subsequently used to image the molecular structure.

Chapter 3 investigated the use of molecular alignment in combination with Laser Induced Electron Diffraction (LIED) [1, 2, 3]. A series of experiments were presented that consider the effect of the *molecular frame* on the Photoelectron Angular Distribution (PAD) of impulsively aligned and strong-field ionized CF_3I molecules using a Velocity Map Imaging Spectrometer (VMIS). It was shown that using the impulsive laser alignment technique enables taking *differential measurements* that bring out directly and clearly LIED effects in the PAD, even for a relatively *complex molecule* such as CF_3I and using a non-coincident detection setup such as the VMIS. A semi-classical model, in which the strong-field driven motion of the photoelectron in the continuum is treated classically and the re-scattering with the parent molecule is modelled quantum mechanically, reproduced the experimentally observed features in the high-energy range of the spectrum. It was shown that oscillations in the experimental PADs along the polarization axis can be interpreted as diffraction features. A comparison of the experimental results at different laser intensities and at two different probe wavelengths, i.e. 800 and 1300 nm, shows that the LIED effect is robust and reproducible for a wide range of experimental conditions and at comparatively low re-collision energies. In order to understand the PAD in the low-energy region, where the direct electrons that have not re-scattered with the parent molecule dominate the total signal, an accurate model of the strong-field ionization going beyond the semi-classical approach is required. Simulations of the current LIED experiments on CF_3I molecules using the Molecular Strong Field Theory (MSFT) developed by Milošević *et al.* [88, 89, 90, 91] were presented. The MSFT simulations showed important deviations from the experimental data and the semi-classical models that are currently not understood. The results from ab-initio Time-Dependent Density Functional Theory (TDDFT) calculations performed by DeGiovannini *et al.* show a relatively good match with the experimental data at all photoelectron

energies. The TDDFT calculations indicate that the contribution the Highest Occupied Molecular Orbital (HOMO) *and* of the lower-lying HOMO-1 are significant and can be identified in the experimental results, clearly illustrating the importance of molecular orbital effects in these experiments.

The experimental work on LIED presented in this thesis only considers the use of the technique in constructing static snap-shots of the molecular structure. Further experiments are needed to establish firmly the ability of the LIED technique to image structural *dynamics* in molecules. The only experiment so far to observe a possible indication of structural dynamics in a molecule using LIED was performed by Blaga *et al.* [69]. The bond length retrieved by Blaga *et al.* for the O_2 molecule was 0.1 – 0.15 Å shorter than its equilibrium bond length. This was interpreted as a possible indication of a contraction of the molecule following photoionization, and within the few femtoseconds it takes for the photoelectron to return and re-collide with the parent ion. These observations are indirect in the sense that there is no *pump* pulse that initiates a specific structural change in the molecule. Experiments that induce structural dynamics in a molecule with a pump pulse, and subsequently probe the molecular structure using LIED are therefore needed. The first follow-up experiments attempting to use LIED to image the structure of an I_2 molecule during photoinduced dissociation have already been performed using the experimental setup presented in this thesis, though without the use of molecular alignment. In future experiments it would be insightful to study such dynamical processes in combination with molecular alignment, because this can help to bring out molecular-frame effects more clearly and ease the comparison with theory. The combined use of aligned molecules and LIED is especially interesting when attempting to apply the technique to ever larger and more complex molecules. Using highly aligned molecules is expected to lead to a better understanding of the limitations and possibilities for applying the LIED technique to more general systems, and will offer a more stringent test for theoretical models that describe the strong-field ionization of such complex molecules.

On the theoretical side, further effort is needed to develop ab-initio calculations capable of modelling the strong-field ionization of relatively large and complex *molecules*, e.g. TDDFT. The development of the ab-initio models needs to be supplemented by the development of semi-classical and Strong Field Approximation (SFA) models that can be used to analyse and *interpret* the results of ab-initio calculations *and* of experiments. In particular the development of extended semi-classical LIED models that can accurately represent molecular orbital effects and multiple ionization channels would be very useful.

The second technique considered in this thesis proposes the use of secondary electrons produced by electron impact ionization for the imaging of the molecular structure during a dynamical process. Secondary electrons produced by electron impact ionization may carry information on the molecular structure through different physical mechanisms. Impact Ionized Coherent Electron Emission (IICEE) is a generalization of the Cohen-Fano effect and leads to the interference between electrons that are ejected from multiple, identical atomic centres within a molecule [4]. A second mechanism that can give rise to molecular interference effects is Impact Ionized Secondary Electron Diffraction (IISED). An impact ionized electron that is ejected from one of the atomic centres within the molecule can scatter elastically from *another* atomic center, which leads to interferences between the scattered and *non*-scattered electrons [4].

Chapter 4 presented some first results from the combination of a table-top Ultrafast Electron Diffraction (UED) source with a Velocity Map Imaging Spectrometer (VMIS) that is applied to the study of secondary electron emission. The spectra of atomic and molecular targets were acquired, demonstrating the capability of the experimental setup to image the momentum distribution of secondary electrons generated by electron impact ionization. In order to identify possible IICEE effects in the spectrum of H_2, a Distorted Wave Born Approximation (DWBA) model was applied. The Helium spectrum along the $p_{\parallel}$ axis could be reproduced very well by the DWBA model. In the case of H_2, DWBA calculations show that a two-center molecular interference effect should manifest itself as a slight narrowing of the secondary electron distribution as compared to atomic Hydrogen. This narrowing of the spectrum was possibly also visible in the experimental data along the $p_{\parallel}$ axis, though sources of systematic error in the experiment, and shortcomings of the DWBA model in reproducing a low-energy peak, make an unambiguous assignment difficult. The match between the Helium and H_2 simulations and experiments along the $p_{\perp}$ axis was not as good as that for the $p_{\parallel}$ axis. Due to the lack of agreement between simulation and experiment in this case, and the relatively small effect of the molecular structure, no IICEE effects could be observed. Fixing, or restricting, the molecular frame orientation in space can help to overcome systematic errors in the experiment and ease the comparison with the theory. Simulations with perfectly aligned and partially aligned H_2 were used to illustrate the effect of alignment on the secondary electron spectrum. It is demonstrated that using the alignment effect leads to a powerful experimental approach that will enable clear and unambiguous extraction of IICEE effects from secondary electron spectra of impact ionized molecules.

The use of secondary electrons produced by electron impact ionization to obtain information on the structure of the parent molecule is a rather recent development. Of all the different physical effects that can lead to molecular structure effects in the secondary electrons, IICEE is the only one that has been demonstrated consistently in a number of experiments [47, 50, 52]. Though several experiments have investigated IISED effects, a conclusive experimental demonstration has not yet been provided [48, 53, 4]. From the limited experimental and theoretical work considering IISED it is clear that these effects are rather weak, and that a lot of fundamental ground-work remains to be done. Consequently, the experiments performed so far have focused on the relatively strong IICEE effect in the simplest diatomic molecules, i.e. H_2, N_2 and O_2. Even in these 'simple' molecules the observation of IICEE effects can be challenging due to the partial cancellation of the coherent emission effect from orbitals with *gerade* and *ungerade* symmetry, as was shown for the case of N_2 and O_2 molecules [49, 110]. Future experiments that aim to observe IICEE effects in more complex molecules such as N_2 and O_2 may therefore require (e,2e) detectors that can identify the specific orbital from which the ionized electron originates by simultaneous detection of the energy of the projectile electron [52]. From the point of view of developing a more generally applicable technique, the IISED effect seems to be a more attractive option because it does not require the emission of electrons from identical atomic centres within the molecule. One important limitation for this development is the lack of availability of an accurate and simple theoretical model that can be used to analyse and interpret IISED effects. On the experimental side it would be necessary to

perform measurements with a very high signal-to-noise ratio, where systematic error contributions have been carefully minimized and calibrated, so that the experimental results and theoretical model predictions can be compared with the high precision required for the extraction of the molecular structure effects. The use of alignment, as in the LIED experiments, may significantly aid in the identification and extraction of IICEE and IISED effects in the spectra and will offer a more stringent test for the theoretical models.

Appendix A

Intense-field Many-body S-matrix Theory

The centerpiece of Strong Field Theory (SFT) is the process of *Hamiltonian partitioning*, such that the developed perturbation series includes the relevant interactions in its leading terms [66]. The crucial difference between conventional perturbation theory and the SFT is the application of *different* Hamiltonian partitioning schemes for the initial, intermediate and final states. This can be qualitatively understood in the following way. The initial electronic state is strongly bound and localized around the atom so that the *laser field* can be treated as a perturbation. However, once the photoelectron has reached the continuum the laser field dominates its behaviour, whereas the *atomic potential* can be seen as a perturbation. The success of the initial SFT approach has culminated in Intentse-field Many-body S-matrix Theory (IMST) which *formalizes* the process of Hamiltonian partitioning and provides a consistent and powerful formulation of the SFT [66]. IMST was developed specifically as a method to deal with problems that require *multiple* Hamiltonian partitioning schemes. In contrast, conventional perturbation theory taught in most text books on Quantum Mechanics, e.g. [30, 26, 28], is based on the concept of a *single* Hamiltonian partitioning. IMST is a very elegant and powerful method to understand and apply perturbation theory to multi-domain problems.

As IMST arises as a generalization of conventional perturbation theory, this shall be shortly introduced first. The starting point for the development of standard time-dependent perturbation theory is the Time-Dependent Schrödinger Equation (TDSE)

$$\mathrm{i}\hbar\frac{\partial}{\partial t}\left|\psi(t)\right\rangle = H(t)\left|\psi(t)\right\rangle \tag{A.1}$$

where $H(t)$ is a time-dependent Hamiltonian. For the purpose of describing the temporal behaviour of this system the *evolution operator* $U(t,t')$ will be introduced, which is defined as

$$\left|\psi(t)\right\rangle = U(t,t')\left|\psi(t')\right\rangle \tag{A.2}$$

From this definition it also follows that

$$U(t',t') = I \tag{A.3}$$
$$U(t,t') = U(t,\tau)U(\tau,t') \tag{A.4}$$
$$U^{-1}(t,t') = U(t',t) \tag{A.5}$$

where I is the unit operator. Moreover, conservation of probability requires that the operator is unitary so that

$$U^{\dagger}(t,t')U(t,t') = U(t,t')U^{\dagger}(t,t') = I \tag{A.6}$$

Finally, multiplying (A.6) on both sides by $U^{-1}(t,t')$ and using (A.5) leads to the identity

$$U^{\dagger}(t,t') = U^{-1}(t,t') = U(t',t) \tag{A.7}$$

Substituting (A.2) into (A.1) it is seen that the evolution operator must satisfy the Schrödinger equation

$$\mathrm{i}\hbar\frac{\partial}{\partial t}U(t,t') = H(t)U(t,t') \tag{A.8}$$

in order to describe the time-evolution of the original system described by the Hamiltonian $H(t)$. Formally then, integrating the above equation leads to the following *integral equation* for the evolution operator

$$U(t,t') = I - \frac{\mathrm{i}}{\hbar}\int_{t'}^{t} H(\tau)U(\tau,t')\,\mathrm{d}\tau \tag{A.9}$$

The unit operator I in this expression originally arises as an integration constant. That this integration constant must be the unit operator follows from the fact that applying the evolution operator given by (A.9) to some state and letting $t \to t'$, that same state must be returned unchanged. This is in fact the specification of the *initial state* of the system. A second form of the integral equation for the evolution operator can be obtained by taking the Hermitian conjugate of (A.9) and using identity (A.7). This leads to the following equivalent integral equation

$$U(t,t') = I - \frac{\mathrm{i}}{\hbar}\int_{t'}^{t} U(t,\tau)H(\tau)\,\mathrm{d}\tau \tag{A.10}$$

Obtaining the full evolution operator is equivalent to solving the original TDSE. However, the re-formulation of the original problem in terms of the evolution operator which satisfies the integral equations (A.9) and (A.10) is particularly useful in the application of perturbation theory. The first step in applying time-dependent perturbation theory is the *partitioning* of the original Hamiltonian into two parts

$$H(t) = H^{(0)}(t) + V(t) \tag{A.11}$$

where $H^{(0)}(t)$ is an exactly solvable main Hamiltonian, with evolution operator $U_0(t,t')$, and $V(t)$ is a weak, time-dependent perturbation. The second step would be to obtain an expression for the full evolution operator in terms of the known operator $U_0(t,t')$. This is done by transforming the system states to the so-called *interaction picture* defined by the transformation

$$|\psi(t)\rangle = U_0(t,t')\left|\psi^N(t)\right\rangle \tag{A.12}$$

Substituting this into the original TDSE (A.1) and using (A.11) leads to the *Tomonaga-Schwinger equation*

$$\mathrm{i}\hbar\frac{\partial}{\partial t}\left|\psi^N(t)\right\rangle = V^N(t)\left|\psi^N(t)\right\rangle \tag{A.13}$$

where $V^N(t) = U_0^\dagger(t,t')V(t)U_0(t,t')$. Defining an evolution operator in the interaction picture

$$\left|\psi^N(t)\right\rangle = U^N(t,t')\left|\psi^N(t')\right\rangle \tag{A.14}$$

and substituting into (A.13) leads to two integral equation equations for the evolution operator in the interaction picture which are analogous to (A.9) and (A.10)

$$U^N(t,t') = I - \frac{\mathrm{i}}{\hbar}\int_{t'}^{t} V^N(\tau)U^N(\tau,t')\,\mathrm{d}\tau \tag{A.15}$$

$$U^N(t,t') = I - \frac{\mathrm{i}}{\hbar}\int_{t'}^{t} U^N(t,\tau)V^N(\tau)\,\mathrm{d}\tau \tag{A.16}$$

Transforming these integral equations from the interaction picture back to the original picture requires obtaining an expression for the evolution operator in the interaction picture $U^N(t,t')$ in terms of the original evolution operator $U(t,t')$. Using definitions (A.2) and (A.14), together with the interaction picture transformation (A.12) leads to

$$U_N(t,t')\left|\psi^N(t')\right\rangle = U_0^\dagger(t,t')U(t,t')\left|\psi(t')\right\rangle \tag{A.17}$$

Furthermore, from (A.12) and (A.3) it also follows that

$$\left|\psi^N(t')\right\rangle = U_0^\dagger(t',t')\left|\psi(t')\right\rangle = \left|\psi(t')\right\rangle \tag{A.18}$$

so that the evolution operator in the interaction picture is indeed given by

$$U_N(t,t') = U_0^\dagger(t,t')U(t,t') \tag{A.19}$$

which is the desired relation. Substituting this into the integral equations (A.15) and (A.16) finally leads to the following expressions for the original evolution operator in terms of the perturbation $V(t)$ and the known evolution operator $U_0(t,t')$ corresponding to the main Hamiltonian $H^{(0)}(t)$

$$U(t,t') = U_0(t,t') - \frac{\mathrm{i}}{\hbar}\int_{t'}^{t} U_0(t,\tau)V(\tau)U(\tau,t')\,\mathrm{d}\tau \tag{A.20}$$

$$U(t,t') = U_0(t,t') - \frac{\mathrm{i}}{\hbar}\int_{t'}^{t} U(t,\tau)V(\tau)U_0(\tau,t')\,\mathrm{d}\tau \tag{A.21}$$

This integral equation formulation of the original TDSE is particularly suited to be solved by iterative approximation. That is, simply taking be the evolution operator for the *unperturbed* system U_0 as a first guess and substituting it on the right-hand side of (A.21) leads to an approximate expression for the full evolution operator. This approximate solution can then be substituted again,

leading to the next approximate solution, etc. Formally, this leads to the *Dyson series* expansion of the full propagator given by

$$U(t,t') = U_0(t,t') - \frac{\mathrm{i}}{\hbar}\int_{t'}^{t} U_0(t,\tau_0)V(\tau_0)U_0(\tau_0,t')\,\mathrm{d}\tau_0 - \left(\frac{\mathrm{i}}{\hbar}\right)^2 \int_{t'}^{t} U_0(t,\tau_1)V(\tau_1)U_0(\tau_1,\tau_0)V(\tau_0)U_0(\tau_0,t')\,\mathrm{d}\tau_0\,\mathrm{d}\tau_1 + \ldots \quad \text{(A.22)}$$

where $t > \tau_n > \tau_{n-1} \ldots \tau_0 > t'$.

According to the discussion above, applying the conventional time-dependent perturbation treatment based on a single partitioning of the Hamiltonian to strong field interactions with atoms and molecules leads to difficulties. This is due to the fact that, depending on the domain that the active electron is in, either the atomic potential *or* the laser field is dominant. It will now be shown how this case can be treated using *multiple* Hamiltonian partitionings, leading to the development of the IMST [66]. First, the initial Hamiltonian partitioning is defined as

$$H = H_i^{(0)} + V_i \quad \text{(A.23)}$$

and the final partitioning as

$$H = H_f^{(0)} + V_f \quad \text{(A.24)}$$

where $H_i^{(0)}$ and $H_f^{(0)}$ are the main Hamiltonian for the initial and final system configurations and V_i and V_f are the initial and final perturbation terms. In Strong Field Theory (SFT) the initial main Hamiltonian represents the field-free target system, whereas the final main Hamiltonian represents a free continuum electron in the laser field. Using the initial partitioning scheme (A.23) and substituting in (A.21) leads to the following integral equation for the full evolution operator

$$U(t,t') = U_i(t,t') - \frac{\mathrm{i}}{\hbar}\int_{t'}^{t} U(t,\tau)V_i(\tau)U_i(\tau,t')\,\mathrm{d}\tau \quad \text{(A.25)}$$

where $U_i(t,t')$ is the evolution operator corresponding to $H_i^{(0)}$. Similarly, using the final partitioning scheme (A.24) and substituting in (A.20) leads to

$$U(t,t') = U_f(t,t') - \frac{\mathrm{i}}{\hbar}\int_{t'}^{t} U_f(t,\tau)V_f(\tau)U_0(\tau,t')\,\mathrm{d}\tau \quad \text{(A.26)}$$

The final step is to substitute (A.26) into the right-hand side of (A.25), which leads to an *exact* expression for the full evolution operator

$$U(t,t') = U_i(t,t') - \frac{\mathrm{i}}{\hbar}\int_{t'}^{t} U_f(t,\tau_0)V_i(\tau_0)U_i(\tau_0,t')\,\mathrm{d}\tau_0 - \left(\frac{\mathrm{i}}{\hbar}\right)^2 \int_{t'}^{t}\int_{\tau_0}^{t} U_f(t,\tau_1)V_f(\tau_1)U(\tau_1,\tau_0)V_i(\tau_0)U_i(\tau_0,t')\,\mathrm{d}\tau_0\,\mathrm{d}\tau_1 \quad \text{(A.27)}$$

The first term in this expression is simply the evolution operator of the initial state which is governed by the main Hamiltonian $H_i^{(0)}$ and represents the part of the system which is not affected by the perturbation. The second term in

the equation is due to the first term in (A.26) and represents the transition at time τ_0 from the initial state governed by $H_i^{(0)}$ to a final state governed by $H_f^{(0)}$ through the perturbation V_i. The final term in (A.27) represents all remaining higher order interactions through the full evolution operator $U(t,t')$ which acts as an intermediate between the initial and final configurations.

An approximate solution for the evolution operator can immediately be constructed from (A.27) by simply neglecting the final term representing higher order processes. Alternatively, based on some insight with regard to the dominant physical process during the intermediate system evolution, it is possible to introduce an *intermediate* Hamiltonian partitioning

$$H = H_m^{(0)} + V_m \tag{A.28}$$

Repeating the same procedure as above and substituting the expression for the full evolution operator obtained from the intermediate Hamiltonian partitioning into the right-hand side of (A.27) leads to the expression

$$\begin{aligned} U(t,t') = U_i(t,t') &- \frac{\mathrm{i}}{\hbar}\int_{t'}^{t} U_f(t,\tau_0)V_i(\tau_0)U_i(\tau_0,t')\,\mathrm{d}\tau_0 \\ &- \left(\frac{\mathrm{i}}{\hbar}\right)^2 \int_{t'}^{t}\int_{\tau_0}^{t} U_f(t,\tau_1)V_f(\tau_1)U_m(\tau_1,\tau_0)V_i(\tau_0)U_i(\tau_0,t')\,\mathrm{d}\tau_0\,\mathrm{d}\tau_1 \\ &- \left(\frac{\mathrm{i}}{\hbar}\right)^3 \int_{t'}^{t}\int_{\tau_0}^{t}\int_{\tau_0}^{\tau_1} U_f(t,\tau_2)V_f(\tau_2)U(\tau_2,\tau_1)V_m(\tau_1)U_m(\tau_1,\tau_0) \\ &\qquad \times V_i(\tau_0)U_i(\tau_0,t')\,\mathrm{d}\tau_0\,\mathrm{d}\tau_1\,\mathrm{d}\tau_2 \end{aligned} \tag{A.29}$$

The first two terms in this expression are identical to (A.27), and can be interpreted in the same way. The third term can be interpreted in a similar fashion. At time τ_0 the initial state interacts with the laser and leads to the transition from the initial state governed by $H_i^{(0)}$ to an *intermediate* state governed by $H_m^{(0)}$ through the perturbation V_i in the initial partitioning (A.23). The intermediate state is propagated from τ_0 to τ_1, being governed fully by the intermediate main Hamiltonian $H_m^{(0)}$. Finally, at time τ_1 a transitions from the intermediate state to the *final* state is induced through the perturbation V_f in the final partitioning (A.24), after which the final state evolves freely according to U_f. The full evolution operator can again be approximated by simply leaving out the final term in (A.29), or one could introduce further intermediate Hamiltonian partitions. Finally, it is also possible to take the Dyson series expansion (A.22) of the evolution operator in the intermediate partitioning scheme, and obtain higher order interactions in the intermediate state in which multiple interactions with the perturbation potential V_m are taken into account.

To represent the process of ionization in a strong field, including re-scattering of the photoelectron from the remaining ionic core as an intermediate step, it is necessary to adopt *three* Hamiltonian partitioning schemes. In the initial partitioning scheme the field-free target Hamiltonian H_T is taken as the reference and the laser field V_L as the perturbation. In the intermediate *and* final partitioning schemes the laser-electron Hamiltonian H_L, which corresponds to a single electron in a classical laser field, is taken as the reference, and the field-free *target* Hamiltonian V_T is taken as the perturbation. This partitioning

scheme can be summarized as follows

$$H_i^{(0)} = H_T \qquad V_i = V_L \tag{A.30}$$

$$H_m^{(0)} = H_f^{(0)} = H_L \qquad V_m = V_f = V_T \tag{A.31}$$

Substituting this partitioning scheme into the IMST expression for the full evolution operator (A.29) leads to the following expression

$$\begin{aligned} U(t,t') = U_i(t,t') &- \frac{\mathrm{i}}{\hbar}\int_{t'}^{t} U_L(t,\tau_0)V_L(\tau_0)U_T(\tau_0,t')\,\mathrm{d}\tau_0 \\ &- \left(\frac{\mathrm{i}}{\hbar}\right)^2 \int_{t'}^{t}\int_{\tau_0}^{t} U_L(t,\tau_1)V_T(\tau_1)U_L(\tau_1,\tau_0)V_L(\tau_0)U_T(\tau_0,t')\,\mathrm{d}\tau_0\,\mathrm{d}\tau_1 \\ &- \left(\frac{\mathrm{i}}{\hbar}\right)^3 \int_{t'}^{t}\int_{\tau_0}^{t}\int_{\tau_0}^{\tau_1} U_L(t,\tau_2)V_T(\tau_2)U(\tau_2,\tau_1)V_T(\tau_1)U_L(\tau_1,\tau_0) \\ &\qquad \times V_L(\tau_0)U_T(\tau_0,t')\,\mathrm{d}\tau_0\,\mathrm{d}\tau_1\,\mathrm{d}\tau_2 \end{aligned} \tag{A.32}$$

where U_T, U_L are the evolution operators corresponding to the field-free target, and the laser-electron Hamiltonian H_T and H_L respectively. The first term in this expression is simply the evolution operator of the initial target state and represents the part of the system which is not affected by the laser. The second term in this equation represents the transition at time τ_0 from the initial target state, through an interaction with the laser field perturbation V_L, to a final continuum state governed by the laser-electron Hamiltonian H_L. In the third term, the initial state interacts with the laser at time τ_0, leading to a transition to an *intermediate* continuum state governed by H_L. The intermediate state evolves freely from τ_0 to τ_1, at which time a transition takes place from the intermediate to the *final* continuum state through an interaction with the perturbation V_T, i.e. the parent ion. After this, the final state evolves freely again according to U_L. The final term in (A.32) represents higher order processes in which further interactions with the parent ion are included.

In his treatment of the ionization of an atom by a strong laser field, Keldysh approximates the full propagator by the first two terms in (A.32) [63]. Since the final perturbation term V_T does not appear in the first two terms of the full evolution operator (A.32), Keldysh's final partitioning scheme was implicit in the choice of the final state wavefunctions, i.e. Volkov wavefunctions. This is the so-called Strong Field Approximation (SFA). As it became clear that the Keldysh's SFA was not able to explain High-order Above Threshold Ionization (HATI), and other effects in which re-scattering plays an crucial role, improved versions of the theory, i.e. SFA2, were introduced to effectively include the third term in (A.32) [64, 65]. The MSFT is in fact a SFA2 theory applied to the case of molecules. Higher order versions of the theory which go beyond the SFA2 have also been proposed. For example, it is possible to introduce a fourth partitioning scheme so that in addition to the *perturbative* interaction, treated by the third term in (A.32), a strong interaction, i.e. hard scattering, between the target and the photoelectron can be treated more appropriately [103, 124, 125].

Bibliography

[1] H. Niikura, F. Légaré, R. Hasbani, A.D. Bandrauk, M. Yu Ivanov, D.M. Villeneuve, and P.B. Corkum. Sub-laser-cycle electron pulses for probing molecular dynamics. *Nature*, 417(6892):917–922, 2002.

[2] M. Lein, J.P. Marangos, and P.L. Knight. Electron diffraction in above-threshold ionization of molecules. *Physical Review A*, 66(5):051404, 2002.

[3] M. Spanner, O. Smirnova, P. B. Corkum, and M. Y. Ivanov. Reading diffraction images in strong field ionization of diatomic molecules. *J. Phys. B: At., Mol. Opt. Phys.*, 37:L243–L250, 2004.

[4] M.F. Ciappina, O.A. Fojón, and R.D. Rivarola. Coherent electron emission from simple molecules by impact of energetic charged particles. *Journal of Physics B: Atomic, Molecular and Optical Physics*, 47(4):042001, 2014.

[5] A. H. Zewail. Femtochemistry: atomic-scale dynamics of the chemical bond using ultrafast lasers (Nobel Lecture). *Angew. Chem. Int. Ed.*, 39:2586–2631, 2000.

[6] T. S. Rose, M. J. Rosker, and A. H. Zewail. Femtosecond real-time observation of wave packet oscillations (resonance) in dissociation reactions. *The Journal of Chemical Physics*, 88(10):6672–6673, 1988.

[7] A. H. Zewail. Four-dimensional electron microscopy. *Science*, 328:187–193, 2010.

[8] J. R. Dwyer, C. T. Hebeisen, R. Ernstorfer, M. Harb, V. B.Deyirmenjian, R. E. Jordan, and R. J. Dwayne Miller. Femtosecond electron diffraction: 'making the molecular movie'. *Phil. trans. R. Soc. A*, 364:741–778, 2006.

[9] J.C. Williamson and A.H. Zewail. Structural femtochemistry: Experimental methodology. *Proceedings of the National Academy of Sciences*, 88(11):5021–5025, 1991.

[10] J.C. Williamson, M. Dantus, S.B. Kim, and A.H. Zewail. Ultrafast diffraction and molecular structure. *Chemical physics letters*, 196(6):529–534, 1992.

[11] H. Ihee, V.A. Lobastov, U.M. Gomez, B.M. Goodson, R. Srinivasan, C-Y Ruan, and A.H. Zewail. Direct imaging of transient molecular structures with ultrafast diffraction. *Science*, 291(5503):458–462, 2001.

[12] B. J. Siwick, J. R. Dwyer, R. E. Jordan, and R.J. D. Miller. An atomic-level view of melting using femtosecond electron diffraction. *Science*, 302(5649):1382–1385, 2003.

[13] L. Waldecker, R. Bertoni, R. Ernstorfer, and J. Vorberger. Electron-phonon coupling and energy flow in a simple metal beyond the two-temperature approximation. *Physical Review X*, 6(2):021003, 2016.

[14] R. Neutze, R. Wouts, D. van der Spoel, E. Weckert, and J. Hajdu. Potential for biomolecular imaging with femtosecond x-ray pulses. *Nature*, 406(6797):752–757, 2000.

[15] J. Tenboer, S. Basu, N. Zatsepin, K. Pande, D. Milathianaki, M. Frank, M. Hunter, S. Boutet, G. J. Williams, J. E. Koglin, et al. Time-resolved serial crystallography captures high-resolution intermediates of photoactive yellow protein. *Science*, 346(6214):1242–1246, 2014.

[16] K. Pande, C.D.M. Hutchison, G. Groenhof, A. Aquila, J.S. Robinson, J. Tenboer, S. Basu, S. Boutet, D.P. DePonte, M. Liang, et al. Femtosecond structural dynamics drives the trans/cis isomerization in photoactive yellow protein. *Science*, 352(6286):725–729, 2016.

[17] A. Landers, Th. Weber, I. Ali, A. Cassimi, M. Hattass, O. Jagutzki, A. Nauert, T. Osipov, A. Staudte, M. H. Prior, H. Schmidt-Böcking, C. L. Cocke, and R. Dörner. Photoelectron diffraction mapping: Molecules illuminated from within. *Phys. Rev. Lett.*, 87:013002, 2001.

[18] F. Krasniqi, B. Najjari, L. Struder, D. Rolles, A. Voitkiv, and J. Ullrich. Imaging molecules from within: Ultrafast angström-scale structure determination of molecules via photoelectron holography using free-electron lasers. *Phys. Rev. A*, 81:033411, 2010.

[19] R. Boll, D. Anielski, C. Bostedt, J.D. Bozek, L. Christensen, R. Coffee, S. De, P. Decleva, S.W. Epp, B. Erk, et al. Femtosecond photoelectron diffraction on laser-aligned molecules: Towards time-resolved imaging of molecular structure. *Physical Review A*, 88(6):061402, 2013.

[20] T. van Oudheusden, P. L. E. M. Pasmans, S. B. van der Geer, M. J. de Loos, M. J. van der Wiel, and O. J. Luiten. Electron source concept for single-shot sub-100 fs electron diffraction in the 100 kev range. *J. Appl. Phys. 102, 093501 (2007)*, 102:093501, 2007.

[21] C.S. Fadley. The study of surface structures by photoelectron diffraction and auger electron diffraction. In *Synchrotron Radiation Research*, pages 421–518. Springer, 1992.

[22] J. Küpper, S. Stern, L. Holmegaard, F. Filsinger, A. Rouzeé, A. Rudenko, P. Johnsson, A. V. Martin, M. Adolph, A. Aquila, et al. X-ray diffraction from isolated and strongly aligned gas-phase molecules with a free-electron laser. *Phys. Rev. Lett.*, 112(8):083002, 2014.

[23] P. Reckenthaeler, M. Centurion, W. Fuß, S.A. Trushin, F. Krausz, and E.E. Fill. Time-resolved electron diffraction from selectively aligned molecules. *Phys. Rev. Lett.*, 2009.

[24] C. J. Hensley, J. Yang, and M. Centurion. Imaging of isolated molecules with ultrafast electron pulses. *Phys. Rev. Lett.*, 2012.

[25] L.D. Landau and E.M. Lifshitz. *Classical mechanics*. Pergamon Press, Oxford, 1960.

[26] E. Merzbacher. *Quantum mechanics*. Wiley international editions. J. Wiley, 1970.

[27] J. R. Taylor. *Scattering theory: the quantum theory of nonrelativistic collisions*. Dover Publications, 2006.

[28] C. J. Joachain, N. J. Kylstra, and R. M. Potvliege. *Atoms in intense laser fields*. Cambridge University Press, 2012.

[29] B. H. Bransden and C. J. Joachain. *Physics of atoms and molecules*. Pearson Education India, 2003.

[30] L. D. Landau and E. M. Lifshitz. *Quantum mechanics: non-relativistic theory*, volume 3. Elsevier, 2013.

[31] H.J. Weber and G.B. Arfken. *Essential Mathematical Methods for Physicists, ISE*. Academic Press, 2003.

[32] Milton Abramowitz and Irene A Stegun. *Handbook of mathematical functions: with formulas, graphs, and mathematical tables*. Courier Corporation, 1964.

[33] P. G. Burke. *R-Matrix Theory of Atomic Collisions: Application to Atomic, Molecular and Optical Processes*, volume 61. Springer Science & Business Media, 2011.

[34] K. A. Berrington, W. B. Eissner, and P. H. Norrington. RMATRX1: Belfast atomic R-matrix codes. *Computer Physics Communications*, 92(2):290–420, 1995.

[35] R. R. Lucchese, K. Takatsuka, and V. McKoy. Applications of the schwinger variational principle to electron-molecule collisions and molecular photoionization. *Physics Reports*, 131(3):147–221, 1986.

[36] F. Salvat, A. Jablonski, and C. J. Powell. ELSEPA–Dirac partial-wave calculation of elastic scattering of electrons and positrons by atoms, positive ions and molecules. *Computer physics communications*, 165(2):157–190, 2005.

[37] J. Als-Nielsen and D. McMorrow. *Elements of modern X-ray physics*. John Wiley & Sons, 2011.

[38] P.J. Brown, A.G. Fox, E.N. Maslen, M.A. O'Keefe, and B.T.M. Willis. Intensity of diffracted intensities. In *International Tables for Crystallography Volume C: Mathematical, physical and chemical tables*, pages 554–595. Springer, 2005.

[39] C. Colliex, J. M. Cowley, S. L. Dudarev, M. Fink, J. Gjúnnes, R. Hilderbrandt, A. Howie, D. F. Lynch, L. M. Peng, G. Ren, A. W. Ross, V. H. Smith, J. C. H. Spence, J. W. Steeds, J. Wang, M. J. Whelan, and B. B. Zvyagin. Electron diffraction. In *International Tables for Crystallography Volume C: Mathematical, physical and chemical tables*, pages 259–429. Springer, 2005.

[40] F. W. Byron and C. J. Joachain. Theory of (e,2e) reactions. *Physics reports*, 179(4):211–272, 1989.

[41] Mitio Inokuti. Inelastic collisions of fast charged particles with atoms and molecules—the bethe theory revisited. *Reviews of modern physics*, 43(3):297, 1971.

[42] M. A. Coplan, J. H. Moore, and J. P. Doering. (e,2e) spectroscopy. *Rev. Mod. Phys.*, 66:985, 1994.

[43] B. Podolsky and L. Pauling. The momentum distribution in hydrogen-like atoms. *Physical Review*, 34:109, 1929.

[44] K. Bartschat, I. E. McCarthy, R. P. McEachran, D. H. Madison, Z. Xixiang, and K. Bartschat. *Computational atomic physics: electron and positron collisions with atoms and ions*. Springer, 2013.

[45] I. Hargittai and M. Hargittai, editors. *Stereochemical applications of gas-phase electron diffraction*. VCH, 1988.

[46] H. D. Cohen and U. Fano. Interference in photo-ionization of molecules. *Phys. Rev.*, 150:30–33, 1966.

[47] N. Stolterfoht, B. Sulik, V. Hoffmann, B. Skogvall, J.-Y. Chesnel, J. Rangama, F. Frémont, D. Hennecart, A. Cassimi, X. Husson, et al. Evidence for interference effects in electron emission from H_2 colliding with 60 MeV/u Kr^{34+} ions. *Physical Review Letters*, 87(2):023201, 2001.

[48] N. Stolterfoht, B. Sulik, B. Skogvall, J-Y Chesnel, F. Frémont, D. Hennecart, A. Cassimi, L. Adoui, S. Hossain, and J.A. Tanis. Frequency doubling of interference structures in electron emission interferences from H_2 by 68 MeV/u Kr^{33+} impact. *Physical Review A*, 69(1):012701, 2004.

[49] J.L. Baran, S. Das, F. Járai-Szabó, K. Póra, L. Nagy, and J.A. Tanis. Suppression of primary electron interferences in the ionization of N_2 by 1–5 MeV/u protons. *Physical Review A*, 78(1):012710, 2008.

[50] D.S. Milne-Brownlie, M. Foster, J. Gao, B. Lohmann, and D.H. Madison. Young-type interference in (e,2e) ionization of H_2. *Physical review letters*, 96(23):233201, 2006.

[51] E.M. Staicu Casagrande, A. Naja, F. Mezdari, A. Lahmam-Bennani, P. Bolognesi, B. Joulakian, O. Chuluunbaatar, O. Al-Hagan, Don H. Madison, D.V. Fursa, et al. (e,2e) ionization of helium and the hydrogen molecule: signature of two-centre interference effects. *Journal of Physics B: Atomic, Molecular and Optical Physics*, 41(2):025204, 2008.

[52] L.R. Hargreaves, C. Colyer, M.A. Stevenson, B. Lohmann, O. Al-Hagan, D.H. Madison, and C.G. Ning. (e,2e) study of two-center interference effects in the ionization of N_2. *Physical Review A*, 80(6):062704, 2009.

[53] J.A. Tanis, J-Y Chesnel, B. Sulik, B. Skogvall, P. Sobocinski, A. Cassimi, J-P Grandin, L. Adoui, D. Hennecart, and N. Stolterfoht. Angular and high-frequency analysis of electron interference structures in ∼60 MeV/u Kr^{34+}+H_2 collisions. *Physical Review A*, 74(2):022707, 2006.

[54] H. Agueny, A. Makhoute, A. Dubois, and J.P. Hansen. Coherent electron emission beyond young-type interference from diatomic molecules. *Physical Review A*, 93(1):012713, 2016.

[55] B. Joulakian, J. Hanssen, R. Rivarola, and A. Motassim. Dissociative ionization of H_2^+ by fast-electron impact: Use of a two-center continuum wave function. *Phys. Rev. A*, 1996.

[56] P. Weck, O. A. Fojón, J. Hanssen, B. Joulakian, and R. D. Rivarola. Two-effective center approximation for the single ionization of molecular hydrogen by fast electron impact. *Physical Review A*, 63(4):042709, 2001.

[57] C. R. Stia, A. Fojon, P. F. Weck, J. Hanssen, B. Joulakian, and R. D. Rivarola. Molecular three-continuum approximation for ionization of H_2 by electron impact. *Phys. Rev. A*, 2002.

[58] C. R. Stia, O. A. Fojón, P. F. Weck, J. Hanssen, and R. D. Rivarola. Interference effects in single ionization of molecular hydrogen by electron impact. *J. Phys. B: At., Mol. Opt. Phys.*, 36:L257 – L264, 2003.

[59] M. Brauner, J.S. Briggs, and H. Klar. Triply-differential cross sections for ionisation of hydrogen atoms by electrons and positrons. *Journal of Physics B: Atomic, Molecular and Optical Physics*, 22(14):2265, 1989.

[60] T. Zuo, A. D. Bandrauk, and P. B. Corkum. Laser-induced electron diffraction: a new tool for probing ultrafast molecular dynamics. *Chem. Phys. Lett.*, 259:313–320, 1996.

[61] P. B. Corkum. Plasma perspective on strong-field multiphoton ionization. *Phys. Rev. Lett.*, 71(13), 1993.

[62] Z. Chen, A. Le, T. Morishita, and C.D. Lin. Quantitative rescattering theory for laser-induced high-energy plateau photoelectron spectra. *Phys. Rev. A*, 79:033409, 2009.

[63] L. V. Keldysh. Ionization in the field of a strong electromagnetic wave. *Sov. Phys. JETP*, 20(5):1307–1314, 1965.

[64] W. Becker, A. Lohr, and M. Kleber. Effects of rescattering on above-threshold ionization. *Journal of Physics B: Atomic, Molecular and Optical Physics*, 27(14):L325, 1994.

[65] M. Lewenstein, K. C. Kulander, K. J. Schafer, and P. H. Bucksbaum. Rings in above-threshold ionization: A quasiclassical analysis. *Physical Review A*, 51(2):1495, 1995.

[66] A. Becker and F. H.M. Faisal. Intense-field many-body s-matrix theory. *Journal of Physics B: Atomic, Molecular and Optical Physics*, 38(3):R1, 2005.

[67] M. Ivanov. Ionization in strong low-frequency fields. In T. Schultz and M. Vrakking, editors, *Attosecond and XUV physics: ultrafast dynamics and spectroscopy*, chapter 6, pages 177 – 200. Wiley Online Library, 2014.

[68] M. Meckel, D. Comtois, D. Zeidler, A. Staudte, D. Pavičić, H.C. Bandulet, H. Pépin, J.C. Kieffer, R. Dörner, D.M. Villeneuve, and P. B. Corkum. Laser-induced electron tunneling and diffraction. *Science*, 320(5882):1478–1482, 2008.

[69] C. I. Blaga, J. Xu, A. D. DiChiara, E. Sistrunk, K. Zhang, P. Agostini, T. A. Miller, L. F. DiMauro, and C. D. Lin. Imaging ultrafast molecular dynamics with laser-induced electron diffraction. *Nature*, 483:194–197, 2012.

[70] M.V. Ammosov, N.B. Delone, V.P. Krainov, et al. Tunnel ionization of complex atoms and of atomic ions in an alternating electromagnetic field. *Sov. Phys. JETP*, 64(6):1191–1194, 1986.

[71] I. Martin and G. Simons. New procedure for generating valence and rydberg orbitals. ii. atomic photoionization cross sections. *The Journal of Chemical Physics*, 62(12):4799–4803, 1975.

[72] X. M. Tong, Z. X. Zhao, and C. D. Lin. Theory of molecular tunneling ionization. *Physical Review A*, 66(3):033402, 2002.

[73] T. K. Kjeldsen and L. B. Madsen. Strong-field ionization of n2: length and velocity gauge strong-field approximation and tunnelling theory. *Journal of Physics B: Atomic, Molecular and Optical Physics*, 37(10):2033, 2004.

[74] P. Agostini and L.F. DiMauro. Atoms in high intensity mid-infrared pulses. *Contemporary Physics*, 49(3):179–197, 2008.

[75] H. Cho, M.Y. Song, J.S. Yoon, M. Hoshino, and H. Tanaka. Elastic electron scattering from CF_3H and CF_3I. *Journal of Physics B: Atomic, Molecular and Optical Physics*, 43(13):135205, 2010.

[76] J. Xu, Z. Chen, A.-T. Le, and C.D. Lin. Self-imaging of molecules from diffraction spectra by laser-induced rescattering electrons. *Physical Review A*, 82(3):033403, 2010.

[77] M. Okunishi, H. Niikura, R. R. Lucchese, T. Morishita, and K. Ueda. Extracting electron-ion differential scattering cross sections for partially aligned molecules by laser-induced rescattering photoelectron spectroscopy. *Physical review letters*, 106(6):063001, 2011.

[78] J. Xu, C. I. Blaga, K. Zhang, Y. H. Lai, C.D. Lin, T. A. Miller, P. Agostini, and L. F. DiMauro. Diffraction using laser-driven broadband electron wave packets. *Nature communications*, 5, 2014.

[79] M. Pullen, B. Wolter, A.-T. Le, M. Baudisch, M. Hemmer, A. Senftleben, C.D. Schröter, J. Ullrich, R. Moshammer, C.D. Lin, et al. Imaging an aligned polyatomic molecule with laser-induced electron diffraction. *Nature Communications*, 6, 2015.

[80] Y. Ito, C. Wang, A. Le, M. Okunishi, D. Ding, C.D. Lin, and K. Ueda. Extracting conformational structure information of benzene molecules via laser-induced electron diffraction. *Structural Dynamics*, 3(3):034303, 2016.

[81] C. Yu, H. Wei, X. Wang, A.-T. Le, R. Lu, and C.D. Lin. Reconstruction of two-dimensional molecular structure with laser-induced electron diffraction from laser-aligned polyatomic molecules. *Scientific reports*, 5, 2015.

[82] T. Seideman. Rotational excitation and molecular alignment in intense laser fields. *J. Chem. Phys.*, 103(18):7887–7896, 1995.

[83] H. Stapelfeldt and T. Seideman. Aligning molecules with strong laser pulses. *Reviews of Modern Physics*, 75(2):543, 2003.

[84] S. K. Lee, Y. F. Lin, L. Yan, and W. Li. Laser-induced low energy electron diffraction in aligned molecules. *The Journal of Physical Chemistry A*, 116(8):1950–1955, 2012.

[85] J. Ullrich, R. Moshammer, A. Dorn, R. Dörner, L. Schmidt, and H. Schmidt-Böcking. Recoil-ion and electron momentum spectroscopy: reaction-microscopes. *Reports on Progress in Physics*, 66(9):1463, 2003.

[86] A. T. J. B. Eppink and D. H. Parker. Velocity map imaging of ions and electrons using electrostatic lenses: Application in photoelectron and photofragment ion imaging of molecular oxygen. *Rev. Sci. Instrum.*, 68(9):3477–3484, 1997.

[87] U. De Giovannini, D. Varsano, M. A. L. Marques, H. Appel, E. K. U. Gross, and A. Rubio. Ab initio angle-and energy-resolved photoelectron spectroscopy with time-dependent density-functional theory. *Physical Review A*, 85(6):062515, 2012.

[88] D. B. Milošević. Strong-field approximation for ionization of a diatomic molecule by a strong laser field. *Physical Review A*, 74(6):063404, 2006.

[89] M. Busuladžić, A. Gazibegović-Busuladžić, D. B. Milošević, and W. Becker. Strong-field approximation for ionization of a diatomic molecule by a strong laser field. ii. the role of electron rescattering off the molecular centers. *Physical Review A*, 78(3):033412, 2008.

[90] E. Hasović and D.B. Milošević. Strong-field approximation for above-threshold ionization of polyatomic molecules. *Physical Review A*, 86(4):043429, 2012.

[91] E. Hasović and D.B. Milošević. Strong-field approximation for above-threshold ionization of polyatomic molecules. II the role of electron rescattering off the molecular centers. *Physical Review A*, 89(5):053401, 2014.

[92] T. Seideman. Revival structure of aligned rotational wave packets. *Phys. Rev. Lett.*, 83(24):4971, 1999.

[93] M. Wollenhaupt, M. Krug, J. Köhler, T. Bayer, C. Sarpe-Tudoran, and T. Baumert. Three-dimensional tomographic reconstruction of ultrashort free electron wave packets. *Applied Physics B*, 95(4):647–651, 2009.

[94] C. Smeenk, L. Arissian, A. Staudte, D.M. Villeneuve, and P.B. Corkum. Momentum space tomographic imaging of photoelectrons. *Journal of Physics B: Atomic, Molecular and Optical Physics*, 42(18):185402, 2009.

[95] V. Dribinski, A. Ossadtchi, V. A. Mandelshtam, and H. Reisler. Reconstruction of abel-transformable images: The gaussian basis-set expansion abel transform method. *Review of Scientific Instruments*, 73(7):2634–2642, 2002.

[96] M. D. Morse. Supersonic beam sources. In F.B. Dunning and Randall G. Hulet, editors, *Atomic, Molecular, and Optical Physics: Atoms and Molecules*, volume 29, Part B of *Experimental Methods in the Physical Sciences*, pages 21 – 47. Academic Press, 1996.

[97] U. Even, J. Jortner, D. Noy, N. Lavie, and C. Cossart-Magos. Cooling of large molecules below 1 k and he clusters formation. *The Journal of Chemical Physics*, 112(18):8068–8071, 2000.

[98] Y. Huismans, A. Rouzée, A. Gijsbertsen, J. H. Jungmann, A. S. Smolkowska, P. S. W. M. Logman, F. Lépine, C. Cauchy, S. Zamith, T. Marchenko, J. M. Bakker, G. Berden, B. Redlich, A. F. G. van der Meer, H. G. Muller, W. Vermin, K. J. Schafer, M. Spanner, M. Yu. Ivanov, O. Smirnova, D. Bauer, S. V. Popruzhenko, and M. J. J. Vrakking. Time-resolved holography with photoelectrons. *Science*, 331:61–64, 2011.

[99] B. Friedrich and D. Herschbach. Alignment and trapping of molecules in intense laser fields. *Phys. Rev. Lett.*, 74(23):4623, 1995.

[100] O. Smirnova, M. Spanner, and M. Ivanov. Coulomb and polarization effects in sub-cycle dynamics of strong-field ionization. *Journal of Physics B: Atomic, Molecular and Optical Physics*, 39(13):S307, 2006.

[101] A. E. S. Green, D. L. Sellin, and A. S. Zachor. Analytic independent-particle model for atoms. *Physical Review*, 184(1):1, 1969.

[102] A. Čerkić and D. B. Milošević. Plateau structures in potential scattering in a strong laser field. *Physical Review A*, 70(5):053402, 2004.

[103] A. Čerkić, E. Hasović, D.B. Milošević, and W. Becker. High-order above-threshold ionization beyond the first-order born approximation. *Physical Review A*, 79(3):033413, 2009.

[104] N. M. Kroll and K. M. Watson. Charged-particle scattering in the presence of a strong electromagnetic wave. *Physical Review A*, 8(2):804, 1973.

[105] L. Tao and A. Scrinzi. Photo-electron momentum spectra from minimal volumes: the time-dependent surface flux method. *New Journal of Physics*, 14(1):013021, 2012.

[106] R. de L. Kronig. Zur theorie der feinstruktur in den röntgenabsorptionsspektren. iii. *Zeitschrift für Physik A Hadrons and Nuclei*, 75(7):468–475, 1932.

[107] J. J. Rehr and R. C. Albers. Theoretical approaches to X-ray absorption fine structure. *Reviews of modern physics*, 72(3):621, 2000.

[108] S. Hossain, A.L. Landers, N. Stolterfoht, and J.A. Tanis. Interference phenomena associated with electron-emission from H_2 by (1–5)-MeV H^+ impact. *Physical Review A*, 72(1):010701, 2005.

[109] S. Chatterjee, D. Misra, A. H. Kelkar, L. C. Tribedi, C. R. Stia, O. A. Fojón, and R. D. Rivarola. Young-type interference effect on angular distribution of secondary electrons emitted from H_2 in collisions with fast electrons. *Phys. Rev. A*, 78:052701, 2008.

[110] S. Nandi, A.N. Agnihotri, C.A. Tachino, R.D. Rivarola, F. Martín, and L.C. Tribedi. Investigation of the interference effect in the case of low energy electron emission from O_2 in collisions with fast bare C-ions. *Journal of Physics B: Atomic, Molecular and Optical Physics*, 45(21):215207, 2012.

[111] D. H. Madison and O. Al-Hagan. The distorted-wave born approach for calculating electron-impact ionization of molecules. *Journal of Atomic, Molecular, and Optical Physics*, 2010, 2010.

[112] T. Van Oudheusden, P.L.E.M. Pasmans, S.B. Van Der Geer, M.J. De Loos, M.J. Van Der Wiel, and O.J. Luiten. Compression of subrelativistic space-charge-dominated electron bunches for single-shot femtosecond electron diffraction. *Physical review letters*, 105(26):264801, 2010.

[113] T. van Oudheusden. *Electron source for sub-relativistic single-shot femtosecond diffraction*. PhD thesis, Eindhoven University of Technology, 2010.

[114] Pulsar Physics. http://www.pulsar.nl/.

[115] S.B. van der Geer and M.J. de Loos. GPT simulations for ultrafast velocity map imaging. Internal Report, September 2011.

[116] M. Gao, H. Jean-Ruel, R.R. Cooney, J. Stampe, M. de Jong, M. Harb, G. Sciaini, G. Moriena, and R.J. D. Miller. Full characterization of rf compressed femtosecond electron pulses using ponderomotive scattering. *Optics express*, 20(11):12048–12058, 2012.

[117] A. Gliserin, A. Apolonski, F. Krausz, and P. Baum. Compression of single-electron pulses with a microwave cavity. *New Journal of Physics*, 14(7):073055, 2012.

[118] W. Lotz. An empirical formula for the electron-impact ionization cross-section. *Zeitschrift für Physik*, 206(2):205–211, 1967.

[119] W. Lotz. Electron-impact ionization cross-sections and ionization rate coefficients for atoms and ions from hydrogen to calcium. *Zeitschrift für Physik*, 216(3):241–247, 1968.

[120] W. Lotz. Electron binding energies in free atoms. *JOSA*, 60(2):206–210, 1970.

[121] S. Chatterjee, A.N. Agnihotri, C.R. Stia, O.A. Fojón, R.D. Rivarola, and L.C. Tribedi. Bethe binary-encounter peaks in the double-differential cross sections for high-energy electron-impact ionization of h 2 and he. *Physical Review A*, 82(5):052709, 2010.

[122] M.J. Brothers and R.A. Bonham. Approximate first born descriptions of high-energy asymmetric (e,2e) cross sections for helium. *Journal of Physics B: Atomic and Molecular Physics*, 17(20):4235, 1984.

[123] G. Laurent, P.D. Fainstein, M.E. Galassi, R.D. Rivarola, L. Adoui, and A. Cassimi. Orientation and interference effects in single ionization of H_2 by fast ions. *Journal of Physics B: Atomic, Molecular and Optical Physics*, 35(22):L495, 2002.

[124] L. Torlina and O. Smirnova. Time-dependent analytical R-matrix approach for strong-field dynamics. I. one-electron systems. *Physical Review A*, 86(4):043408, 2012.

[125] L. Torlina, M. Ivanov, Z. B. Walters, and O. Smirnova. Time-dependent analytical R-matrix approach for strong-field dynamics. II. many-electron systems. *Physical Review A*, 86(4):043409, 2012.

Acknowledgements

I am indebted to many people for their help and encouragement, which were vital for the successful completion of this work. First of all I would like to thank my supervisor, Marc Vrakking, for giving me the wonderful opportunity to pursue my doctorate at the Max Born Institute in Berlin, and for spending his very limited time with me, offering his guidance and helpful insights. Furthermore, I would like to thank Arnaud Rouzeé, who was my day-to-day supervisor, for all his hard work in the lab, helping me with the experiments and teaching me how to work with the VMI.

I would also like to thank all the PhD students who worked together with me in the lab and assisted in obtaining the experimental data shown in this thesis: Axel Hundertmark, Jean-Gabriel Brisset, Felix Braußе and Sebastian Raabe. Also, thanks to Bernd Schütte for being a good listener and a supportive colleague with whom I have shared the lab during the long days of measurement.

Special thanks go to Thomas Schultz, Oleg Kornilov, Claus-Peter Schulz, Jochen Mikosch, Misha Ivanov, Wilhelm Becker, Serguei Patchkovskii and Olga Smirnova, with whom I have discussed and expanded my limited knowledge of the theory and philosophy of physics, ranging from strong-field theory to spectroscopy, and beyond.

I would like to also acknowledge the funding under European Community 7^{th} Framework Programme, under contract ITN-2008-238362 (ATTOFEL), that I received in the first years of my PhD studies and that was initiated and supervised by Marc Vrakking. I would like to thank all the other fellows of the ATTOFEL network, especially Filippo, Christoph and Piotr, for co-organizing a wonderful Winterschool event in Bormio, Italy, where we came together with very experienced and inspirational people to discuss the exciting and difficult choice of future and career building.

Furthermore, I would like to thank Jom Luiten, Peter Baum and Dejan Milosević for the hospitality they have shown by receiving me at their groups and the expertise and insight they have shared to help me in building and understanding my experiments.

During my time at the Max Born Institute I have gotten to know an befriend many of the other PhD students. Christian Neidel, Christian Schröter, Jesse Klei and Lukas Medisauskas, thank you for all the work, and non-work, related discussions and support you have shown me over the years we spent together.

Though my family was in the rather far-away Rotterdam during my time spent on the PhD studies, it was their loving support and hard work that helped me and enabled me to get this far. Mama, Tata, Tarik, Hana, thank you. Also, a special thanks to my newly added family member and mother-in-law Arilee for travelling to Berlin and staying with us for several months to help us during

the time that I was writing this thesis. Farah, thank you for being so incredibly supportive and enabling me to actually accomplish all of this. You always believed in me, and hearing you say so always restored some peace of mind during the hardest times. Besides being there for me unconditionally, you also gave me a beautiful daughter, Emina, that is a continuous source of wonder and happiness.

Selbstständigkeitserklärung gemäss der Promotionsordnung

Sämtliche verwendeten Hilfsmittel, Hilfen und Quellen sind an der entsprechenden Stelle angegeben. Ich versichere, dass ich auf dieser Grundlage diese Arbeit selbstständig verfasst habe. Diese Arbeit wurde bisher weder in gleicher noch ähnlicher Form einer anderen Prüfungskomission vorgelegt oder veröffentlicht.

Berlin, den 9. September 2016

Faruk Krečinić